

Comparison of Conventional and Super-Glassy Polymers– Molecular Mobility, Gas Transport and Influence of Nanofiller

vorgelegt von

Dipl. – Chem.

Nora Magdalena Konnertz

geboren in Viersen

von der Fakultät II– Mathematik und Naturwissenschaften

der Technischen Universität Berlin

zur Erlangung des akademischen Grades

Doktor der Naturwissenschaften

(Dr. rer. nat.)

genehmigte Dissertation

Promotionsausschuss:

Vorsitzender:

Prof. Dr. Reinhard Schomäcker

1. Gutachterin:

Prof. Dr. Regine von Klitzing

2. Gutachter:

Prof. Dr. Andreas Schönhals

3. Gutachter:

Prof. Dr. Klaus Rätzke

Tag der wissenschaftlichen Aussprache: 16. Februar 2017

Berlin 2017

Acknowledgements

I would like to express my gratitude to all who helped me complete my dissertation with their professional and especially personal support.

My sincere thanks goes out to Prof. Dr. Andreas Schönhals and Dr. Martin Böhning for giving me the opportunity to work at their laboratories at BAM Federal Institute for Materials Research and Testing Berlin. Thank you for your helpful advices, interesting discussions and the trust in me.

I have furthermore to thank Prof. Dr. Regine von Klitzing for undertaking the first correction.

Additionally, I would like to thank my colleagues from BAM for their personal and scientific support. I am deeply indebted to Thomas Ryback for supporting me significantly in technical and scientific questions.

I warmly thank my students Yi Ding, Laura Geoffroy and Vinicius Viana de Souza Duarte. Especially, Yi Ding made significant contributions to my work.

In addition, I would like to thank Dr. Stefan Wellert (TU Berlin) for the WAXS measurements, Dr. Wayne Harrison for the PIM-1 synthesis, Petra Fengler for dynamic mechanical analysis, Michael Morys for the SEM images and Patrick Klack as well as Dietmar Neubert for FTIR and TGA measurements. Furthermore, I express my gratitude to the BAM mechanics for realizing all technical wishes.

For the financial support I gratefully thank the BAM PhD program.

A special thank goes to my family and good friends for their support, patience and love.

Abstract

In the field of gas separation, polymeric membranes are favorable materials. Polymers are inexpensive compared to ceramics and metals, offer a good processability, and possess the ability to operate at large scale. The most important fact about polymeric membranes is their good selectivity. Nevertheless, most of the polymeric membranes show a strong tendency to physical aging and plasticization, which lead to changes in their performance with time. Up to know, it is not fully understood how these drawbacks are connected to the internal molecular mobility. In this study, a commonly used non-porous polyimide for gas separation applications, Matrimid, was compared to a microporous, high performance polymer, PIM-1. PIMs are Polymers with Intrinsic Microporosity and were firstly introduced by Budd and McKeown in the early 2000s. PIM-1 was the first synthesized PIM and, even if many more PIMs followed, PIM-1 shows the most promising gas transport properties. The molecular mobility of the solution casted Matrimid and PIM-1 was investigated by Broadband Dielectric Spectroscopy (BDS). For both polymers, one relaxation process, denoted as β^* , and a conductivity contribution were found. Due to a very high activation energy for this β^* -relaxation (86 kJ/mol for PIM-1 and 99 kJ/mol for Matrimid) and the high temperature range where the peak appeared, it was concluded that the β^* -relaxation has to be of cooperative nature. A sandwich like structure, formed by $\pi - \pi$ -stacking, was assumed. The conductivity, observed for both polymers quite well below their glass transition temperatures, was attributed to the $\pi - \pi$ -stacked structure as well. One approach to reduce and/or overcome plasticization and physical aging is the incorporation of nanofiller. In this study, PhenethylPOSS was embedded in PIM-1 and Matrimid due to an expected interaction of the phenyl substituents of POSS with the π -systems of the polymers and thus probably stabilizing the polymer matrix. Therefore, concentrations of 0 to 20 wt% (0 to 40 wt%) were mixed in Matrimid (PIM-1). A miscibility on a molecular level was observed up to 4 wt% for Matrimid, whereas up to 10 wt% for PIM-1. For higher POSS contents, a phase separation was found, while the size and distribution within the polymers strongly differed from one another.

Enhanced permeability for PIM-1 and Matrimid was achieved with embedding 1 wt% of POSS. Furthermore, the phase separated Matrimid composites yielded a reduced plasticization effect for CO₂.

Zusammenfassung

Auf dem Gebiet der Gastrennung sind polymere Membranen favorisierte Materialien, da sie im Vergleich zu Keramiken und Metallen preiswert sind, eine gute Verarbeitbarkeit bieten und eine hohe Selektivität aufweisen. Allerdings zeigt ein Großteil der Polymermembranen eine starke Tendenz zur physikalischen Alterung und/oder Weichmachung, die im Laufe der Zeit zur Änderungen ihrer Permeabilität und/oder Selektivität führen kann. Inwiefern die molekulare Beweglichkeit mit der physikalischen Alterung und der Weichmachung zusammenhängt, ist bis jetzt allerdings noch nicht vollständig verstanden. Diesen Punkt greift diese Arbeit auf, indem ein kommerziell gebräuchliches, nicht-poröses Polyimid für die Gastrennung, Matrimid, mit einem mikroporösen Hochleistungspolymer, PIM-1, verglichen wird. PIMs sind Polymere mit intrinsischer Mikroporosität und wurden erstmals von Budd und McKoewn in den frühen 2000er Jahren vorgestellt. PIM-1 ist das erste synthetisierte PIM und bringt vielversprechende Gastransporteigenschaften mit. Die molekulare Beweglichkeit der gegossenen Matrimid- und PIM-1-Filme wurde mittels Dielektrischer Relaxationsspektroskopie (BDS) untersucht. Für beide Polymere wurde ein Relaxationsprozess, bezeichnet als β^* , und Leitfähigkeit unterhalb der Glasübergangstemperatur gefunden. Die Aktivierungsenergie für diesen β^* -Relaxationsprozess (86 kJ/mol für PIM-1 und 99 kJ/mol für Matrimid) und der Temperaturbereich, in dem der Peak auftrat, waren sehr hoch. Aus diesen Gründen wurde für die β^* -Relaxation von einem kooperativen Prozess ausgegangen. Es wurde eine "sandwichartige" Struktur angenommen, die sich durch $\pi - \pi$ -Stacking der Polymerketten und/oder -segmenten bildet. Des Weiteren wurde für beide Polymere unterhalb ihrer Glasübergangstemperaturen eine Leitfähigkeit beobachtet, die ebenfalls durch die besondere $\pi - \pi$ Wechselwirkungen erklärt wurde. Ein Ansatz zur Reduktion und/oder Überwindung von Weichmachung und physikalischer Alterung ist der Einsatz von Nanofüllern eingebettet in der Polymermatrix. In dieser Arbeit wurde PhenethylPOSS in PIM-1 und Matrimid gemischt, weil eine Wechselwirkung der Phenylsubstituenten von POSS mit den π -Systemen der Polymere angenommen

wurde und somit die Polymermatrix gegebenenfalls stabilisiert werden kann. Die Konzentrationen wurden von 0 bis 20 Gew.-% für Matrimid (0 bis 40 Gew.-% für PIM-1) variiert. Für Matrimid wurde eine molekulare Mischbarkeit bis zu 4 Gew.-% beobachtet, während bis zu 10 Gew.-% für PIM-1. Bei höheren POSS Konzentrationen kam es zu einer Phasentrennung, während sich die Größe und Verteilung der POSS Agglomerate innerhalb der Polymere stark voneinander unterschieden. Durch Einbringen von 1 Gew.-% POSS in Matrimid und PIM-1 Matrix wurde die Permeabilität deutlich erhöht. Des Weiteren wurde die CO₂ Weichmachung in den Matrimid Kompositen reduziert.

Contents

1	Motivation	1
2	Introduction	5
2.1	Glass Transition Phenomena	5
2.1.1	Thermal Glass Transition	5
2.1.2	Dynamic Glass Transition	9
2.2	Glassy Dynamics	11
2.2.1	Models for the Glass Transition	11
2.3	Gas Separation Membranes	14
2.3.1	Diffusion Mechanism of Gases in Porous and Non-Porous Membranes	14
2.3.2	Gas Separation in Non-Porous Polymers	15
2.3.3	Sorption in Glassy Polymers: Dual Mode Behavior	21
2.3.4	Effects of Permeant	22
2.3.5	Effects of Temperature	23
2.3.6	Challenges and Limits of Technology	24
3	Methods	27
3.1	Broadband Dielectric Spectroscopy (BDS)	27
3.1.1	Theoretical Background	27
3.1.2	Dielectric Response	28
3.1.3	Analysis of Dielectric Spectra	31
3.1.4	Dielectric Measurements	34
3.2	Permeation: Time-Lag Method	36
3.3	Density	38
3.4	Differential Scanning Calorimetry	38
3.5	Dynamic Mechanical Analysis	38
3.6	FTIR Spectroscopy	39

3.7	Scanning Electron Microscopy	39
3.8	Thermogravimetric Analysis	40
4	Materials and Sample Preparation	41
4.1	Materials	41
4.2	Sample Preparation	43
5	Matrimid and Matrimid/POSS Nanocomposites	45
5.1	Introduction	46
5.2	Relaxation Behavior	46
5.2.1	Characterization	47
5.2.2	Relaxation Behavior of Pure Matrimid	50
5.2.3	Properties of Matrimid/POSS Nanocomposites	59
5.2.4	Conclusions	70
5.3	Gas Transport Properties	71
5.3.1	Gas Permeability	71
5.3.2	Conclusions	78
6	PIM-1 and PIM-1/POSS Nanocomposites	79
6.1	Introduction	79
6.2	PIM-1	80
6.2.1	Conclusions	86
6.3	PIM-1/POSS Nanocomposites	87
6.3.1	Characterization	87
6.3.2	Relaxation Behavior	89
6.3.3	Gas Transport Properties	99
6.3.4	Conclusions	105
7	Conclusions and Outlook	107
7.1	Conclusions	107
7.2	Outlook	113
A	Further Experimental Details	I
A.1	Materials and Sample Preparation	I
A.2	Dielectric Investigations: PIM-1 and Matrimid	V
B	Abbreviations	VII

C	Publications	XI
C.1	Paper	XI
C.2	Contributions to Conferences	XII
C.2.1	Oral Presentations	XII
C.2.2	Poster Presentations	XII
D	Bibliography	XIII

1 Motivation

Membrane technology is one of the key technologies to reduce the energy consumption of chemical separation processes and of renewable energy fields because a phase change is not required.

Industrial gas separation membranes are mainly used for hydrogen recovery, air separation and natural gas purifications. Hydrogen recovery is important for ammonia purge gas recovery, oxo-chemical synthesis and refinery gas purification.¹⁻⁴ In the field of air separation, nitrogen enrichment applications have the largest market.^{1,2,5} It is essential to remove carbon dioxide and acidic gases from natural gas to avoid pipeline corrosion, during natural gas transport.⁶

In the last decades, polymer membranes were successfully used in industrial gas separations.⁶ This is due to the fact that they are inexpensive compared to metal or ceramic materials, they show good processability and their ability to operate at large scale.⁷ Besides polysulfones, polycarbonates and aramides, polyimides are now commonly used as gas separation membranes.⁶

In general, the separation properties of a polymer are essential for the performance of a polymeric membrane. Several studies concentrating on structure/property relationships regarding their membrane performances were conducted⁸⁻¹² and have identified structural features, offering desirable gas separation properties.^{11,12} Mostly, glassy polymers with rigid polymer backbones provided the best combination of good separation properties (selectivity) and high performance (permeability), because the frozen-in structure of dense polymers below their glass transition temperature (T_g) offers additional free volume, which is essential for the gas transport through polymers.¹²

Nevertheless, some challenges in membrane science and limitations of membrane technology still remain. Several studies have shown that there is a trade-off relation between permeability and selectivity, which complicates the development of new

materials with high performance and good separation properties. Furthermore, due to the glassy state, polymeric membranes are in a non-equilibrium state, which leads to a continuous change of their internal structure, trying to reach equilibrium. This results in loss of the good performance of glassy polymers with time. This effect is called physical aging.

Another challenge to improve and/or overcome is plasticization. Increasing the concentration of gas within a polymer can lead to a swelling of the polymeric structure. This would lead to increased free volume as well as increased molecular mobility, thus enhancing diffusivity but strongly reducing selectivity.

Up to now, it is not fully understood how the challenging phenomenons of plasticization and physical aging are related to the internal structure of the polymers and thus, hindering large scale applications of various promising polymers. This study is performed to gain a more detailed comprehension on how molecular mobility and gas transport properties are related to the internal structure of a polymer respectively of a polymer nanocomposite. Therefore, the commonly used, non-porous polyimide Matrimid is compared to a high performance polymer, a polymer of intrinsic microporosity (PIM, here PIM-1). Whereas, the used commercially available Matrimid is frequently used for gas separation applications,^{13–15} PIMs were firstly introduced by Budd and McKeown in 2004.^{16,17} The first synthesized PIM, PIM-1, is still of huge interest because it offers extraordinary gas transport properties.

In contrast to other polymers with very high fractional free volume and extremely high gas permeabilities like polyacetylenes (e.g. PTMSP), PIMs offer high permeabilities and high selectivities representing the current state-of-the-art in air separation and hydrogen recovery.^{18,19} Due to the rigid polymer backbone PIMs provide a high additional free volume, which is essential for their high performance. A major drawback for practical membrane applications of PIMs is their tendency to physical aging.^{20,21}

One approach to reduce or even overcome the phenomenon of physical aging and of plasticization as well as improving gas transport properties, is to introduce fillers to the polymer matrix. These composites are often called "mixed matrix membranes" The filler can either be large, small or even nano sized and porous or non-porous. Due to their high surface to volume ratio, nanofiller are especially suited to influence the interface between the matrix and filler. This can either lead to an increase of the free volume, indicating an increase in molecular mobility and sorption abilities or, if the

interaction between filler and matrix is good, to a stabilization of the polymer matrix. Eventually, filler addition to the polymer matrix enhances performance through improving permeability and/or selectivity, as well as reducing or suppressing aging effects and plasticization.^{20,22–24} So this approach can address both important issues of glassy membrane polymers.

Current research for mixed matrix membranes have used e.g. metal-organic frameworks (MOFs),^{25,26} zeolites^{27–29} or silica^{30,31} as nanofiller. In the case of silica nanofillers Polyhedral Oligomeric Silsesquioxanes (POSS) are of huge interest in the field of gas separation.^{32–37} POSS composites, as potential materials for gas separation, were investigated by Rahman et al.^{38,39} POSS may be regarded as the smallest possible silica particle and is composed of a silica cage with organic substituents (R) at the edges ($R_n(SiO_{1.5})_n$ ($n \geq 6$), n is the number of silica atoms). Octa-silsequioxanes are the major product of a typical synthesis route and are mostly investigated. The main advantage of using POSS as filler is that their solubility,⁴⁰ miscibility, thermal stability and mechanical properties are easily influenced by chemical variation of the substituents.^{32,41–43} Besides its good solubility in many solvents, PhenethylPOSS (PhE-POSS) is miscible with different polymers. In this study, PhE-POSS was used as nanofiller for Matrimid and PIM-1 because it is expected that the phenyl-substituent of POSS interacts with the π -system of the polymer, respectively and thus, stabilize the polymer matrix to probably reduce plasticization, aging and improve the gas transport properties.

A correlation between molecular motions of the polymer matrix and the diffusion of gas molecules through the matrix can be observed for conventional glassy polymers. This correlation is in agreement with fundamental transport models^{44,45} as well as simulations of molecular dynamics,^{46,47} which was further discussed for experimental data on ref.^{48,49} The solubility of a gas in a polymer depends on its condensability, the free volume distribution and on the molecular interactions within the polymer matrix.⁵⁰ Furthermore, the already mentioned challenges left in membrane science and limitation of technology permeability/selectivity trade-off, physical aging and plasticization strongly depends on the molecular mobility of the polymer. Additionally, the film formation during casting, i.e. the solidification of the polymer by solvent evaporation, is predominantly governed by the molecular mobility of the polymer matrix. Thus, investigations addressing molecular mobility combined with gas transport experiments are realized in this study for Matrimid as well as PIM-1 and the composites with PhE-POSS as nanofiller, respectively.

2 Introduction

At high temperatures amorphous polymers are in a rubbery, liquid like state. With decreasing temperature they undergo a glass-rubber transition and the polymer becomes glassy. From the temperature range at which the amorphous polymer changes from the highly viscous, rubbery to the glassy, brittle state the glass transition temperature T_g can be estimated. In the following section this phenomenon is discussed in more detail.

2.1 Glass Transition Phenomena

2.1.1 Thermal Glass Transition

When an amorphous glass forming polymer is cooled, without crystallization, the density and viscosity increases while the molecular mobility decreases.⁵¹ At a certain temperature range, the segmental mobility for structural rearrangements becomes too low over experimentally accessible time scales. The liquid is then no longer in an equilibrium state. A glass is then formed, which is in a non-equilibrium state, without any long-range order.⁵² This process is called the thermal glass transition whereby this transition takes place in a given temperature range. The glass transition is a kinetic phenomenon and not a thermodynamic phase transition, which is explained by discontinuous changes in any physical property, in contrast to first and second order transitions.^{53,54}

Depending on the temperature, a polymeric system in the bulk could behave like an elastic solid, rubber-like, as a viscoelastic, highly deformable material or as a melt. The shear modulus G versus the temperature demonstrates this behavior as it is shown in Figure 2.1.

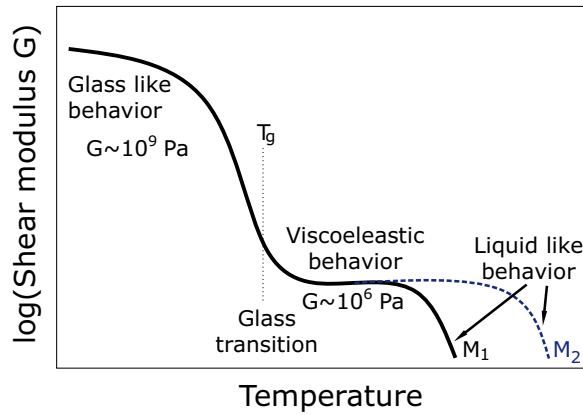


Figure 2.1 – Sketch of the shear modulus vs. the temperature for an amorphous polymer. Solid line represents a polymer with a molecular weight of $M_1 > M_c$ and the dashed line a polymer with $M_2 > M_1$ (based on ref.⁵⁵).

At low temperatures, the shear modulus is in the range of 10^9 Pa and the polymer shows an elastic-solid-like behavior. At the glass transition temperature T_g , the shear modulus rapidly decreases by ca. 3 orders of magnitude. For temperatures higher than T_g , the behavior of the polymer changes from glassy to viscoelastic and rubbery. Entanglements (topological interactions), which are formed for molecular weights M_w higher than the critical molecular weight M_c (for very flexible polymers about 10^4 g/mol) are responsible for this rubber-like plateau. With further increase of the temperature, the polymer behaves like an ordinary liquid, which indicates the shear modulus to be 0. As it can be seen from Figure 2.1 the viscoelastic behavior of a glassy polymer strongly depends on the molecular weight.

The glass transition temperature is a characteristic phenomenon for polymers. Besides the specific volume (see Figure 2.4), the typical temperature dependence (for a constant cooling rate) for a glassy polymer around T_g can also be observed for other thermodynamic quantities like the enthalpy and entropy (see Figure 2.2).

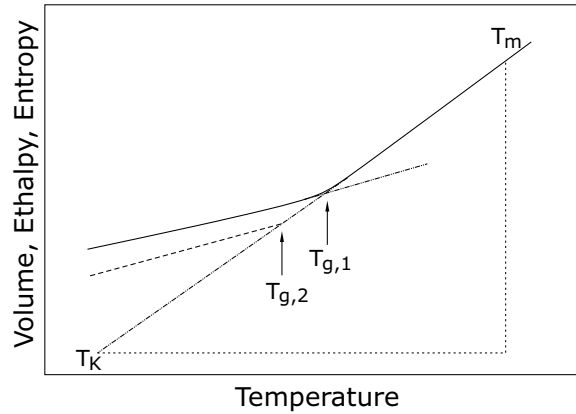


Figure 2.2 – Thermodynamic quantities like volume, enthalpy and entropy vs. temperature around the glass transition temperature T_g . $T_{g,1}$ and $T_{g,2}$ are for different cooling rates where $T_1 > T_2$. T_m characterizes a hypothetical melting point and T_K the Kauzmann temperature. (based on ref.⁵⁵)

With decreasing temperature down to T_g , the slope of the temperature dependence of the volume, entropy and enthalpy changes. At the same time, a step-like change can be observed for material properties like specific heat $c_p = (\partial H / \partial T)_p$ or thermal expansion coefficient $\alpha = (1/V)(\partial V / \partial T)_p$ (Figure 2.3), which is denoted as the thermal glass transition temperature.

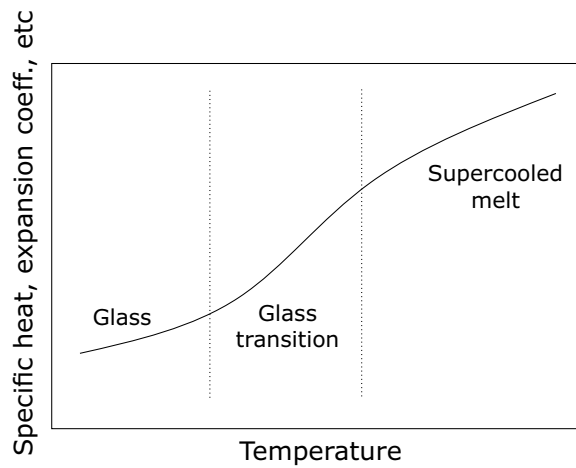


Figure 2.3 – Scheme of the temperature dependence of different material properties like specific heat and expansion coefficient for a glassy polymer.⁵⁵

In order to measure the thermal T_g methods like Differential Scanning Calorimetry (DSC),^{56,57} ellipsometry,^{58,59} etc. can be used.

The reduced molecular mobility below the glass transition temperature T_g leads to excess properties e.g. free volume, enthalpy, etc.. Figure 2.4 shows a scheme of the specific volume of a polymer as a function of the temperature above and below T_g .

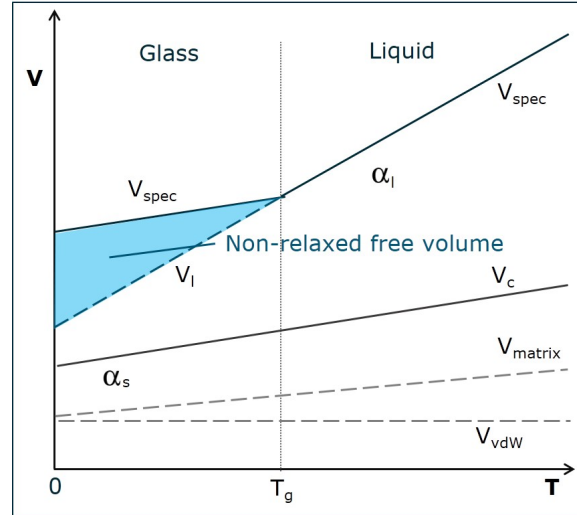


Figure 2.4 – The temperature dependence of the specific volume of a glassy polymer (based on ref.⁶⁰).

The specific volume V_{spec} decreases with decreasing temperature corresponding to the thermal expansion coefficient of the liquid state α_l . By passing T_g , cooperative movements freeze while smaller units of the polymer structure are still mobile and the liquid turns into a glass, retaining the internal structure of the rubbery state above T_g . In this temperature range, changes of the volume follow the thermal expansion coefficient of the solid α_s and due to the frozen-in segmental mobility additional free volume results. In general, the free volume is defined as the difference of the specific volume V_{spec} and the extrapolated volume of an undercooled liquid V_l as well as the matrix volume V_{matrix} . Non-relaxed free volume is characterized by the difference of the specific volume and V_l . Several occupied volumes may be subtracted from the specific volume V_{spec} to obtain the free volume:

1. $V_{spec} - V_{vdW}$: the van der Waals volume gives the free volume at 0 K.
2. $V_{spec} - V_c$: the volume of the hypothetical crystal (closed packed) gives the excess free volume.
3. $V_{spec} - V_l$: the extrapolated volume of an undercooled liquid gives the amount of unrelaxed free volume.

By calculating the so called fractional free volume Φ_{FV} , described by Bondi,⁶¹ the free volume of common glassy polymers is determined as:

$$\Phi_{FV} = \frac{V_{free}}{V_{spec}} = 1 - 1.3 \cdot \frac{V_{vdW}}{V_{spec}} \quad (2.1)$$

2.1.2 Dynamic Glass Transition

Molecular mobility is an important part of the glass formation process. In order to measure those segmental dynamics different techniques e.g. Dynamic Mechanical Analysis (DMA),⁵¹ neutron scattering⁶² and in a extremely wide frequency range by Broadband Dielectric Spectroscopy (BDS)⁶³ could be applied.

During the glass formation, different changes related to dynamical processes can be observed which are schematically shown in Figure 2.5 with the dielectric loss ϵ'' as an example.

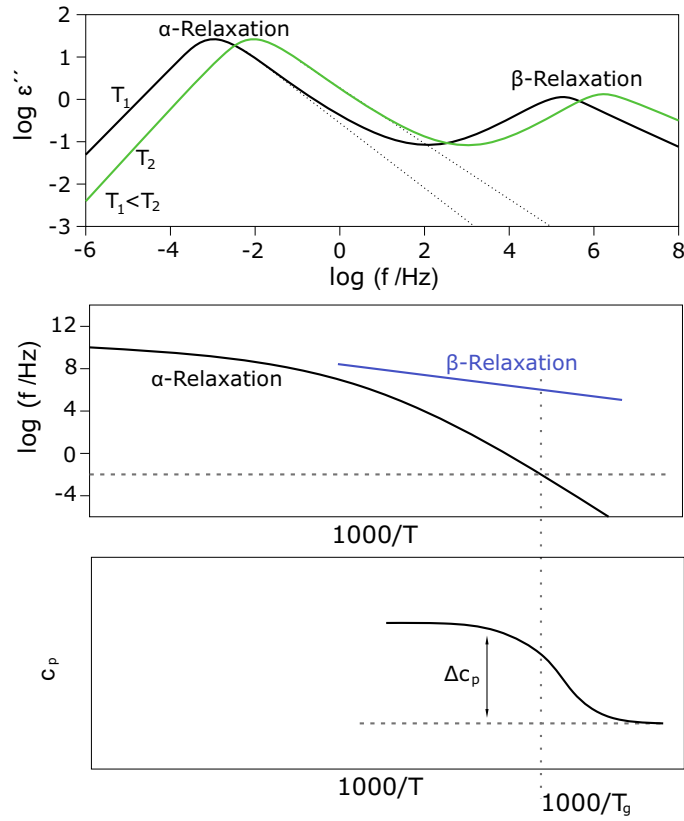


Figure 2.5 – Sketch of dynamics for glassy polymers around T_g . First, dielectric loss ε'' vs. frequency for two different temperature $T_1 < T_2$. Second, relaxation rate vs. inverse temperature for α and β -relaxation. Third, specific heat capacity vs. the inverse temperature (based on ref.⁵⁵).

Many polymers show processes at higher frequencies, for instance the β -relaxation. The temperature of this process can usually be described by an Arrhenius relation:

$$f(T) = \frac{1}{2\pi\tau_\beta(T)} = f_\infty \cdot \exp\left(-\frac{E_A}{k_B T}\right) \quad (2.2)$$

where E_A represents the activation energy, k_B the Boltzmann constant and f_∞ denotes the frequency in the high temperature limit ($f_\infty = (2\pi\tau_\infty)^{-1}$). Mostly, the β -process can be assigned to rotational fluctuations of side groups or other inter- and intramolecular fluctuations.⁵⁵

The α -relaxation (structural (primary) relaxation or dynamic glass transition) appears in the low frequency range (see Figure 2.5).⁵⁵ For polymers, this transition is due to segmental fluctuations and can be described by the empirical Vogel-Fulcher-

Tammann equation (VFT):^{64–66}

$$f(T) = \frac{1}{2\pi\tau_\alpha(T)} = f_\infty \cdot \exp\left(-\frac{A \cdot T_0}{T - T_0}\right) \quad (2.3)$$

where A characterizes the fragility parameter, which can be taken as a classification parameter for glassy polymers.^{67,68} When $f(T)$ deviates strongly from the Arrhenius type behavior, the polymer is called "fragile". While for temperature dependence similar to the latter the polymer is considered "strong". T_0 represents the Vogel or ideal glass transition temperature, which is found to be 30 to 70 K below the thermal glass transition temperature. The relaxation rate f_{max} ($f(T_g)$) reaches typical values of 10^{-2} – 10^{-3} Hz at T_g (see Figure 2.5).

2.2 Glassy Dynamics

2.2.1 Models for the Glass Transition

Up to now, there is no generally accepted theoretical approach describing all aspects of the glass transition.⁵⁵ In this section, the cooperativity approach by Adam and Gibbs⁶⁹ as well as the free volume theory by Doolittle⁷⁰ and Cohen^{71,72} are introduced, which justify the empirical VFT dependence, respectively.⁶³

2.2.1.1 Cooperativity Approach

The theory of Adam and Gibbs is based on the assumption of the existence of "Cooperatively Rearranging Regions (CRR)", which are defined as the smallest volume changing its configuration independently from neighboring regions.⁶³ The relaxation time is related to the number of particles as follows:

$$\frac{1}{\tau} \sim \exp\left(-\frac{z(T) \cdot \Delta E}{k_B T}\right) \quad (2.4)$$

where $z(T)$ characterizes the number of segments per CRR and ΔE denotes the free energy barrier for one molecule. $z(T)$ is related to the total configurational entropy

$S_c(T)$ by:

$$z(T) = \frac{S_c}{Nk_B \ln 2} \quad (2.5)$$

where N is the total number of segments and $k_B \ln 2$ characterizes the minimum of entropy of a CRR assuming a two state model. $S_c(T)$ can be related to the change of specific heat capacity Δc_p at T_g as follows:

$$S_c(T) = \int_{T_2}^T \frac{\Delta c_p}{T} dT \quad (2.6)$$

The VFT dependence can be obtained with the assumptions of $T_2=T_0$ and $\Delta c_p \approx C/T$ from eq. 2.4 and 2.6. When the size of a CRR diverges as $z(T) \sim (T - T_0)^{-1}$ the configurational entropy at T_0 , $S_c(T_0)$, disappears. Nevertheless, this cooperativity approach does not give any information about the absolute size for the CRR at T_g .

Donth developed a fluctuation approach^{54,73,74} where the height of the step in c_p and the temperature fluctuation ∂T of a CRR at T_g is connected with the correlation length ξ by:

$$\xi^3 \sim V_{CRR} = \frac{k_B T_g^2 \Delta \left(\frac{1}{c_p} \right)}{\rho (\partial T)^2} \quad (2.7)$$

where $\Delta(1/c_p)$ characterizes the step of the reciprocal specific heat (when $c_v \approx c_p$ is assumed), ρ the density and ∂T can be extracted experimentally from the width of the glass transition.^{75,76} Recently, broadband heat capacity spectroscopy enabled the estimation of ∂T .^{77,78} The size of a CRR for different polymers is about 1 – 3 nm (corresponding to 10 – 200 segments⁵⁵), which was estimated by Differential Scanning Calorimetry (DSC)⁷⁹ and Specific Heat Spectroscopy (SHS)^{80,81}

2.2.1.2 Free Volume Theory

The free volume theory (see also Figure 2.4) is based on four assumptions:^{55,63}

- Every segment of a polymer chain is assigned to a local volume V

- If V is larger than a critical value V_c , the surplus could be considered as free $V_{free} = V - V_c$
- Molecular transport is realized by a jump over a distance corresponding to the size of a molecule V_M ($\approx V_{vdW}$) when $V_{free} > V^* \approx V_M$ where V^* is the minimal free volume required for a jump of a segment (or molecule) between two sites
- The free volume can redistribute without any "cost" of energy

The statistics of this redistribution is assumed to follow the Boltzman statistic and V_{free} to be the total free volume of the system. Thus, the jump rate $1/\tau$ is defined by:

$$\frac{1}{\tau} \sim \int_{V^*}^{\infty} \exp\left(-\frac{V_{free}}{\bar{V}_{free}}\right) dV_{free} \sim \exp\left(-\frac{V^*}{\bar{V}_{free}}\right) \quad (2.8)$$

where \bar{V}_{free} denotes the average free volume. With a linear temperature dependence of the fractional free volume $\bar{f} = \bar{V}_{free}/V$, where V is the total volume:

$$\bar{f} = f_g + \alpha_f(T - T_g) \quad (2.9)$$

and temperature independence of $f^* = V^*/V$ the VFT equation can be obtained. f_g characterizes the fractional free volume at T_g and α_f denotes the thermal expansion coefficient. With the VFT equation (eq. 2.3) follows:

$$AT_0 = \frac{f^*}{\alpha_f} \cdot T_0 = T_g - \frac{f_g}{\alpha_f} \quad (2.10)$$

In this model T_0 is the temperature where the free volume disappears. The free volume model is able to describe the temperature dependence relaxations close to T_g but the fractional free volume cannot be obtained separately.

2.2.1.3 Dynamic and Free Volume Models related to Gas Transport Models

It has to be noted that the free volume model was used by Fujita⁸² as well as the cooperative approach by Schaefer et al.⁸³ in a similar way to describe the diffusion of low molecular penetrants through a membrane.

Whereas, Brandt's model⁸⁴ is based on the assumption that an intramolecular activation energy is required for bending two polymer chains away from each other and intermolecular energy to overcome the repulsion of the bending segments by their neighbors. For more details of those and more gas transport models see ref.⁸⁵

2.3 Gas Separation Membranes

Membranes in general offer high potential to reduce the energy consumption of separation processes because a phase change is often not required compared to conventional material separation techniques like distillation, crystallization, absorption or adsorption which are all thermal driven processes. Membrane technology is widely used for the separation of various mixtures varying in molecular or particle size, charge or affinity for the membrane. They find applications in medicine, power engineering, chemical industry and more.⁸⁵ Some membrane processes were established in the last decades, e.g. microfiltration (MF), ultrafiltration (UF), reverse osmoses (RO), electrodialysis (ED), pervaporation (PV) and gas separation (GS).

In the field of gas separation membranes diverse materials; organic, inorganic, porous, non-porous, find notable application. So why polymeric materials are of such a great interest? Porous materials offer a high permeability due to the pore flow but at the same time a bad selectivity. Inorganic solids like ceramics or metals show low solubilities and low diffusion because of their internal structure binding the penetrants. Whereby liquids provide high gas solubilities but low selectivities. Beside its good processability and low costs, compared to ceramics and metals, polymers offer high selectivity and permeability. For these reasons, polymeric membranes emerge as the favorable material for gas separation applications.

In general, the transport mechanism of a gas through a membrane depends on the internal structure of the membrane material, porous or non-porous membranes.

2.3.1 Diffusion Mechanism of Gases in Porous and Non-Porous Membranes

When the material is porous, the gas transport occurs by Poiseuille flow, Knudsen diffusion or molecular sieving (see Figure 2.6) depending on the ratio of pore diameter

and the mean free path of the gas molecules λ .

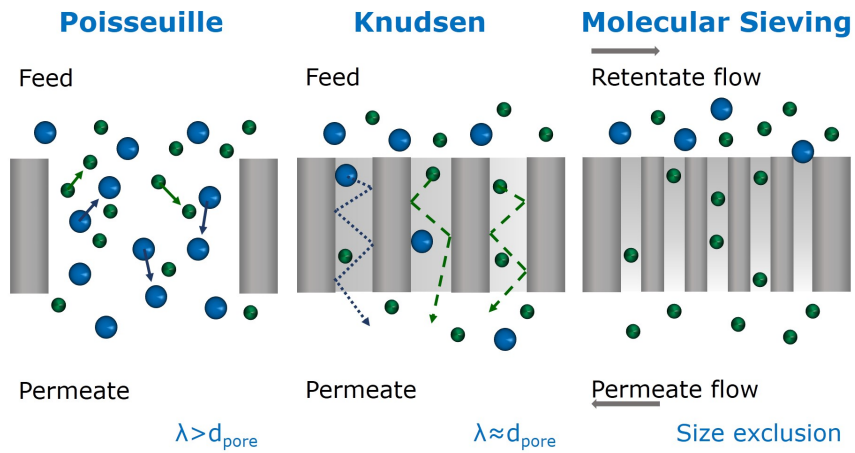


Figure 2.6 – Sketch of different gas transport mechanism through porous membranes (adapted from ref.⁸⁶).

When the pore diameter d_{pore} in membranes is larger than the mean free path λ of the gas molecules, Poiseuille flow takes place. If the pore size of the membranes is smaller than 50 – 100 Å, this diffusion is called Knudsen diffusion.⁸⁷ In the case of molecular sieving, the difference between pore diameter and gas molecule has to be less than 7 Å.

2.3.2 Gas Separation in Non-Porous Polymers

Diffusion in non-porous membranes occurs according to the solution-diffusion mechanism, where the driving force is a concentration gradient across the membrane. The solution-diffusion mechanism is divided into 3 steps (Figure 2.7):⁸⁸

- Sorption of the gas molecules at the so called upstream side (higher pressure = higher equilibrium concentration)
- Diffusion of the gas through the dense polymer across the concentration gradient
- Desorption of the gas molecules from the so called downstream side (lower pressure = lower equilibrium concentration)

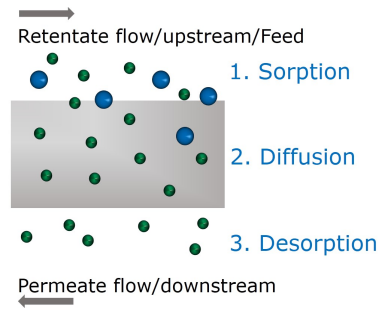


Figure 2.7 – Sketch of the Solution-Diffusion mechanism.

The diffusion in (isotropic) material is generally described by the first Fick's law:

$$J = -D \cdot \frac{\partial c}{\partial x} \quad (2.11)$$

where J denotes the net flux of diffusing material across unit area of a reference plane,⁵¹ x defines the space coordinate measured normal to the section, c is the concentration of diffusing substance and D characterizes the diffusion coefficient*. Eq. 2.11 is only valid for an isotropic medium where diffusion and structure properties are the same at any point within the material, which means that the diffusion coefficient is independent from the concentration and the position in the material, $D = \text{constant}$.

When the diffusion coefficient is constant and one dimensional (gradient of concentration only in x direction) but due to the mass transport time-dependent, Equation 2.11 becomes the second Fick's law:

$$\frac{\partial c}{\partial t} = -D \cdot \frac{\partial^2 c}{\partial x^2} \quad (2.12)$$

Plane Sheet

In case of diffusion into a plane sheet of material which is as thin as the effective diffusion of the substances enter only through the plane faces and negligible amounts through the edges⁸⁹ (see Figure2.8).

* In this work, "diffusion coefficient" is equal to the mutual diffusion where the driving force is a concentration gradient. Whereas, the tracer diffusion describes the statistical motion of a single particle.

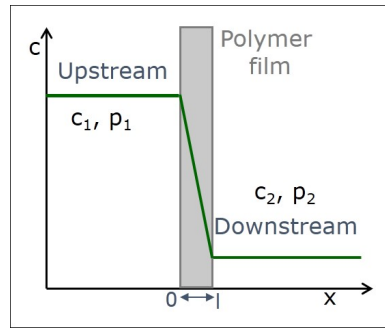


Figure 2.8 – Sketch of gas diffusion through a plane sheet with a thickness of l in the steady state. c_1 , p_1 and c_2 , p_2 are gas concentration and gas pressure at the upstream and downstream side of the membrane, respectively.

Steady State

After a certain time the concentration remains constant at any point of the sheet, the steady state (see Figure 2.8). With a membrane thickness of l (surfaces: $x = 0$ and $x = l$), with constant diffusion coefficient D and constant concentrations (c_1 (upstream) and c_2 (downstream)) the diffusion equation in one dimension (eq. 2.12) reduces to:⁸⁹

$$0 = \frac{d^2c}{dx^2} \quad (2.13)$$

By integrating to x :

$$\frac{dc}{dx} = \text{constant} \quad (2.14)$$

and with $x = 0$ and $x = l$ and with further integration:

$$\frac{c - c_1}{c_2 - c_1} = \frac{x}{l} \quad (2.15)$$

Eq. 2.14 and 2.15 show that the concentration gradient from c_1 to c_2 is linear, thus the molar flux in the steady state is given by:

$$J_{st} = -D \cdot \frac{dc}{dx} = D \cdot \frac{c_1 - c_2}{l} \quad (2.16)$$

The permeability coefficient P at a pressure difference of $\Delta p = p_1 - p_2$ through a

membrane of a thickness l analog to eq. 2.16 is given by:

$$J_{st} = P \cdot \frac{p_1 - p_2}{l} \quad (2.17)$$

where p_1 is the pressure of the upstream and p_2 the pressure of the downstream (see Figure 2.8).

If the diffusion coefficient is constant and the concentration c is proportional to the applied gas pressure (sorption isotherm is linear, Henry's law):

$$c = S \cdot p \quad (2.18)$$

eq. 2.16 and 2.17 are equivalent. S is the solubility and c denotes the concentration within the membrane which is in equilibrium with the external pressure p . With eq. 2.16 and 2.17 eq. 2.18 changes to:

$$P = D \cdot S \quad (2.19)$$

Transient State

When the initial concentration $c_0 = 0$, the upstream concentration $c_1 (= S \cdot p_1)$ is constant and the downstream pressure $p_2 = c_2 = 0$, the concentration profile in the material changes until it is constant (see Figure 2.9).

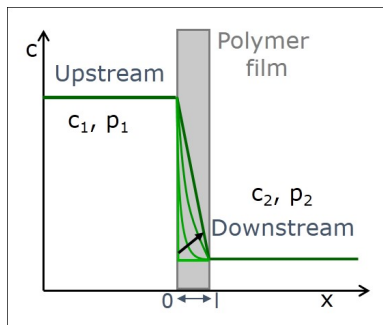


Figure 2.9 – Concentration gradient within a material for a transient to steady state diffusion.

The time until the steady state is reached depends on the diffusion coefficient which determines the speed. If the diffusion coefficient is constant and independent from

the concentration the concentration gradient can be calculated as a function of x and t .⁸⁹ The amount of permeated gas is given by:

$$Q_t = \int_0^t \left(\frac{dV_{gas}^0}{dt} \right) dt = V_{m,gas}^0 \int_0^t \left(\frac{dn}{dt} \right) dt = F \cdot V_{m,gas}^0 \int_0^t J_{st} dt \quad (2.20)$$

$$\Rightarrow \frac{Q_t}{l \cdot c_1} = \frac{D \cdot t}{l^2} - \frac{1}{6} - \frac{2}{\pi^2} \sum_1^{\infty} \frac{(-1)^n}{n^2} \exp \left(\frac{-D \cdot n^2 \cdot \pi^2 \cdot t}{l^2} \right) \quad (2.21)$$

where V_{gas}^0 characterizes the volume of a gas under standard conditions (STP: $T_{STP} = 273.15$ K and $p_{STP} = 1.013$ bar) and $V_{m,gas}^0 = 22.4$ cm³/mol denotes the molar volume for an ideal gas. With $t \rightarrow \infty$ (steady state) eq. 2.21 reduces to:

$$Q_t = \frac{D \cdot c_1}{l} \cdot \left(t - \frac{l^2}{6 \cdot D} \right) \quad (2.22)$$

and Q_t changes to the steady state region (Figure 2.10).

Time-Lag Experiment

Figure 2.10 presents a schematic time-lag experiment curve including additional boundary conditions which are maintained for a time-lag experiment:

$$t < 0 \quad 0 \leq x \leq l \quad c = 0$$

$$t = 0 \quad x = 0 \quad c = S \cdot p_1$$

$$t = 0 \quad x = l \quad c = 0$$

$$t > 0 \quad 0 \leq x \leq l \quad c = f(x,t)$$

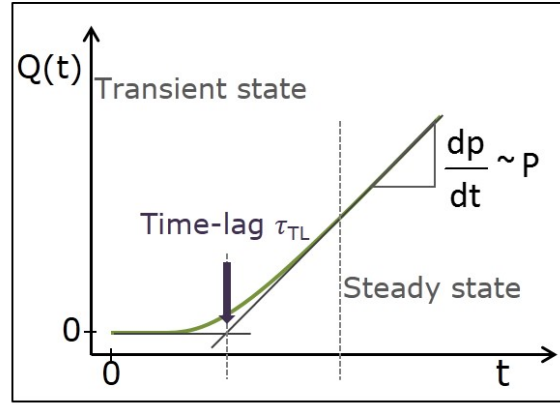


Figure 2.10 – Schematic time-lag measurement curve.

With the boundary conditions eq.2.17 is reduced to:

$$J_{st} = P \cdot \frac{p_1}{l} \quad (2.23)$$

and thus, the permeability is described by:

$$P = J_{st} \cdot \frac{l}{p_1} \quad (2.24)$$

With $Q_t = 0$ and $t = \tau_{TL}$ Eq. 2.22 becomes to: :

$$\tau_{TL} = \frac{l^2}{6 \cdot D} \quad (2.25)$$

where the so called time-lag τ_{TL} describes the intersection of the extrapolated steady-state line with the x-axis (Figure 2.10), which can be used to determine the diffusion coefficient:

$$D = \frac{l^2}{6\tau_{TL}} \quad (2.26)$$

Below T_g the segmental mobility of a glassy polymer is limited (section 2.1) and thus, full thermodynamic equilibration after the gas sorption is not possible. This leads to a pressure-dependence of P and D where τ_{TL} is not only correlated to the diffusion coefficient while the concentration must be constant. Thus, the diffusion coefficient

D, determined from the time-lag τ_{TL} , is an effective diffusion coefficient D_{eff} :

$$D_{eff} = \frac{l^2}{6\tau_{TL}} \quad (2.27)$$

In the following the effective diffusion coefficient D_{eff} is denoted even below T_g simplified as D.

2.3.3 Sorption in Glassy Polymers: Dual Mode Behavior

In order to describe sorption of gas molecules in glassy polymers several models were developed, whereas none is able to explain all phenomena observed experimentally (like gas-induced swelling and plasticization), completely and satisfactorily. However, due to its easy applicability the Dual Mode sorption model is commonly used for various polymer gas systems.^{90,91} This model is a combination of a Henry solution and a Langmuir adsorption (see Figure 2.11).

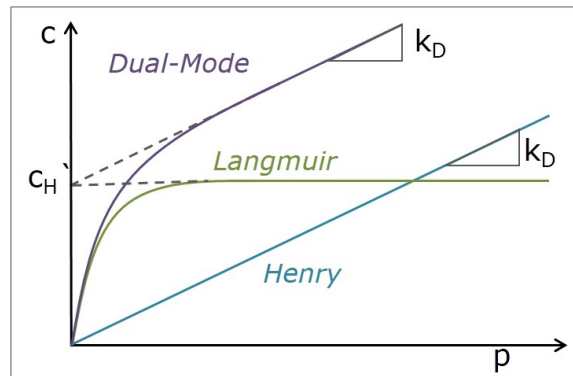


Figure 2.11 – Sorption isotherms for Henry, Langmuir and Dual-Mode.

The idea of the Dual-Mode model is based on the specific internal structure of a glassy polymer (see Figure 2.4). Below T_g the reduced segmental mobility lead to accessible unrelaxed free volume (see Figure 2.4) providing "micro holes". Thus, additionally to the Henry sorption (like in elastomers and rubbers), a hole-filling mechanism described by a Langmuir mechanism is assumed. Consequently, this leads to two different kinds of sorbed gas molecules: $C_{D(issolved)}$ and $C_{H(oles)}$.

$c_{D(issolved)}$ is linear relation to the pressure where the solubility coefficient is constant (Henry-constant k_D). This behavior is described by Henry's law:

$$c_D(p) = k_D \cdot p \quad (2.28)$$

where c_D is the concentration of the penetrant in the polymer, k_D characterizes the Henry-constant and p denotes the pressure. The Langmuir sorption $c_{H(oles)}$ can be regarded as a hole-filling mechanism in the additional unrelaxed free volume and is described by Langmuir isotherm:

$$c_H(p) = \frac{c'_H \cdot b \cdot p}{1 + b \cdot p} \quad (2.29)$$

where c'_H is the saturation capacity and b the affinity constant (quotient of ad- and desorption rate).

In conclusion, the total concentration of a sorbed gas in a glassy polymer follows a combination of equation 2.28 and 2.29, the Dual-Mode model:^{90,92}

$$c(p) = c_D + c_H = k_D \cdot p + \frac{c'_H \cdot b \cdot p}{1 + b \cdot p} \quad (2.30)$$

Whereupon, this sorption isotherm for glassy polymers is dominated for low p by the hole filling mechanism (Langmuir) and for higher p by Henry sorption because the Langmuir term reached already its saturation level (see Figure 2.11).

2.3.4 Effects of Permeant

Size and Shape

Glassy polymers offer high selectivities due to their high diffusivity selectivity. The diffusion coefficient depends on the size and the shape of the penetrant. The gas molecule "jumps" through the polymer matrix when the size of the gas molecule is practicable with the polymer gaps. In general, the diffusion coefficient increases with decreasing size of the penetrant. Furthermore, the shape of the gas molecules is an important factor. The kinetic diameter σ_{kin} is calculated from the minimum equilibrium cross-sectional diameter of the gas molecule⁹³ and is a parameter used for a comparison of different gases. Rod-like molecules such as CO_2 show increased

diffusion coefficients compared to spherical molecules such as CH₄⁹⁴ which can be explained by the smaller kinetic diameter of CO₂ compared to CH₄.

Table 2.1 – Kinetic diameter and critical temperature of H₂, N₂, O₂, CH₄ and CO₂.

	H ₂	N ₂	O ₂	CH ₄	CO ₂
Kinetic diameter σ_{kin} /Å	2.89	3.64	3.46	3.80	3.30
Critical temperature T_c /K	33.3	126.2	154.6	190.7	304.2

Condensability

The condensability of the gas influences the solubility because the van der Waals interaction depends on the polarizability of the gas molecules. The gas solubility increases with increasing gas condensability, which is related to the critical temperature T_c (Table 2.1); the higher T_c , the higher is the solubility. The condensability (solubility) is competitive to the size of the penetrant (diffusivity) in separation processes. One example is the challenging separation of CO₂ and H₂. On the one hand, H₂ has a higher diffusivity than CO₂. But on the other hand, the solubility of CO₂ is higher compared to H₂. Due to those two competitive driving forces the separation of CO₂ and H₂ is difficult.

2.3.5 Effects of Temperature

The temperature dependence of the sorption process is described by the van't Hoff equation:

$$S(T) = S_0 \cdot \exp\left(-\frac{\Delta H_S}{RT}\right) \quad (2.31)$$

where S_0 is a constant ($S(T \rightarrow \infty) = S_0$) and ΔH_S is the partial molar enthalpy of sorption. The temperature dependence the diffusion can be described by the Arrhenius relation:

$$D(T) = D_0 \cdot \exp\left(-\frac{E_{A,D}}{RT}\right) \quad (2.32)$$

where D_0 is a constant ($D(T \rightarrow \infty) = D_0$) and $E_{A,D}$ characterizes the activation energy of the diffusion. R denotes the universal gas constant ($R = 8.314 \text{ J}/(\text{mol K})$).

2.3.6 Challenges and Limits of Technology

The flux, permeability and selectivity are key factors of the transport performance of polymeric membranes.⁶ The flux can be influenced by the type (permeability) and the effective thickness of the polymer. However, the selectivity (eq. 2.33) depends on the choice of the polymer but also on the producibility of- preferably very thin- "pinhole-free" membranes. Permeability and selectivity are key material properties to be considered for the applicability of a polymer as a potential gas separation material, whereas the thickness is a fabrication parameter. From all those structure/property relationship studies, a trade-off relationship between selectivity and permeability emerged. A concept named "upper bound" was identified by Robeson based on a large amount of collected experimental data. This model includes plots of log of the selectivity versus log permeability (of the gas with the higher permeability); where all data points seem to be located below a well defined limiting line.^{11,12,95} Figure 2.12 shows an example of such upper bound (also called Robeson plot) for CO_2/CH_4 . The ideal selectivity is defined as the quotient of the pure gas permeabilities:

$$\alpha_{i,j}^{id} = \frac{P_i}{P_j} \quad (2.33)$$

where P_i and P_j are the permeabilities of pure gases i and j , respectively. It has to be noted that the real selectivity can differ strongly from the ideal one.

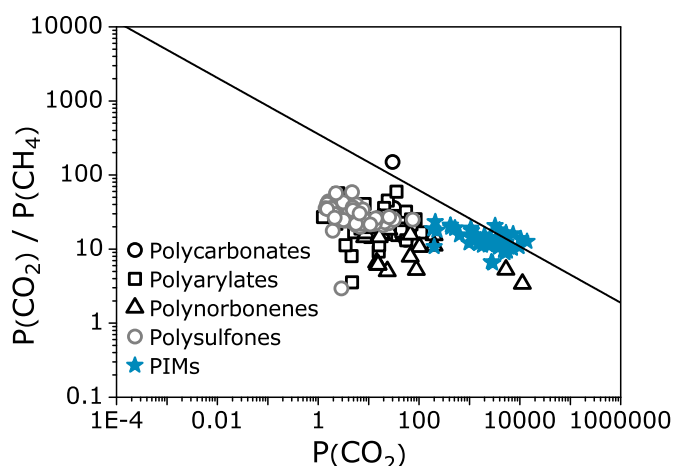


Figure 2.12 – Selectivity of CO₂ against CH₄ vs. permeability of CO₂ plotted in a so called Robeson plot. The data was provided by ref.⁹⁶

Besides the permeability/selectivity trade-off as a "widely recognized challenge",⁶ physical aging is a significant material property compromising the industrial viability of many potentially effective membrane polymers. Glassy polymers are often used as gas separation materials.^{97,98} Glassy polymers offer excess free volume due to decreased polymer segmental mobility below the glass transition temperature T_g (see section 2.1). Due to their non-equilibrium state, the polymer undergoes slow, localized segmental motions towards the equilibrium leading to a higher density.⁹⁹ Hence, a reduced free volume causing a decrease in the gas permeability. Besides the permeability, other physical properties e.g. specific volume, enthalpy, entropy, etc. are altered (section 2.1).

This aging effect can also be induced or intensified by highly soluble gases such as CO₂. Those gases lead to a plasticization effect where the polymer structure swells with increasing gas concentration and the molecular mobility of the polymer matrix is enhanced.

In order to handle these described challenges it is important to understand the mechanism of gas transport through polymeric membranes as well as dynamics in polymers. For these reasons in this study gas transport experiments are combined with measurements of the molecular mobility.

3 Methods

3.1 Broadband Dielectric Spectroscopy (BDS)

Broadband Dielectric Spectroscopy (BDS) probes the interaction of an electrical field with matter (liquids and solids), in a non-destructive way, in a broad frequency range (10^{-6} Hz to 10^{12} Hz). In this frequency range, relaxation phenomena caused by fluctuations of dipoles and drift motion of mobile charge carriers can be observed.

3.1.1 Theoretical Background

Detailed discussion of the following considerations can be found in ref.⁶³

When an electrical field is applied to a material, a dielectric displacement in the material is the result. For small electric field strengths E , the dielectric displacement D_{diel} is defined as:

$$D_{diel} = \varepsilon^* \cdot \varepsilon_0 \cdot E \quad (3.1)$$

where ε^* denotes the complex dielectric function or dielectric permittivity, ε_0 characterizes the dielectric permittivity of the vacuum ($8.854 \cdot 10^{-12} \text{ A} \cdot \text{s} \cdot \text{V}^{-1} \cdot \text{m}^{-1}$) and E the applied electric field. The resulting dielectric displacement within the material due to the application of an electrical field is described by the polarization:

$$\hat{P} = D_{diel} - D_{diel,0} = (\varepsilon^* - 1) \cdot \varepsilon_0 \cdot E \quad (3.2)$$

where $D_{diel,0}$ denotes the dielectric displacement of the free space. Furthermore, $(\varepsilon^* - 1)$ defines the dielectric susceptibility χ^* of the material. When a periodic

electrical field (eq. 3.3) is applied to the system

$$E(t) = E_0 \exp(-i\omega t) \quad (3.3)$$

where $E(t)$ characterizes the outer electrical field, t the time, E_0 denotes the alternating electric field amplitude, ω the angular frequency and, $i^2 = -1$, the permittivity of the material is expressed by a complex function ϵ^* consisting of a real part (in-phase response) proportional to the reversible stored energy and an imaginary part (90° out-of-phase response) related to the energy loss per cycle. This complex dielectric function ϵ^* is given by:

$$\epsilon^*(\omega) = \epsilon'(\omega) - i\epsilon''(\omega) \quad (3.4)$$

where ϵ' is the real part, ϵ'' the imaginary part and ω the radial frequency ($f = \omega/2\pi$). Conductivity contributions could be analyzed with the complex conductivity σ^* is defined as:

$$\sigma^* = \sigma'(\omega) + i\sigma''(\omega) = i\omega\epsilon_0\epsilon^*(\omega) \quad (3.5)$$

where $\sigma'(\omega)$ and $\sigma''(\omega)$ are the real and imaginary part of σ^* . The real and imaginary part are described as:

$$\sigma'(\omega) = \omega\epsilon_0\epsilon''(\omega) \quad (3.6)$$

$$\sigma''(\omega) = \omega\epsilon_0\epsilon'(\omega) \quad (3.7)$$

3.1.2 Dielectric Response

Different relaxation phenomena contribute to the total dielectric response. Those phenomena could be related either to molecular fluctuations of dipoles or mobile charge carriers within the whole matrix or at interfaces (conductivity contributions). Each of them shows a characteristic frequency and temperature dependence of the real and imaginary part.

Macroscopic polarization refers to microscopic dipole moments p_i of molecules or particles within a volume V . Whereby, the microscopic dipoles can either be perma-

nent or induced. Induced dipole moments caused by a local electric field can be distinguished by the shift of the electron cloud respecting to the nuclei. Depending on the time scale, electronic (10^{-12} s) or atomic polarizations (longer time scales) are examples which are not considered here.

When an electrical field is applied to a system dipoles try to orientate along the direction of the field E which is called orientation polarization. At low frequencies, almost all molecular dipoles can follow the outer electrical field with the same frequency or time constant. Whereupon, with increasing frequency the fluctuation is retarded to fluctuate with the same frequency as the dipoles are attached to molecules or are hindered by the surrounding matrix. A characteristic time— the relaxation time τ — refers to each of theses two phenomena. All these processes depend on temperature.

For dielectrics, the response of a system to a disturbance (here the time-dependent external electrical field $E(t)$) is the polarization and can be characterized by a linear equation.⁶³

$$\hat{P}(t) = \hat{P}_{\infty} + \epsilon_0 \int_{-\infty}^t \epsilon(t - t') \frac{dE(t')}{dt'} dt' \quad (3.8)$$

where \hat{P}_{∞} characterizes all contributions arising from induced polarization and $\epsilon(t)$ denotes the time dependent dielectric function. By applying a periodical disturbance $E(\omega) = E_0 \exp(-i\omega t)$ with ω as the angular frequency, the polarization as response is described by:

$$\hat{P}(\omega) = \epsilon_0 \cdot (\epsilon^*(\omega) - 1) \cdot E(\omega) \quad (3.9)$$

The time dependent dielectric function $\epsilon(t)$ and the complex dielectric function $\epsilon^*(\omega)$ are correlated by an one-sided Fourier transformation.

Molecular fluctuations arises from localized, segmental and/or cooperative motion of the whole polymer chain¹⁰⁰ (see Figure 3.1).

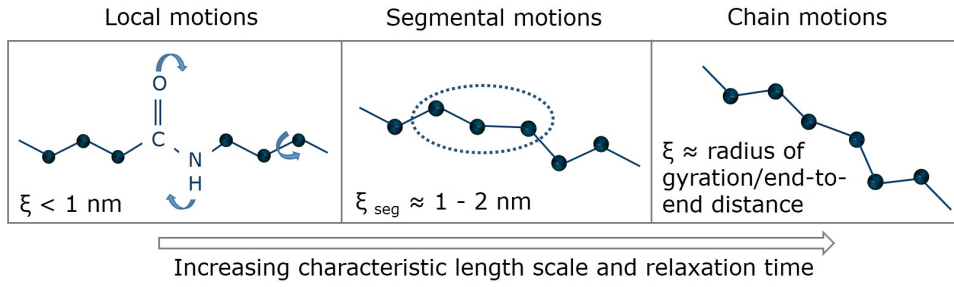


Figure 3.1 – Different molecular motions within a polymer (adapted from ref.¹⁰¹).

Localized fluctuations can take place within a monomeric unit or arise from rotation of a short side of the chain on a length scale of $\xi < 1 \text{ nm}$. Usually, those secondary processes are named as β and γ -relaxations and take place at high frequencies or low temperatures. In contrast, segmental motions are observed at lower frequencies and higher temperatures and on length scales of $\xi \approx 1 - 2 \text{ nm}$. They are related to the glass transition temperature. This primary process is called α -relaxation. With increasing temperature, this relaxation process shifts to higher frequencies.

Besides the molecular fluctuations, separation or motion of charge carriers contribute to the total dielectric response as well. Mobile charge carriers such as electrons, ions or charged defects can migrate through the material leading to conductivity contributions.

In phase separated morphologies, charge carriers can be separated on a mesoscopic length scale at the phase boundaries, leading to an interfacial polarization– the Maxwell-Wagner-Sillars (MWS) polarization. The relaxation time of the Maxwell-Wagner-Sillars polarization is inverse proportional to the conductivity of the material. The relaxation time decreases with increasing conductivity. Thus, the process is shifted to lower temperatures respectively higher frequencies. In some cases, the analysis of the MWS polarization is complicate, as sometimes this process arises in a similar temperature/frequency range with other relaxation processes.^{63,102,103} Furthermore, charge carriers can be separated at the external electrodes on a macroscopic scale– the electrode polarization.⁶³

3.1.3 Analysis of Dielectric Spectra

Each of the processes contributing to the total dielectric response show specific temperature and frequency dependencies of the real and imaginary part of the complex dielectric function (eq. 3.4). In the following section, the analysis and the dielectric spectra of isothermal frequency scans are discussed.

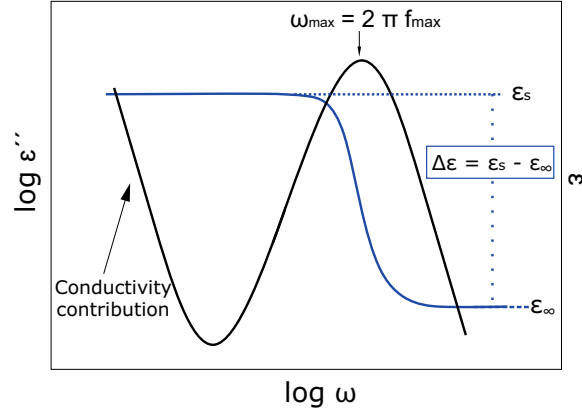


Figure 3.2 – Real $\epsilon'(\omega)$ (blue) and imaginary part $\epsilon''(\omega)$ (black) of the complex dielectric function (eq. 3.4) for a Debye relaxation process. (based on ref.⁶³)

A peak in the imaginary part (loss part) $\epsilon''(\omega)$ and a step-like decrease in the real part $\epsilon'(\omega)$ indicates a relaxation process (Figure 3.2). MWS polarization and conductivity phenomena are identified by an increase of the imaginary part $\epsilon''(\omega)$ with decreasing frequency. Real and imaginary parts are connected by the Kramers/Kronig relations.^{104,105}

The shape of the imaginary part gives information about the distribution of relaxation times. The dielectric strength $\Delta\epsilon$ could be calculated from the step in the real part $\epsilon'(\omega)$ and/or the area under the imaginary part $\epsilon''(\omega)$. The relaxation rate $\omega_{\max} = 2\pi f_{\max}$ or relaxation time $\tau_p = 1/\omega_{\max}$ is characterized by the position of the maximal loss (see Figure 3.2).

Several model functions were developed to analyze dielectric spectra. The simplest model was introduced by Debye¹⁰⁶ where non-interacting dipoles are assumed, leading to an ideal relaxation behavior. In frequency domain, the Debye function is given as follows:

$$\epsilon^*(\omega) = \epsilon_\infty + \frac{\Delta\epsilon}{1 + i\omega\tau_D} \quad (3.10)$$

where $\Delta\epsilon = \epsilon_S - \epsilon_\infty$ denotes the dielectric strength with $\epsilon_S = \lim_{\omega\tau \ll 1} \epsilon'(\omega)$ corresponding to the static permittivity and $\epsilon_\infty = \lim_{\omega\tau \gg 1} \epsilon'(\omega)$ characterizing the unrelaxed permittivity. ϵ_∞ is identified by a plateau in the real part. The Debye relaxation time (τ_D) is determined by $\omega_{max} = 2\pi f_{max} = 1/\tau_D$.

In general, the dielectric behavior of polymers cannot be described by the Debye function. Typically, the peaks for polymeric materials are much broader and of an asymmetric shape. This is named as non-Debye or non-ideal relaxation behavior. A number of model functions have been developed to describe the broadening of the loss peaks, for instance the Cole/Cole function.¹⁰⁷ Compared to eq. 3.10, the Cole/Cole model describes symmetric broadening of the dielectric function:

$$\epsilon^*(\omega) = \epsilon_\infty + \frac{\Delta\epsilon}{1 + (i\omega\tau_{CC})^\beta} \quad (3.11)$$

where $0 < \beta \leq 1$ characterizes the symmetric broadening of ϵ^* for $\beta = 1$, the Debye function is obtained again. The Cole/Cole relaxation time τ_{CC} is connected to the maximum of ϵ'' by $\tau_{CC} = 1/\omega_{max} = 1/(2\pi f_{max})$.

The Havriliak-Negami function (HN function) is used to describe both asymmetry and the broadening of the dielectric function.^{63,108,109}

$$\epsilon_{HN}^* = \epsilon_\infty + \frac{\Delta\epsilon}{\left[1 + (i\omega\tau_{HN})^\beta\right]^\gamma} \quad (3.12)$$

where τ_{HN} denotes the Havriliak-Negami relaxation time related to the frequency of maximal loss f_{max} . ϵ_∞ characterizes the value of the real part ϵ' for $f \gg 1/\tau_{HN}$, $\Delta\epsilon$ is the dielectric strength, ω the radial frequency ($\omega = 2\pi$), and β, γ ($0 < \beta; \beta\gamma \leq 1$) represents the asymmetry and broadening of the spectra compared to the Debye function.⁶³ The maximal loss f_{max} is related to the HN relaxation time by:^{108,110}

$$f_{max} = \frac{\omega}{2\pi} = \frac{1}{2\pi\tau_{HN}} \sin\left(\frac{\pi\beta}{2+2\gamma}\right)^{\frac{1}{\beta}} \sin\left(\frac{\pi\beta\gamma}{2+2\gamma}\right)^{-\frac{1}{\beta}} \quad (3.13)$$

The temperature dependence of f_{max} can be described either by Arrhenius (eq. 2.2) or the empirical Vogel-Fulcher-Tammann equation (VFT) (eq. 2.3).

Conductivity effects are treated in the usual way by adding a power law:

$$\epsilon''_{cond} = a \cdot \frac{\sigma_0}{\omega^s \cdot \epsilon_0} \quad (3.14)$$

with ($0 < s \leq 1$) to the dielectric loss (see Fig. 3.3). Where ϵ_0 is the permittivity of the free space ($= 8.854 \times 10^{-12} \text{ As V}^{-1} \text{ m}^{-1}$). σ_0 is the DC conductivity of the sample. For dimensional reason the factor a has the unit $(\text{rad} \cdot \text{s}^{-1})^{s-1}$. The parameter s ($0 < s \leq 1$) describes for $s = 1$ Ohmic and for $s < 1$ non-Ohmic effects in the conductivity.^{111,112}

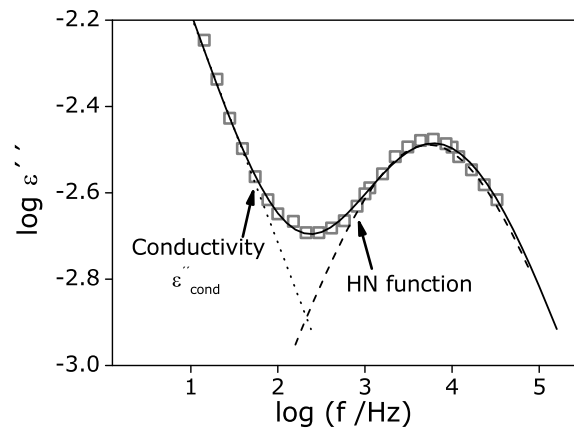


Figure 3.3 – Dielectric loss vs. frequency for PIM-1 (PIM-1-00) for 494 K. The line is a fit of the HN function to the data.

The frequency dependence of the real part of the complex conductivity spectra for a typical behavior expected for semi-conducting polymeric materials is shown in Figure 3.4.

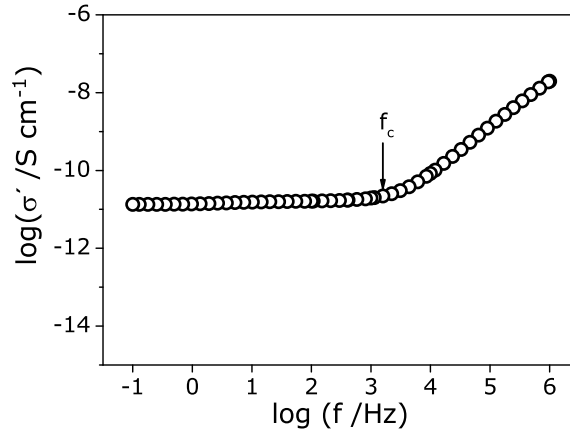


Figure 3.4 – Real part of the complex conductivity σ' vs. frequency for the second cooling run for pure Matrimid (MI-00) at 570 K.

For high frequencies, the real part σ' decreases with decreasing frequency with a power law down to a characteristic frequency f_c , where a plateau value is reached. The plateau value corresponds to the DC conductivity.¹¹¹ In literature, there are several models available to describe the frequency dependence of the real part of the complex conductivity quantitatively. One example is the Dyre model, where the conductivity is considered as a hopping process in a random free energy landscape.¹¹³ In a more simplified approach, the data can be approximated by the well-known Jonscher power law:¹¹⁴

$$\sigma'(f) = \sigma_{DC} \left[1 + \left(\frac{f}{f_c} \right)^n \right] \quad (3.15)$$

The critical frequency f_c characterizes the onset of the dispersion and the exponent n has values between 0.5 and 1. σ_{DC} can be obtained by fitting the Jonscher equation to the data.

3.1.4 Dielectric Measurements

For a capacitor with a dielectric within, the complex dielectric function is defined as:

$$\epsilon^*(\omega) = \frac{C^*(\omega)}{C_0} \quad (3.16)$$

where C^* denotes the complex capacitance of the filled capacitor and C_0 the geometrical capacitance (vacuum capacitance). The complex dielectric function can be

obtained by the measurement of the complex impedance Z^* of the sample:

$$\epsilon^*(\omega) = \frac{1}{i \cdot \omega \cdot Z^*(\omega) \cdot C_0} \quad (3.17)$$

A high resolution ALPHA analyzer interfaced to an active sample head (Novocontrol, Montabaur, Germany) was used to measure the complex dielectric function in a frequency range from 10^{-1} to 10^6 Hz. The samples were measure in parallel plate geometry (see Figure 3.5).

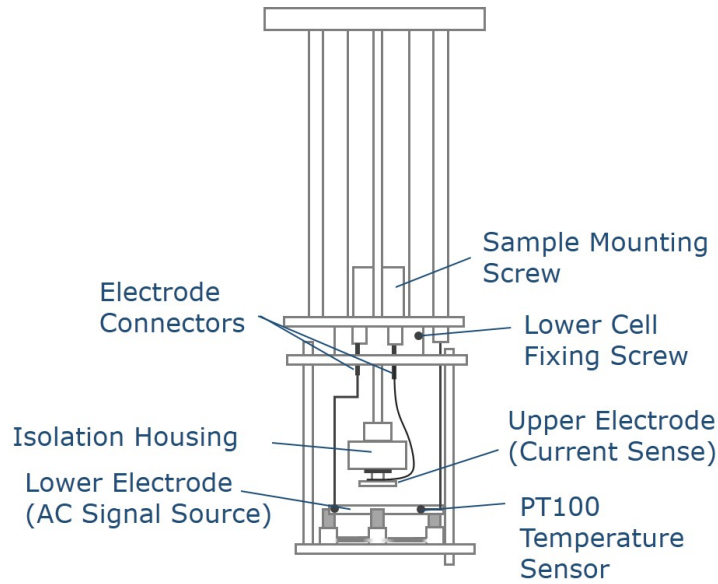


Figure 3.5 – Sketch of the sample holder of a Broadband Dielectric Spectroscopy set up.

In order to ensure a good electrical contact, gold-electrodes with a diameter of 20 mm were thermally deposited on both sites of the sample. The measurements were carried out by isothermal frequency scans at selected temperatures. To determine the influence of the temperature treatment on the structure of the sample, a detailed temperature program with several heating and cooling cycles from 173 K to 573 K ($\Delta T=3$ K) for the Matrimid samples (Figure 3.6a) and from 173 K to 523 K ($\Delta T=3$ K or 5 K) for the PIM-1 samples (Figure 3.6b) was used. The temperature was controlled by a Quatro Novocontrol cryo-system with a stability of 0.1 K. For more details see ref.⁶³ During the whole temperature program the sample was kept in a dry nitrogen atmosphere.

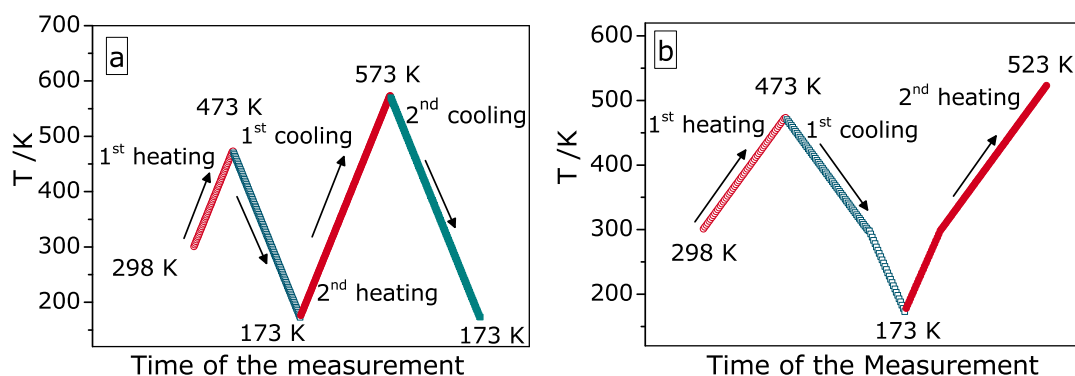


Figure 3.6 – Heating/cooling cycles of the dielectric measurements on a) Matrimid and Matrimid/POSS and b) PIM-1 and PIM-1/POSS.

3.2 Permeation: Time-Lag Method

In order to measure the gas permeability of different gases for Matrimid, PIM-1 and their composites the time-lag method was applied (details can be found in section 2.3). Figure 3.7 shows a flow sheet of the used time-lag set up.

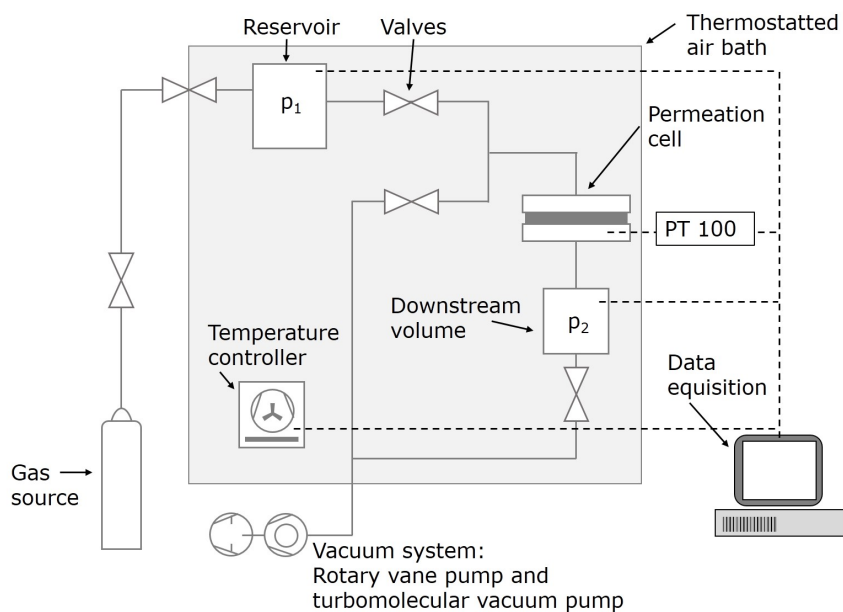


Figure 3.7 – Flow sheet of the used time-lag method.

The dense, defect free polymer film (diameter 38 mm) is placed in a permeation cell on a porous metal support in a temperature-controlled set-up and subsequently

sealed by a Viton O-ring. Before the measurements (start by feeding the probe gas p_1 to the upstream part of the permeation cell) the whole permeation cell and the film are carefully degassed. The downstream pressure increase, due to accumulation of permeating gas in the closed downstream volume, is measured with a temperature-controlled MKS Baratron gauge (128 A, 10 mbar range) and recorded as function of time.¹¹⁵ Figure 3.8 gives an example curve of the downstream pressure p_2 vs. the time for Matrimid.

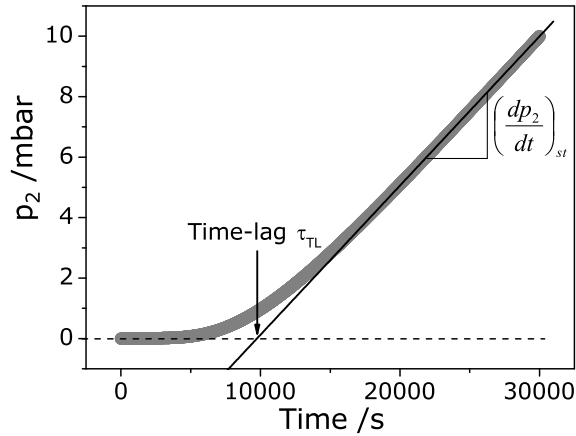


Figure 3.8 – Example curve of Matrimid at a CH_4 pressure of 10 bar and 35 °C.

In a time-lag experiment the permeability coefficient P is estimated from the slope of the steady state with the general definition of the molar flux through a membrane $J = 1/F \cdot (dn/dt)$ and with eq. 2.23:^{90,92,115,116}

$$P = \frac{V \cdot l \cdot T_{STP}}{F \cdot T \cdot p_1 \cdot p_{STP}} \left(\frac{dp_2}{dt} \right)_{st} \quad (3.18)$$

where V denotes the constant downstream volume, F the effective sample area, T the temperature, l the sample film thickness, p_1 characterizes the upstream pressure, T_{STP} is 273.15 K, p_{STP} is 1.013 bar and $(dp_2/dt)_{st}$ the steady state downstream pressure increase. The permeability coefficients are given in Barrer, which is defined as:

$$1 \text{ Barrer} = 10^{-10} \left(\frac{\text{cm}^3 (\text{STP}) \text{ cm}}{\text{cm}^2 \text{ cmHg s}} \right) \quad (3.19)$$

Diffusion coefficients can be estimated by the time-lag τ_{TL} as it was shown in eq. 2.26.

3.3 Density

Method 1

The density of the Matrimid and Matrimid/PhenethylPOSS samples was measured by the immersion method (ISO 1183-1:2004(E)). A MC410 S analytical balance (Satorius, Göttingen, Germany) and the associated YDK 01 LP density determination kit were used. The samples were weighed in air and n-heptane at room temperature.

Method 2

For the determination of the density of PIM-1 and PIM-1/PhenethylPOSS sample a density gradient column (DGC) was used according to DIN 53479 at 296.15 K. Solutions of calcium nitrate $\text{Ca}(\text{NO}_3)_2$ in ethanol were prepared to obtain a density range of 1.1 to 1.4 cm^3/g . For the calibration of the DGC glass floats with defined densities were used. The correlation of position (height) in the density gradient column with density was linear and interpolation was performed by linear regression. For each material sample two specimens were measured.

3.4 Differential Scanning Calorimetry

Differential scanning calorimetry (DSC) was applied for the thermal analysis (DSC 204 F1 Phoenix, Netzsch). The samples were measured in the temperature range from 223 K to 673 K with a heating rate of 10 K/min under nitrogen.

3.5 Dynamic Mechanical Analysis

For dynamic mechanical analysis (DMA), a DMA 242 D (Netzsch) was used in tensile mode. The complex elastic modulus E^* and the complex strain compliance D^* were measured, with a temperature rate of 1 K/min, in the frequency sweep mode between 0.1 – 10 Hz and in the temperature range of 263 K to 573 K first and then twice from 263 K to 673 K, under nitrogen atmosphere.

In the case of the DMA measurements in tensile mode, the complex modulus of elasticity E^* is obtained, which is given by:

$$E^*(T, f) = E'(T, f) + iE''(T, f) \quad (3.20)$$

where E' is the real part (storage modulus) and E'' the imaginary part (loss modulus).

From the thermodynamic point of view the complex dielectric function is a generalized compliance.⁶³ In order to compare the dielectric with the mechanical data the mechanical compliance should be therefore considered instead of the modulus. The compliance is defined as the inverse modulus of elasticity. The so called strain compliance D^* is given by:

$$D^*(T, f) = D'(T, f) - iD''(T, f) \quad (3.21)$$

where D' is the real part and D'' the imaginary part (strain compliance).

3.6 FTIR Spectroscopy

A Vertex70 FTIR spectrometer (Bruker Optics) equipped with a FTIR600 Linkam cell (Linkam Scientific Instruments Ltd., Chilworth, UK) was used to obtain FTIR spectra. The samples were measured in transmission mode at room temperature and in a wavenumber range of 450 to 4500 cm^{-1} , accumulating 32 scans with a resolution of 4 cm^{-1} .

3.7 Scanning Electron Microscopy

Scanning electron microscopy (SEM) was performed with a Zeiss EVO MA10 device. The samples were broken with prior cooling using liquid nitrogen, to analyze the cross sections. Afterwards, the samples were sputtered with a thin gold layer.

3.8 Thermogravimetric Analysis

Thermogravimetric analysis (TGA) was conducted to monitor the drying/annealing process of the cast films and to estimate the PhE-POSS content within the PIM-1 and Matrimid composites. A TG/DTA 220 instrument (Seiko, THASS Germany) was used in a temperature range from 312 to 1168 K with a heating rate of 10 K/min and with synthetic air as flow gas.

4 Materials and Sample Preparation

4.1 Materials

4.1.1 Gases

Nitrogen N₂, oxygen O₂, methane CH₄ and carbon dioxide CO₂ were purchased from Air Liquide and Linde with a purity of 99.9995 %.

4.1.2 Polymer Matrix

Matrimid

Matrimid is an amorphous polymer with a density of 1.24 g/cm³ and a glass transition temperature T_g of about 321 °C (see Fig. 4.2). Matrimid 5218 (Fig. 4.1), a BTDA-DAPI polyimide consisting of 3,3'-4,4'-benzophenone tetra-carboxylic dianhydride and diaminophenylindane was acquired from Huntsman International LLC. This polyimide is marketed as full-imidized polymer during manufacturing. The material was used without further purification.

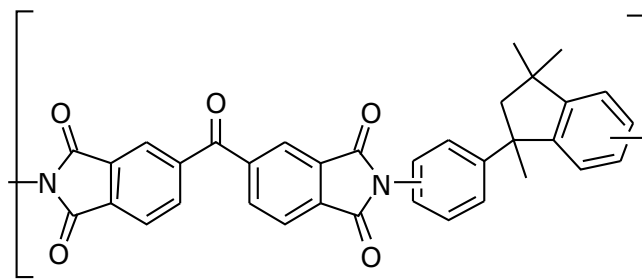


Figure 4.1 – Structure of Matrimid 5218.

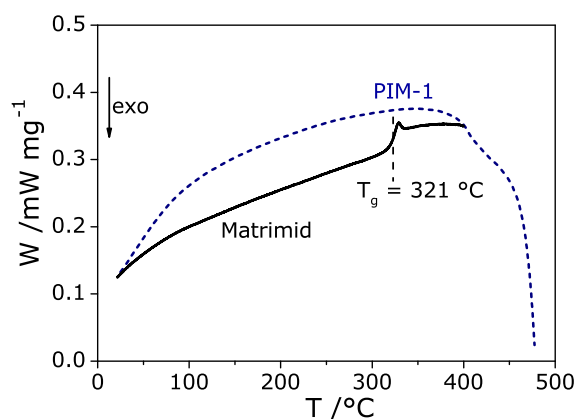


Figure 4.2 – DSC measurements for pure Matrimid and pure PIM-1 for the second heating (heating rate 10 K/min).

PIM-1

PIM-1 (Fig. 4.3) was synthesized by Wayne J. Harrison (The University of Manchester) according to ref.¹¹⁷ (see appendix A.1). The density of PIM-1 is 1.15 g/cm³. For PIM-1 no glass transition temperature can be observed before decomposition (see Fig. 4.2).

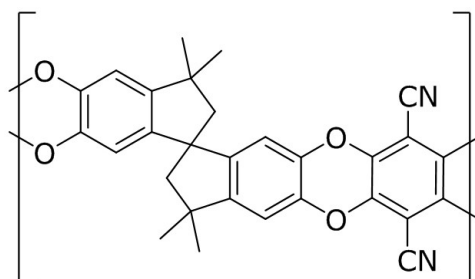


Figure 4.3 – Structure of PIM-1.

4.1.3 Nanofiller: Phenethyl-POSS

Phenethyl-POSS (PhE-POSS) was used as nanofiller due to good solubility/ miscibility and expected interactions of the phenyl substituents and the π -system of the used polymers (POSS is a trademark of Hybrid Plastics Inc. (Hattiesburg, MS). See also www.hybridplastics.com). PhE-POSS was purchased from Hybrid Plastics, Inc. A detailed characterization of PhE-POSS is given in reference.^{118,119} The material

was used without further purification. MALDI-TOF was used to characterize PhE-POSS. As discussed in ref.,¹¹⁹ the spectra showed a mixture of octa- (T8, $n = 8$), deca- (T10, $n = 10$) PhE-POSS and small amounts of larger cage sizes as well. It is generally known from the synthesis of POSS that the main fraction of the product consists of octa-cages.^{120,121}

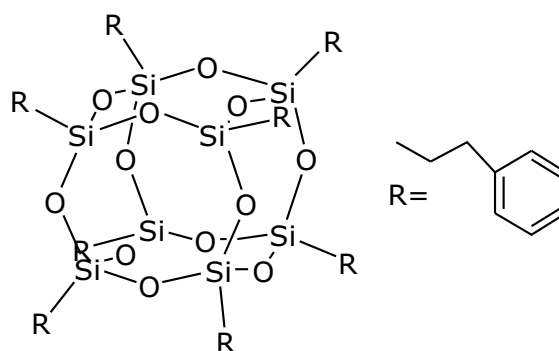


Figure 4.4 – Structure of PhenethylPOSS.

4.2 Sample Preparation

The polymer films were prepared by solution casting. The used temperature treatments are compromises of temperatures which are high enough to remove the residual solvent but preferably low to reduce previous physical aging effects.

4.2.1 Matrimid and Matrimid/PhE-POSS Composites

In the first step, 0.7 g of Matrimid and different amounts of PhE-POSS were dissolved in 12 ml dichloromethane (DCM) and mixed for 4 h. Afterwards, the solution was casted on a Teflon-plate in a closed chamber to ensure a slow first evaporation of DCM. In the next step, the samples were dried in vacuum at 100 °C for 6 days.

The obtained Matrimid/PhenethylPOSS films were transparent and yellowish. With increasing PhE-POSS concentration, the films became less transparent. For high PhE-POSS concentrations, small areas of high cloudiness were formed (see Figure 4.5).

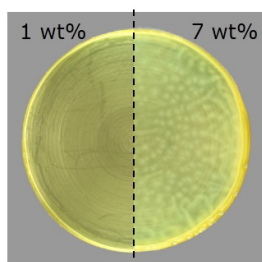


Figure 4.5 – Images of cast Matrimid/PhE-POSS films with 1 wt% and with 7 wt% PhE-POSS.

4.2.2 PIM-1 and PIM-1/PhE-POSS Composites

Here, 1 g of PIM-1 and different amounts of PhE-POSS were dissolved in 12 ml chloroform and stirred for 4 hours. Afterwards, the solution was filtered (5 μm PTFE-filter) and then cast on a Teflon plate. In order to ensure slow evaporation of the solvent, the films were dried in chloroform atmosphere at room temperature for 2 days. Based on thermogravimetric analysis (TGA), the samples were then heated up to 348 K (75 °C) for 3 days, all giving transparent, yellowish films (see Figure 4.6). For more details to the finding of the temperature treatment see appendix A.1. With increasing PhE-POSS content the films tend to become more brittle. As for pure PIM-1, no glass transition could be measured before the decomposition of the nanocomposites.

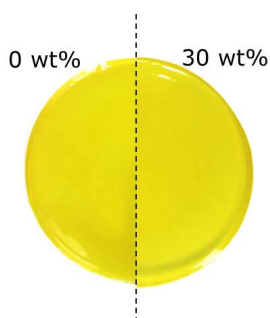


Figure 4.6 – Image of cast PIM-1 film and with 30 wt% of PhE-POSS.

5 Matrimid and Matrimid/POSS Nanocomposites*

Abstract

The dielectric properties of Matrimid and Matrimid/ PhE-POSS nanocomposites were investigated using BDS in combination with standard techniques. Matrimid shows one relaxation process assigned as β^* -relaxation and a conductivity contribution. The relaxation process has a high activation energy of 99 kJ/mol. Thus, this process is assumed to be of cooperative nature due to a $\pi - \pi$ -stacking of the phenyl rings of Matrimid. The influence of the thermal history on Matrimid was analysed with BDS as well, where an annealing effect is found. The Matrimid/PhenethylPOSS nanocomposites show a miscibility on a molecular level up to a concentration of about 4 wt% PhenethylPOSS. For higher concentrations, a phase separated structure was indicated. The conductivity of both systems is explained by $\pi - \pi$ -stacking of the phenyl rings, which enhances charge transport.

Furthermore, gas transport properties were investigated for Matrimid and Matrimid/ PhenethylPOSS composites for N₂, O₂, CH₄ and CO₂ at 35 °C. The permeability of Matrimid was enhanced by 1 wt% embedded in the polymer matrix for all analyzed gases. In addition, the plasticization effect of Matrimid was reduced for high POSS contents in the composites. Permeability, selectivity and diffusion coefficients evidenced a phase separated structure for the Matrimid/PhE-POSS composites above 8 wt%.

*Similar content (section 5.1 and 5.2) was published in Konnertz, N.; Böhning, M.; Schönhals, A., *Polymer*, 2016, 90, 89 - 101.

5.1 Introduction

Sánchez-Soto et al. studied the morphology and properties of polycarbonate PhenethylPOSS nanocomposites which were prepared by melt blending.¹²² A good miscibility up to a PhenethylPOSS concentration of 5 wt% was found. At higher concentrations, micron-sized aggregates of POSS are observed with scanning and transmission electron microscopy. Furthermore, wide angle X-ray diffraction revealed a crystalline structure comparable to pure PhenethylPOSS but with lower crystal sizes and less ordered structure within the POSS-rich domains compared to pure PhenethylPOSS.

Miscibility, specific interactions, and thermomechanical properties of a novolac resin PhenethylPOSS nanocomposite were studied by Wu et al.¹²³ Here, a good miscibility up to a concentration of 20 wt% was observed. The high miscibility was explained by hydrogen bonds between the hydroxyl groups of the phenolic resin and the POSS siloxane groups which was evidenced by FTIR. At higher POSS concentrations an aggregation of the nanofiller was also verified by polarized optical spectroscopy, differential scanning calorimetry, and wide angle X-ray diffraction.

Hao et al. investigated polystyrene/PhenethylPOSS¹¹⁸ and poly(bisphenol A carbonate) (PBAC)/PhenethylPOSS systems by broadband dielectric spectroscopy¹¹⁹ and gas transport measurements.¹¹⁵ For polystyrene a molecular miscibility up to 40 wt% of POSS was found. In contrast, PBAC/PhenethylPOSS showed a phase separation at a concentration of ca. 7 wt%. Due to $\pi - \pi$ stacking of the phenyl rings of POSS and polystyrene,¹²³ the miscibility for the polystyrene/POSS system is enhanced compared to polycarbonate.^{118,119,122}

Li et al. successfully incorporated octa amid acid POSS (up to 20 wt%) with subsequent embedding of Zn^{2+} in Matrimid by solution casting¹²⁴ to improve the gas transport properties.¹²⁵ A good miscibility of POSS and Matrimid due to intermolecular hydrogen bonds between the carboxylic groups of POSS and Matrimid was found.

5.2 Relaxation Behavior

Recently, Comer et al. investigated the dielectric and mechanical relaxation behavior of Matrimid in a temperature range from 123 K to 573 K (one run, steps of

$\Delta T = 10$ K).¹²⁶ The prepared solution-casted Matrimid film was dried after casting seven days at room temperature at ambient conditions, four days under vacuum at 373 K, at 473 K for one day and then in a nitrogen purge at 603 K for 30 min. Using mechanical spectroscopy (DMA), a γ -relaxation was observed at low temperatures ($f = 1$ Hz, $T \approx 153$ K) for their Matrimid sample. At higher temperatures than the γ -relaxation, a β -relaxation ($f = 1$ Hz, $T \approx 348$ K) and an α -relaxation was observed. The β -relaxation was claimed to be of "localized, relatively non-cooperative molecular origin",¹²⁶ while the α -relaxation was assigned to segmental fluctuation. The γ - and β -relaxation were also confirmed by Comer et al. using dielectric spectroscopy. The quantitative analysis of both processes yields activation energies which were further analyzed by the Starkweather approach.¹²⁷

This section focuses on the relaxation behavior of pure Matrimid and Matrimid/PhenethylPOSS composites. Here, in contrast to Comer et al.,¹²⁶ the dielectric measurements of Matrimid and the Matrimid/PhenethylPOSS composites were carried out with a specific sample conditioning to study the influence of the temperature treatment on the molecular mobility of Matrimid and the nanocomposites.

5.2.1 Characterization

The thermal glass transition temperatures (T_g) of the samples were determined by means of DSC. Sample specifications, thermal glass transition temperatures, densities (ρ), and film thicknesses of the samples are given in Table 1. The sample designations include the concentration of PhE-POSS within the composites. The results for the concentration dependence of the density and T_g of the samples are discussed in detail in paragraph 5.2.3.

Table 5.1 – Sample codes with the corresponding PhE-POSS concentrations, glass transition temperatures for the first and second heating, their densities, and the film thickness of MI and the MI/PhE-POSS composites.

Sample	wt%	T_g /K (1st heating)	T_g /K (2nd heating)	ρ /g cm ⁻³	Thickness / μ m
MI-00	0	575	594	1.24	90.5
MI-006	0.6	574	593	1.22	93.1
MI-01	1	573	590	1.25	94.2
MI-02	2	573	589	1.27	90.4
MI-03	3	567	587	1.28	107.0
MI-04	4	566	586	1.25	104.7
MI-07	7	557	582	1.26	103.1
MI-10	10	557	583	1.26	107.1
MI-15	15	558	583	1.25	110.5
MI-20	20	557	583	1.24	116.5
PhE-POSS	100	-	517 ¹¹⁹	1.22 ¹¹⁹	-

It was attempted to adjust the film thickness to around 100 μ m. Due to an increasing viscosity with increasing PhE-POSS concentration, the thickness of the composites films increases slightly with the POSS amount.

Thermogravimetric analysis (TGA) was applied to prove the PhE-POSS content within the Matrimid-PhE-POSS composites. Figure 5.1 gives example curves of the TGA measurements, and the inset provides a detailed view on the TGA curves at high temperatures for MI-00 and selected MI/PhE-POSS composites. The inset presents a detailed view on the TGA curves above 900 K.

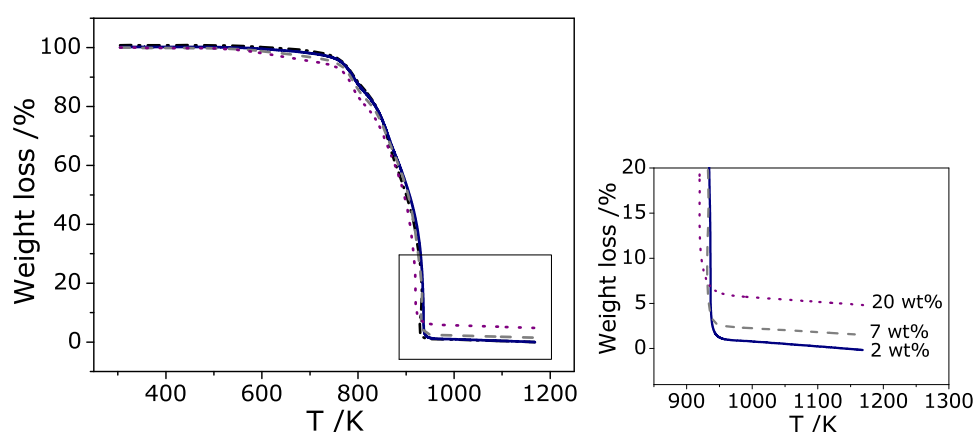


Figure 5.1 – TGA curves of MI-00 (dashed-dotted line), MI-02 (solid line), MI-07 (dashed line) and MI-20 (dotted line). The inset gives a detailed view of the TGA curves at high temperatures.

The polymer matrix and the POSS are completely oxidized during heating. It is assumed that only Si as SiO_2 remains in the residue as it can be seen from the plateaus of the TGA curves at high temperatures (Figure 5.1). This plateau value increases with increasing POSS content (see inset of Figure 5.1). For this reason it is concluded that the residual weight can be regarded as measure of the POSS concentration.

In Figure 5.2 the remaining weight percent is plotted versus the nominal PhE-POSS concentration used for the preparation.

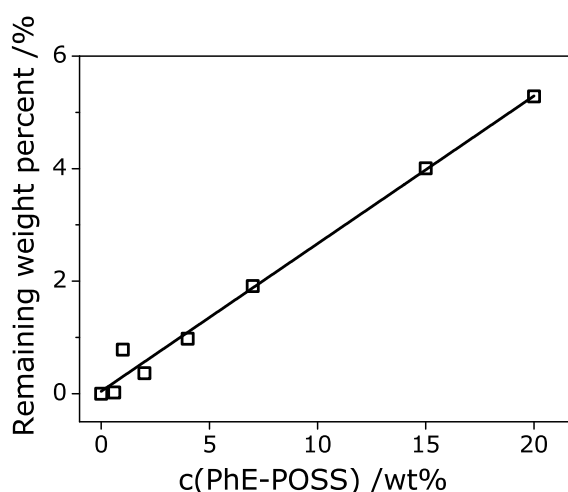


Figure 5.2 – Remaining weight percent vs. $c(\text{PhE-POSS})$. The solid line is a linear fit to the data.

The relation between residual weight and POSS concentration is linear, supporting this approach, to estimate the POSS content by TGA.

5.2.2 Relaxation Behavior of Pure Matrimid

5.2.2.1 Broadband Dielectric Spectroscopy

As discussed above, Comer et al. investigated the dielectric relaxation behavior of Matrimid in a temperature range from 123 K to 573 K with temperature steps of 10 K.¹²⁶ In that work the casted Matrimid film was dried seven days at ambient conditions, four days under vacuum at 373 K, at 473 K for one day, and finally in a nitrogen purge at 603 K for 30 min. Two relaxation processes were observed below T_g . A first relaxation mode was observed in the temperature range from 153 K to 263 K and was denoted γ -relaxation. A further process was found at higher temperatures (370 K – 500 K) than the γ -process and is assigned to a β -relaxation.

Figure 5.3 shows our measurement of the dielectric loss of pure Matrimid (MI-00) in dependence on frequency and temperature in a 3D representation for the second heating cycle.

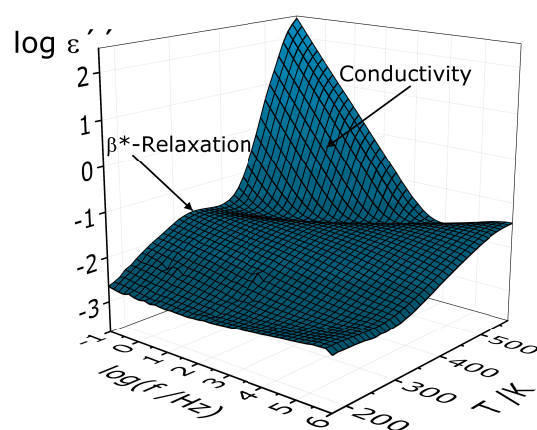


Figure 5.3 – Dielectric loss $\log \varepsilon''$ vs. frequency and temperature for pure Matrimid (MI-00) in a 3D presentation for the second heating cycle (compare Figure 3.6).

In contrast to the work of Comer et al., only one relaxation process is observed, indicated as a peak in the dielectric loss ε'' . The γ -relaxation described by Comer et al. at low temperatures is not observed here. The reason is not known and requires

further investigations. One reason might be the different sample preparation and annealing procedure.

The observed relaxation peak is rather broad. With increasing temperature, the process shifts to higher frequencies as expected. The relaxation mode is located in a temperature range similar to the β -process of Comer et al.¹²⁶ Here, the process is called β^* -relaxation for reasons discussed below. In the temperature range above the β^* -process, a strong increase in ϵ'' is observed, which increases with decreasing frequency. This effect is due to conductivity phenomena related to drift motions of mobile charge carriers. Surprisingly, conductivity is observed at temperatures well below the glass transition temperature of Matrimid. This effect will be discussed in detail in the section 5.2.2.2 below.

The HN-function (eq. 3.12) was fitted to the data leading to the relaxation rate f_{max} and the dielectric strength $\Delta\epsilon$. Examples for the fit are given in Figure 5.4.

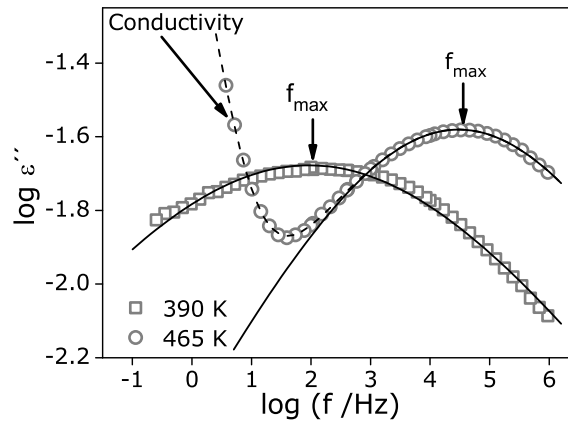


Figure 5.4 – Dielectric loss vs. frequency for MI-00 at 390 K and 465 K. The lines are fits of the HN function to the data. The dashed lines represent the contribution of the respective relaxation process.

The temperature dependence relaxation rates f_{max} for the β^* -relaxation for all heating and cooling runs are plotted vs. inverse temperature in Figure 5.5 (relaxation map). For comparison, the data of Comer et al. are included too. At first glance, the temperature dependence of the relaxation rates seems to follow the Arrhenius equation (see eq. 2.2).

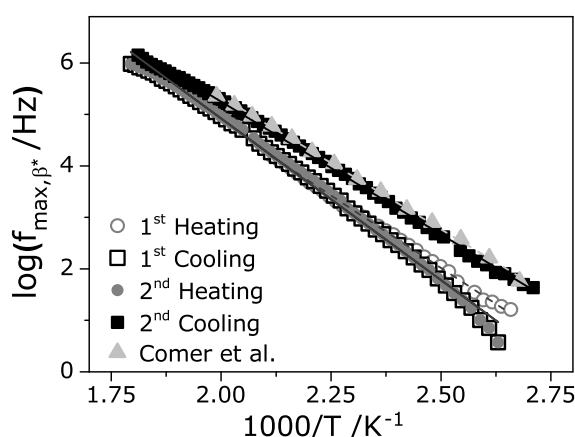


Figure 5.5 – Relaxation rate f_{max,β^*} vs. inverse temperature for pure Matrimid (MI-00) including the complete temperature treatment (1st heating, 1st cooling, 2nd heating, 2nd cooling), whereas first cooling and second heating are superposed. Furthermore, the results for pure Matrimid from Comer et al. are included.¹²⁶ The lines are fits of the Arrhenius equation to the corresponding data.

Obviously, the apparent activation energy changes with the thermal treatment of the sample. The first change in the apparent activation energy is observed between the first heating and the first cooling cycle, where for the first cooling run a higher apparent activation energy is found than for the heating cycle. This might be due to the evaporation of traces of residual solvent and/or the formation of a densified structure during the temperature treatment. The apparent activations energies for the first cooling and the second heating run are more or less identical. This leads to the conclusion that the cooling process does not further affect the structure of Matrimid. The thermal treatment during the second heating up to 573 K results in a decrease of E_A of the β^* -relaxation. This indicates a loosening of the structure or a change in the packing of the polymer segments, leading to an enhanced mobility. This assumption is in agreement with the results for the activation energy of Comer et al.¹²⁶ They heated the Matrimid film before the BDS measurements up to 603 K leading to a similar apparent activation energy of the β^* -relaxation.

The activation energies estimated for the β^* -relaxation are relatively high and not characteristic for a solely β -process. The activation energy of true β -processes for polymers is expected to be in the range of 40 kJ/mol to 60 kJ/mol. Here, the activation energies are found in the range of 100 kJ/mol (see Figure 5.6). Moreover, the β^* -relaxation is found at relatively high temperatures close to the glass transition temperature. This is also untypical for a β -process.

A process with similar properties to the β^* -relaxation reported here was also observed for Poly(ethylene 2,6 naphthalene dicarboxylate) (PEN).^{128–130} The reported activation energies for the β^* -relaxation of PEN are in a range similar to the values found here for the β^* -relaxation observed for Matrimid. Hardy et al. assigned the β^* -relaxation of PEN to fluctuations of agglomerated naphthalene groups. Spies/Gehrke and Jones et al. evidenced such an agglomeration of naphthalene groups in solution¹³¹ as well as in solid state¹³² with optical spectroscopy. These arguments lead to the assumption that the β^* -relaxation observed for Matrimid might also be due to molecular fluctuations of agglomerated phenyl groups. Wide angle X-ray measurements evidence such aggregates with a molecular spacing of 3.2 Å and 5.3 Å (Appendix A.4).¹³³ Such molecular fluctuations require a certain cooperativity of the underlying molecular motions, which was also evidenced by the Starkweather analysis given in ref.¹²⁶ This analysis indicates a relatively high value of the activation entropy which is characteristic for cooperative processes as well.

The strong increase in the imaginary part ϵ'' at low frequencies is attributed to conductivity effects (see Figure 5.4). This indicates a high mobility of charge carriers within Matrimid even below the thermal glass transition temperature which is discussed in detail in paragraph 5.2.2.2.

A Matrimid film was prepared as described in 4.2 to verify that the structure of Matrimid is stable after heating the sample up to 573 K. Afterwards, the sample was measured using BDS as previously accomplished with an additional heating (up to 573 K) and cooling (down to 173 K) (sample code: MI-3Heat). Furthermore, a Matrimid film was prepared as described in section 4.2, then dried additionally at 473 K for one day in vacuum and afterwards, heated to 573 K in air for 30 minutes (sample code: MI-00-300) to compare the influence of the film preparation with the results of Comer et al. This film was measured with BDS using the temperature program as described in section 3.1. The activation energies of the β^* -relaxation for the different heating (H) and cooling (C) runs of MI-00, MI-00-300 and MI-3Heat as well as the $E_{A,\beta}$ of Comer et al. are shown in Figure 5.6.

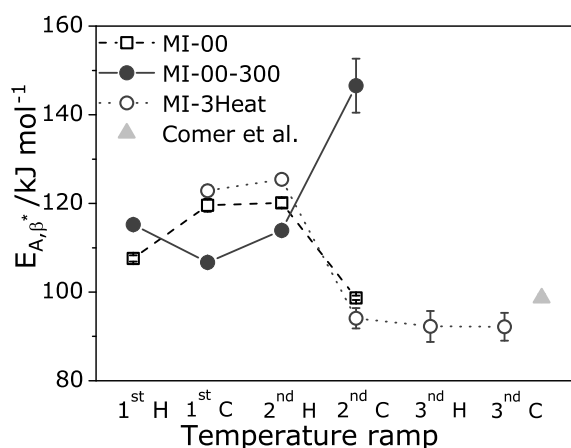


Figure 5.6 – Activation energy E_{A,β^*} for the different heating (H) and cooling runs (C) for MI-00, MI-00-300, and MI-3Heat. Furthermore, the value of Comer et al. is included.¹²⁶ The lines are guide for the eyes.

MI-00-300 shows an opposite behavior of E_{A,β^*} compared to the other Matrimid films. The activation energy of the β^* -relaxation for MI-00-300 decreases after heating up to 473 K, increases afterwards and finally strongly increases after heating the sample up to 573 K.

The observed changes of the activation energy with the heat treatment cannot be attributed to chemical alterations within the samples, especially because it is considered as fully imidized. The material is still completely soluble even after the strongest thermal impact. Also, the FTIR spectra for the untreated and the treated samples are identical (see Figure 5.7). Therefore, it is concluded that the observed changes are due to changes of the packing density of the polymer segments.

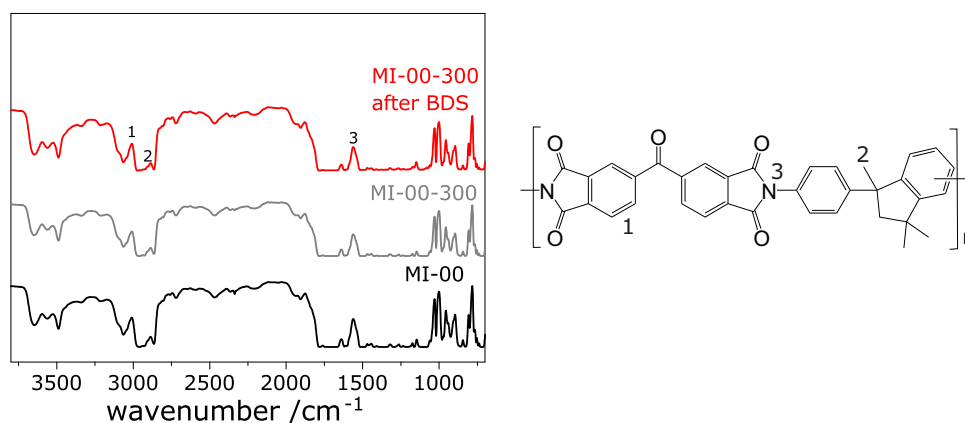


Figure 5.7 – FTIR spectra of MI-00, MI-00-300 and the sample MI-00-300 after BDS measurement.

5.2.2.2 Conductivity

As discussed above, Matrimid as well as the corresponding composites show a strong conductivity contribution at temperatures well below their thermal glass transition temperatures. This is an unusual behavior because for most conventional polymers conductivity effects are observed above T_g because charge transport is related to segmental dynamics in these systems.⁶³ Therefore, it is concluded that for the Matrimid systems charge transport is due to a different mechanism. This conductivity effect is quantified by the complex conductivity given by equation 3.5.

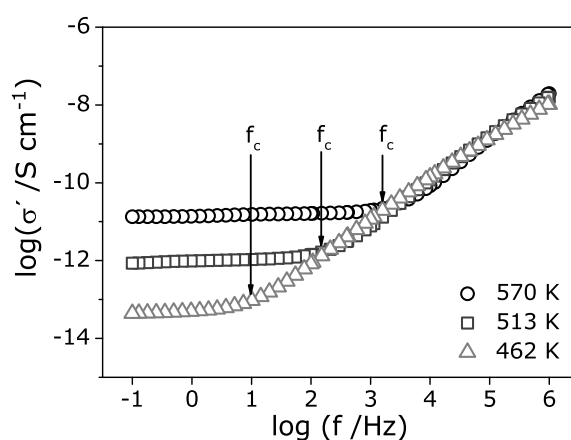


Figure 5.8 – Real part of the complex conductivity σ' versus frequency for the second cooling run for pure Matrimid MI-00 at different temperatures ($T = 570$ K; $T = 513$ K; $T = 46$ K).

The frequency dependence of the real part of the complex conductivity spectra shows the typical behavior, which is expected for semi-conducting polymeric materials (see section 3.1.3). The data is approximated by the Jonscher power law (eq. 3.15) and σ_{DC} is obtained by fitting the Jonscher equation to the data.

Figure 5.9 depicts the DC conductivity σ_{DC} as a function of inverse temperature for pure Matrimid. The temperature dependence of the DC conductivity can be described by the Arrhenius equation (eq. 2.2). For conventional amorphous polymers, the conductivity is related to segmental dynamics and its temperature follows the Vogel-Fulcher-Tammann equation (eq. 2.3). For Matrimid, the temperature dependence is Arrhenius-like ($E_{A,\sigma_{DC}} = 115$ kJ/mol) and is observed at temperatures below the glass transition temperature. Therefore, it is concluded that for Matrimid the conductivity is not directly related to segmental dynamics. As discussed above, agglomerates

formed by stacked phenyl groups by $\pi - \pi$ -interaction were found with wide angle X-ray scattering measurements. Due to the overlapping π -systems, charge transport in Matrimid is enhanced.

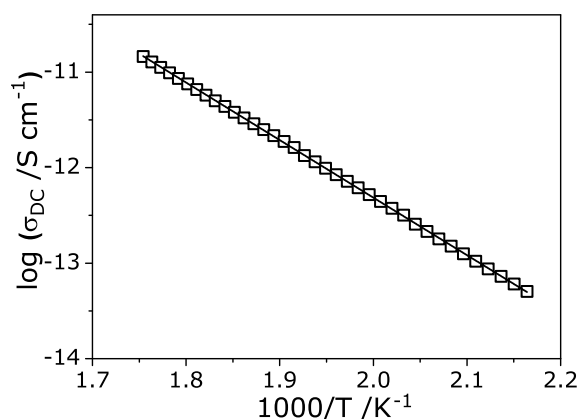


Figure 5.9 – Direct current conductivity (σ_{DC}) for the second cooling run vs. inverse temperature for MI-00. The line is a fit of the Arrhenius equation to the data.

5.2.2.3 Dynamic Mechanical Analysis

The dynamic-mechanical properties of Matrimid were determined by DMA. The loss modulus E'' and the strain compliance D'' vs. temperature are compared for pure Matrimid for the third heating at 1 Hz in Figure 5.10. The loss modulus shows the β^* -relaxation at lower and an α -relaxation (dynamic glass transition) at higher temperatures. The dynamic glass transition is related to segmental fluctuations. A similar behavior is reported by Comer et al.¹²⁶ Compared to the loss modulus, the imaginary part of the compliance shows also a β^* -relaxation at lower temperatures. For higher temperatures in the region, where the α -relaxation is observed in the modulus, the onset of flow is evidenced in the loss part of the compliance by a strong increase of D'' with increasing temperature.

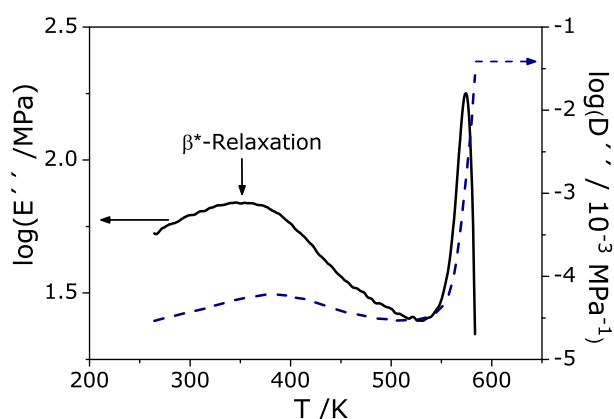


Figure 5.10 – Loss modulus E'' (solid line) and loss part of the strain compliance D'' (dashed line) for Matrimid (MI-00) vs. temperature for the third heating run at 1 Hz (DMA).

Figure 5.11 compares the temperature dependence of the dielectric loss ϵ'' and loss part of the mechanical compliance D'' at the same frequency.

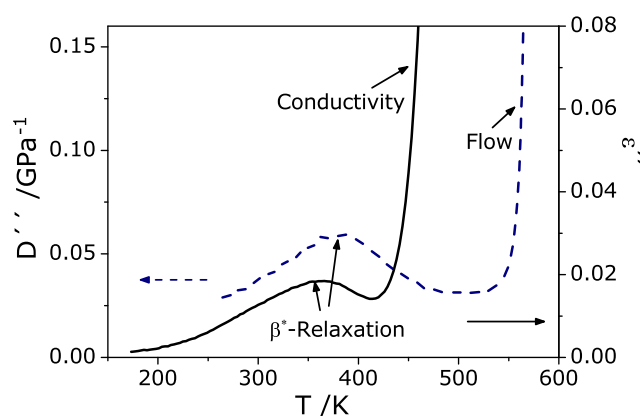


Figure 5.11 – Loss part of the strain compliance D'' (DMA) (dashed line) and dielectric loss ϵ'' (solid line) vs. temperature of Matrimid (MI-00) for the second cooling run at a frequency of 1 Hz.

In principle, a similar behavior is observed for dielectric and mechanical properties. Compared to the dielectric data the loss peak for the compliance is shifted a bit to higher temperatures. This effect is commonly observed for polymers.¹³⁴ Both methods are sensitive to different molecular probes. While dielectric relaxation is related to dipole fluctuations, the mechanical compliance senses the fluctuations of the shear angle. This means both methods monitor the same process but through a different window.

Figure 5.12 gives the loss part of the elastic modulus versus temperature for two different frequencies.

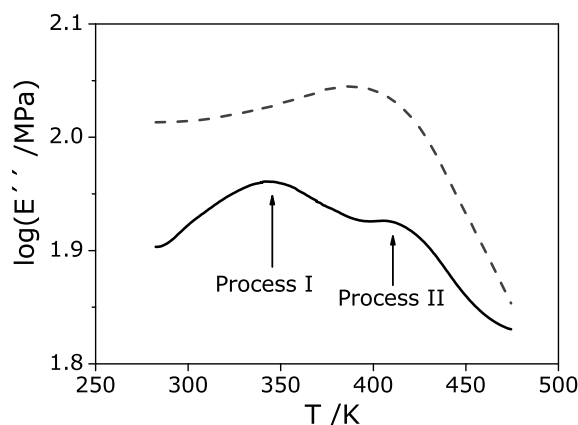


Figure 5.12 – Loss modulus E'' for Matrimid (MI-00) vs. temperature for the third heating run at 0.3 Hz (solid line) and 10 Hz (dashed line).

While for high frequencies 10 Hz and 1 Hz (see Figure 5.10) only one broad peak is observed, this peak splits into two processes for lower frequencies. Also a closer inspection of the dielectric loss gives evidences that the β^* -relaxation consist of two processes (see Figure 5.13) which merge together for higher frequencies or temperatures.

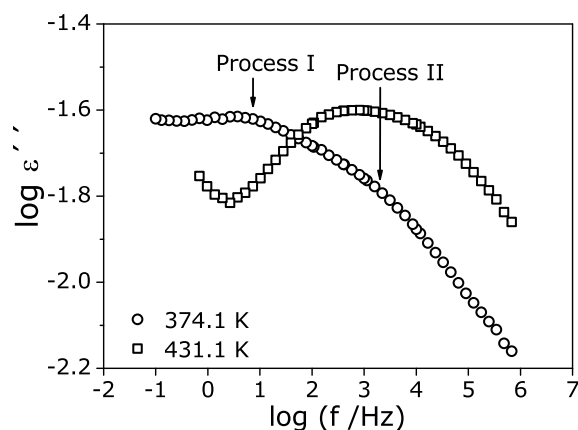


Figure 5.13 – Dielectric loss vs. frequency for MI-00 at 431.1 K and 374.1 K for the first cooling run.

Unfortunately, due to the close overlapping the processes cannot be separated unambiguously. Bearing in mind that WAXS pattern shows two different spacings for stacks and the assignment of the β^* -relaxation to molecular fluctuations to these

aggregates, it is concluded that the observed two modes of the β^* -relaxation are due to these different aggregates.

5.2.3 Properties of Matrimid/POSS Nanocomposites

Before the dielectric properties are discussed in detail, DSC and density measurements are considered.

5.2.3.1 Differential Scanning Calorimetry

In Figure 5.14, DSC measurements of pure Matrimid MI-00 for the first and second heating run are shown. The peak at low temperatures of the first heating run is attributed to water. When the sample is exposed to normal atmosphere after the second heating run, the DSC measurements show this peak for the first heating run again.

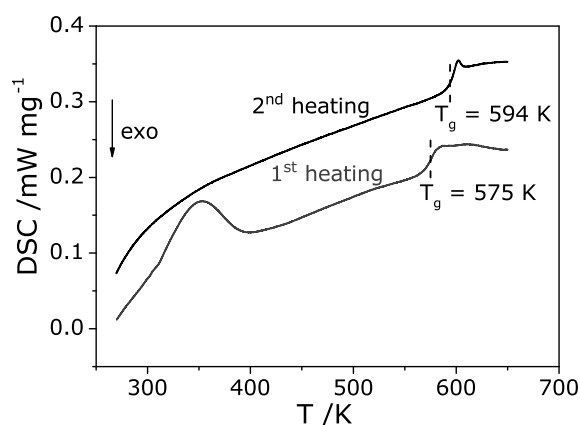


Figure 5.14 – DSC measurements for pure Matrimid MI-00 for the 1st and the 2nd heating run.

The glass transition temperatures T_g were taken from the step in the heat flow (Figure 5.14). T_g of pure Matrimid and the corresponding nanocomposites with POSS for the first and second heating run are presented in Figure 5.15.

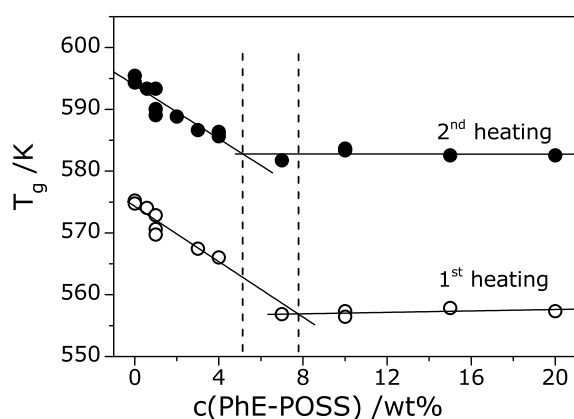


Figure 5.15 – Dependence of the thermal glass transition temperature T_g on the concentration of PhE-POSS for the 1st and the 2nd heating run for pure Matrimid MI-00 and the MI/PhE-POSS composites. The DSC measurements were carried out up to 670 K with a heating rate of 10 K/min. The lines are guides for the eyes.

T_g is shifted to higher temperatures for the second heating compared to the first run. For the first heating run, T_g decreases with increasing concentration of PhE-POSS up to about 8 wt%. For higher PhE-POSS concentrations, T_g becomes independent of the amount of POSS. A comparable dependence of the glass transition temperature on the concentration of PhE-POSS was observed for polycarbonate/POSS nanocomposites.¹¹⁹ In that case, the decrease in T_g with increasing POSS concentration was explained by a plasticization effect where the plateau value of T_g for higher concentrations of POSS evidenced a (nano)phase separation. Compared to polycarbonate, Matrimid is a stiff polymer with a high amount of free volume. In the case of low concentrations of POSS, PhE-POSS can be dissolved on a molecular level, probably in the free volume sites where the phenyl rings of POSS can interact with that of Matrimid. This assumption is further supported by the results for the densities which are discussed below. By that mechanism the dense packed structure of Matrimid is partially disturbed and the molecular mobility of the polymer segments (or parts of it) is enhanced which leads to a decrease of T_g . For ca. 8 wt% of PhE-POSS, all available free volume sites are filled up and with increasing POSS concentration PhE-POSS cannot be dissolved in the Matrimid structure and (nano)phase separation takes place with further increase of the concentration of POSS. This also means when the saturation of PhE-POSS in the Matrimid matrix is reached the composition of the mixed phase remains constant. Thus, the molecular interaction between Matrimid and POSS does not change further, leading to a

constant T_g independent of the concentration of POSS. This is in good agreement with a prediction of T_g for partially miscible systems by Brostow et al.¹³⁵ Like for pure Matrimid, the thermal glass transition is shifted to higher temperatures for the second heating. The observed increase of T_g is caused by structural changes and a densification of the Matrimid matrix due to a partial collapse of the free volume sites. Compared to the first heating run, the transition from the decrease of T_g to the plateau value is shifted from ca. 8 wt% of PhE-POSS to 4 wt%. This is in agreement with the picture developed above that PhE-POSS is solved in the free volume sites. Due to the thermal treatment, the free volume sites are partially collapsed and the miscibility limit is shifted to lower concentrations of PhE-POSS. Moreover, this is also in agreement with the dielectric experiments discussed below where the second heating run is considered as well and nanophase separation is observed at around 4 wt% of PhE-POSS.

5.2.3.2 Density

The densities of the composites are plotted versus POSS concentration in Figure 5.16.

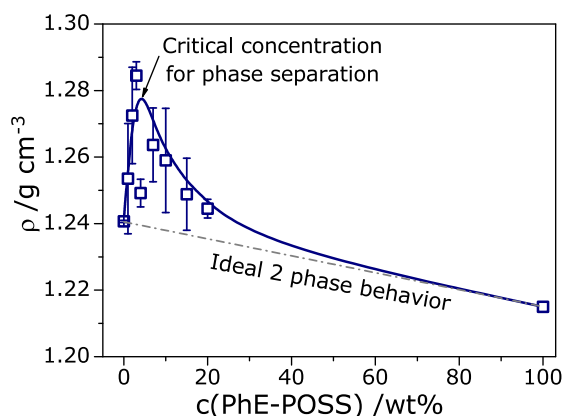


Figure 5.16 – Density of the MI/PhE-POSS composites vs. the PhE-POSS concentration. The solid line is a guide for the eyes. The dotted-dashed line indicates the behavior of an ideal two component system.

Surprisingly, for low POSS concentrations the density of the composites is higher than the densities of both compounds. It increases with the POSS concentration for low $c(\text{PhE-POSS})$. After the maximum between ca. 5 wt% and ca. 8 wt%, ρ decreases

with further increase of the POSS concentration and approaches the behavior which is characteristic for an ideal two component system (Figure 5.16).

Hao et al. investigated the molecular mobility of Poly(bisphenol A carbonate) (PBAC)/ PhE-POSS nanocomposites by BDS.¹¹⁹ They observed an opposite dependence of the density on the POSS concentration. In that case, the density decreases with increasing concentration of POSS in the miscible state. This was explained by the assumption that the adding of POSS molecules leads to an increase of the free volume and therefore to a decrease of the density. Compared to PBAC, Matrimid has a larger free volume.¹³⁶ In the case of low concentrations PhE-POSS is dissolved due to this free volume in the Matrimid matrix leading to an increase of the density. With increasing concentration, molecules saturate the free volume of the Matrimid matrix and an aggregation of PhE-POSS molecules occurs, leading to a (nano)phase separated structure. Thus, with further increasing POSS concentration an ideal two phase behavior can be observed for the density.

5.2.3.3 Broadband Dielectric Spectroscopy

Due to the strong effect of the thermal treatment on the properties of Matrimid discussed before the dielectric properties of the composites are discussed for the second cooling run in the following part. In Figure 5.17 the dielectric loss for the samples MI-00, MI-02, MI-15, and PhE-POSS is given as a function of the temperature at a frequency of 1 kHz as an example of the dielectric spectra for the composites.

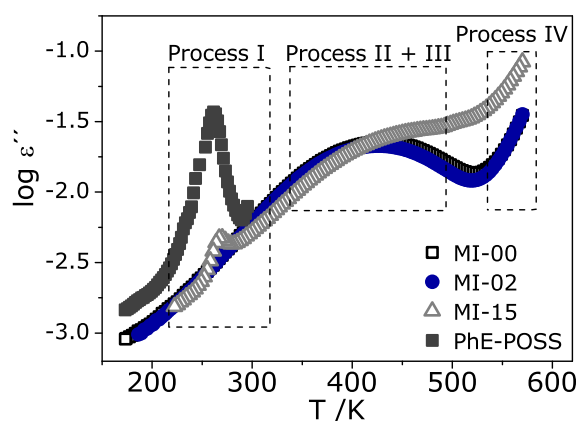


Figure 5.17 – Dielectric loss vs. temperature for the second cooling for pure Matrimid MI-00, for MI/PhEPOSS with 2 wt% MI-02, 15 wt% PhEPOSS MI-15, and pure PhE-POSS at a frequency of 1 kHz.

The peak in the dielectric loss ϵ'' at around 250 K for PhE-POSS indicates the dynamic glass transition or α -relaxation of POSS (process I). For a more detailed discussion see also ref.¹¹⁹ As discussed in section 5.2.2, a β^* -relaxation (process II) and a conductivity phenomenon (process IV) is observed for Matrimid. For MI-02, one broad peak which is similar to Matrimid is present. This behavior indicates that PhE-POSS is miscible in Matrimid on a molecular level. The dielectric loss of MI-15 has, besides the one broad peak at high temperatures which is related to Matrimid, one additional peak at temperatures which is close to the α -relaxation of pure PhE-POSS. Obviously, the latter process belongs to bulk-like PhE-POSS in a (nano)phase separated state. The conductivity contribution is observed for all samples while its strength increases with increasing PhE-POSS concentration.

The dielectric loss $\log \epsilon''$ is plotted vs. frequency $\log f$ for MI-00, MI-02 and MI-15 at a fixed temperature of 423 K in Figure 5.18 to analyze the broad peak at high temperatures (process II and III, Figure 5.17).

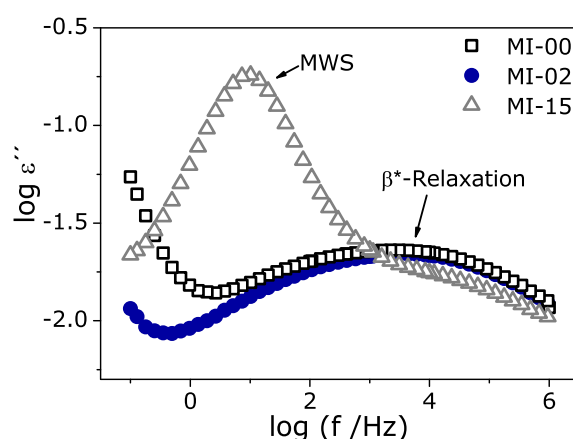


Figure 5.18 – Dielectric loss for the second cooling vs. frequency at 423 K for Matrimid, MI-02, and MI-15.

For MI-00 and MI-02 only one broad peak is observed which indicates miscibility on a molecular level. In case of MI-15, an additional relatively sharp peak is visible which is related to interfacial polarization effects (Maxwell-Wagner-Sillars polarization, MWS), supporting the assumption of a phase separation for high PhE-POSS concentrations. The following parts discuss the different relaxation processes belonging to Matrimid and PhE-POSS, respectively.

Relaxation Process Belonging to Matrimid: β^* -Relaxation

In this part, the influence of the PhE-POSS concentration on the β^* -relaxation is discussed. The dielectric spectra of the composites are analyzed by fitting the Havriliak-Negami function (eq. 3.12) to the data. The relaxation rates of the β^* -relaxation f_{max,β^*} are shown exemplary for MI-00, MI-02, and MI-07 plotted versus inverse temperature (Figure 5.19).

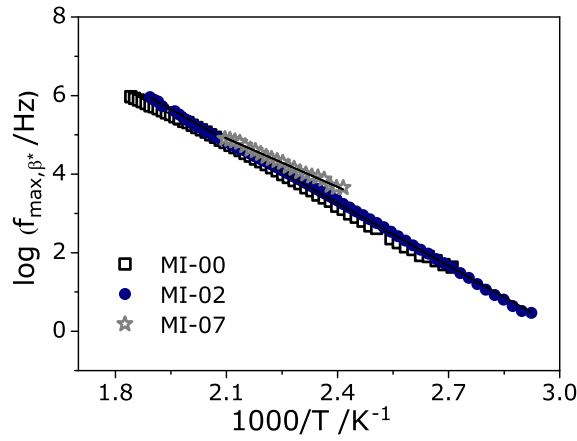


Figure 5.19 – Relaxation rate f_{max,β^*} for the second cooling vs. inverse temperature for Matrimid, MI-02, and MI-07. The lines are fits of the Arrhenius equation to the corresponding data.

The temperature dependence of the relaxation rates is Arrhenius-like (eq. 2.2). The activation energies E_{A,β^*} are extracted and discussed for PhE-POSS concentrations up to 7 wt% (Table 5.2).

Table 5.2 – Activation energy E_{A,β^*} determined by Arrhenius of different MI/PhE-POSS composites.

Sample	E_{A,β^*} /kJ mol ⁻¹
MI-00	99.2
MI-006	102.5
MI-01	118.7
MI-02	101.5
MI-03	101.9
MI-04	96.1
MI-07	79.0

E_{A,β^*} seems to be almost independent of the POSS content up to a PhE-POSS concentration of 4 wt%. The Matrimid matrix is only slightly influenced by the PhE-POSS molecules, which are incorporated in or close to the free volume sites, and by the proposed aggregates. Since the β^* -relaxation is assigned to the aggregates, E_{A,β^*} is almost independent of $c(\text{PhE-POSS})$. With further increasing PhE-POSS concentration, E_{A,β^*} seems to decrease slightly. For POSS concentrations higher than 7 wt%, the β^* -relaxation overlaps with the MWS polarization peak (see below). For those nanocomposites, the analysis of the β^* -relaxation cannot be done unambiguously.

Relaxation of Bulk-Like PhE-POSS

For PhE-POSS concentrations higher than 4 wt%, an additional peak in the imaginary part of ϵ'' (about $T = 270$ K) close to the α -relaxation of PhE-POSS is observed (Figure 5.17 and Figure 5.20). Its dielectric strength increases with increasing POSS concentration.

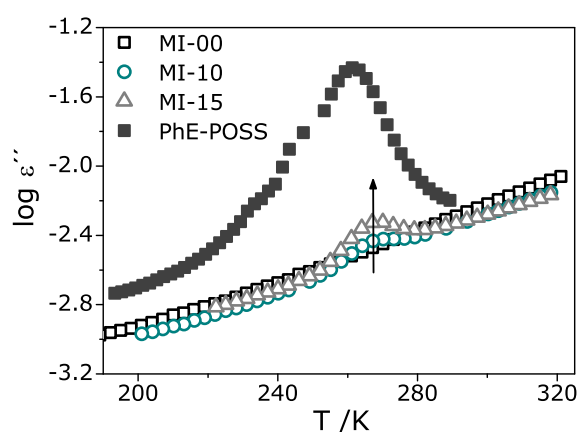


Figure 5.20 – Dielectric loss for the second cooling vs. temperature for pure PhE-POSS, MI-00, MI-10, and MI-15 at a frequency of 1 kHz.

The peak is directly related to the dynamic glass transition of bulk-like PhE-POSS which indicates a (nano)phase separation of PhE-POSS and Matrimid. This is in agreement with the results described above. The increase of the dielectric strength of this peak with increasing PhE-POSS concentration directly evidences the α -relaxation of PhE-POSS-rich domains which grow and/or increase in numbers with increasing POSS content. Compared to the α -relaxation of bulk POSS, the observed peak for the composites shifts slightly to higher temperatures. This shift can be due to two different origins. Firstly, the deeply frozen Matrimid matrix can be considered as a confinement to the POSS-rich domains which may constrain the mobility in these domains and thus increase its glass transition temperature. Secondly, if Matrimid is dispersed in the POSS-rich domains to a marginal extent, this can also lead to an increase of its glass transition temperature. Unfortunately, on the basis of the given experimental data, one cannot discriminate between both possibilities.

Dielectric Process due to the Phase Separated Structure: Maxwell-Wagner-Sillars Polarization

As discussed above, in addition to the broad peak of the β^* -relaxation an additional process can be observed in the same temperature range for higher POSS concentrations (see Figure 5.16). Its intensity increases with increasing PhE-POSS concentration. In phase separated morphologies, charges carriers can be separated on a mesoscopic length scale at the phase boundaries, leading to an interfacial polarization (MWS⁶³). The proposed structure of the POSS/Matrimid composites consists

of PhE-POSS domains and a Matrimid matrix (Figure 5.21). The T_g of PhE-POSS is low compared to T_g of Matrimid (Table 5.1). In the temperature range of the β^* -relaxation of Matrimid, the POSS molecules are in the liquid state and thus the mobility of the charge carriers within the PhE-POSS rich domains is much higher than in the Matrimid matrix, but their drift motion movement is blocked at the interfaces to the Matrimid matrix. This leads to an interfacial polarization – the MWS polarization process. The high mobility of the charge carries in the POSS rich domains is the molecular reason that the MWS process is observed at temperatures which are below the glass transition temperature of Matrimid. A similar behavior was observed for PhE-POSS/PBAC composites.¹¹⁹ The HN-function (eq. 3.12) is also employed to analyze this MWS interfacial polarization process. The resulting characteristic rates $f_{max,MWS}$ are given versus inverse temperatures in Figure 5.21.

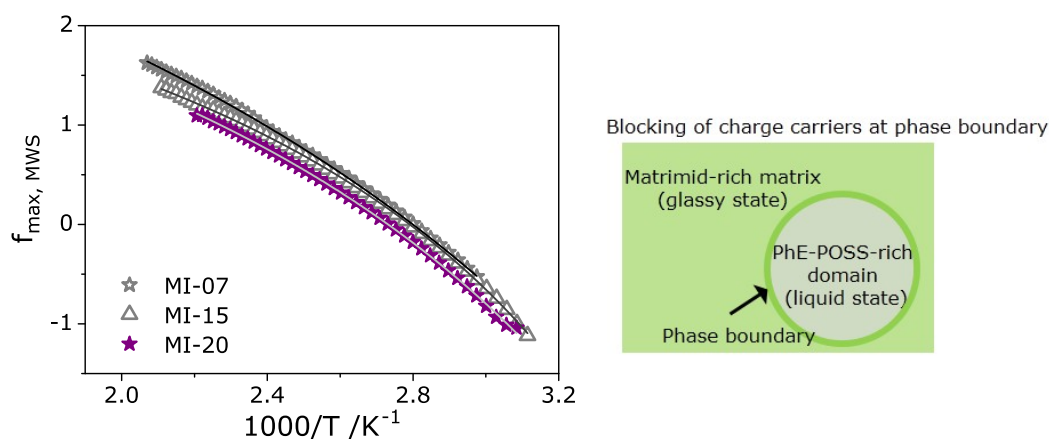


Figure 5.21 – Characteristic rate $f_{max,MWS}$ of the Maxwell-Wagner-Sillars polarization for the second cooling vs. inverse temperature for MI-07, MI-15, and MI-20. The lines are fits of the VFT-equation to the corresponding data. The scheme shows the proposed phase separated structure within the composites for high PhE-POSS concentrations.¹¹⁹

The temperature of the rate $f_{max,MWS}$ is curved when plotted versus $1/T$ and can be described by Vogel-Fulcher-Tammann (eq. 2.3). The estimated VFT parameters are listed in Table 5.3.

Table 5.3 – VFT parameters for the MWS polarization of different MI/PhE-POSS composites.

Sample	VFT parameters of MWS polarization		
	A /K	$\log f_{\infty}$ /Hz	T_0 /K
MI-07	762.3	4.1	170.3
MI-10	341.1	2.6	236.1
MI-15	418.8	3.0	218.9
MI-20	535.8	3.2	200.5

The temperature dependence of the relaxation rates of the β^* -relaxation of Matrimid follows the Arrhenius equation while the rate of the MWS polarization process are described by the VFT-relation. This is a further proof that the MWS process is due to the PhE-POSS rich domains. It is well accepted that for molecular or polymeric systems the temperature dependence of the conductivity is related to the α -relaxation in these materials. A characteristic feature of the α -relaxation is VFT-dependence of their relaxation rates. As discussed above, the MWS process is related to the mobility of the charge carriers and therefore to the conductivity. For that reason, the VFT-like temperature dependence of the rate of the MWS process in the PhE-POSS/Matrimid composites evidences that the MWS is due to the POSS rich domains. Moreover, the estimated Vogel temperature for this process is close to the Vogel temperature of the α -relaxation of bulk PhE-POSS (218 K).

With increasing POSS concentration, the rate of the MWS process decreases (see Figure 5.21). As discussed in ref.¹¹⁹ the rate of the MWS process is related to the size d of the POSS rich domain $f_{max,MWS} \sim d^{-1}$. This means that the decrease of $f_{max,MWS}$ with increasing POSS concentration is related to the growing of the size of the POSS rich domains. But compared to the PhE-POSS/PBAC, the increase of the size of the domains is much weaker. Therefore, it must be concluded that with increasing POSS amount the number of POSS rich domains increases stronger than their size. This behavior might be related to the stiffer structure of Matrimid compared to polycarbonate.

5.2.3.4 Scanning Electron Microscopy

These assumptions are further supported by SEM images of cross-sections of different MI/PhE-POSS composites (Figure 5.22).

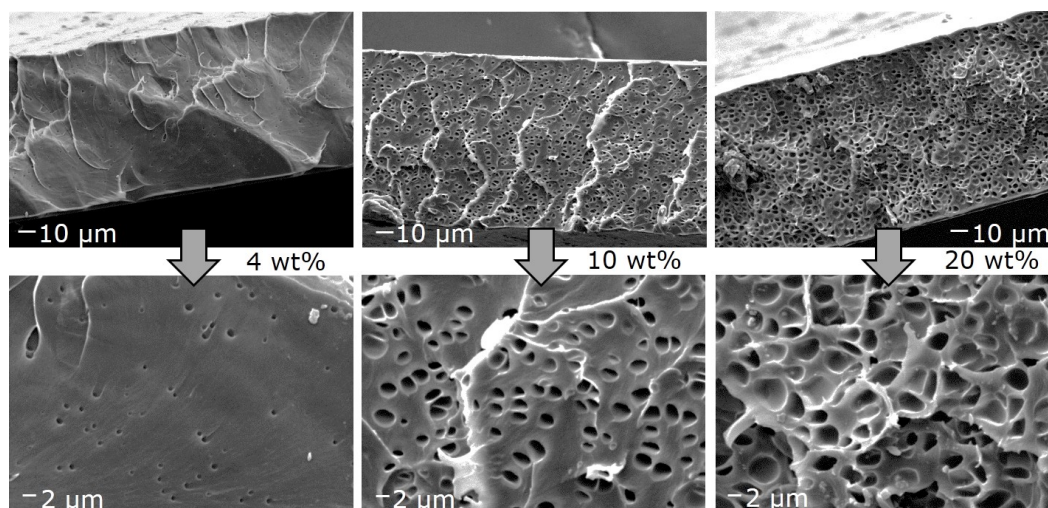


Figure 5.22 – SEM images of cross sections of different MI/PhE-POSS composites MI-04, MI-10, and MI-20.

With increasing PhE-POSS concentration, the number and the size of the “holes” visible in the cross sections of the composites (Figure 5.22) increases as well. It is assumed that those holes occur during the cryogenic fracture where the POSS aggregates are detached from the Matrimid matrix. Therefore, those “holes” are considered to represent the phase-separated PhE-POSS domains originally present in the composite matrix. Sánchez-Soto et al. observed this effect for a polycarbonate-PhE-POSS matrix as well.¹²² A first analysis using simple image processing indicate that the area fraction of the holes corresponds roughly to the concentration of PhE-POSS. Note that the weight fractions are almost equal to the volume fractions as the densities of the both components are approximately similar (Figure 5.16).

As it was already mentioned, the MI/PhE-POSS composites show a strong conductivity distribution at temperatures well below their thermal glass transition temperatures as well. Due to the MWS polarization which occurs in a similar temperature range, this conductivity cannot be analyzed quantitatively for the composites.

5.2.4 Conclusions

Dielectric properties of pure Matrimid and the nanocomposites were analyzed by Broadband Dielectric Spectroscopy. Pure Matrimid displayed one relaxation process pointed as β^* -relaxation and a conductivity contribution. The activation energy of the β^* -relaxation was relatively high ($E_{A,\beta^*} = 99$ kJ/mol) compared to solely β -processes for other glassy polymers. Furthermore, the β^* -relaxation was found at comparatively high temperatures close to the glass transition temperature which is also not characteristic for beta processes. Thus, it was assumed that the β^* -relaxation has to be of a cooperative nature due to $\pi-\pi$ -stacking of the phenyl rings of Matrimid. The influence of the thermal history on Matrimid was analyzed with BDS as well. Those results and Differential Scanning Calorimetry measurements indicated an annealing effect, leading to a more dense packing of the polymer chains and thus to higher activation energies and higher T_g .

The conductivity contribution of Matrimid and the nanocomposites were found to be well below their glass transition temperature. This led to the conclusion that, for Matrimid, the conductivity is not directly related to segmental dynamics. As discussed above, agglomerates of stacked phenyl groups by $\pi-\pi$ -interaction were found with wide angle X-ray scattering. Due to this $\pi-\pi$ -stacking, charge transport in Matrimid is enhanced as well.

Additionally, dynamic-mechanical properties were investigated using DMA. Basically, the dielectric and mechanical properties of Matrimid showed similar results. For the loss modulus, a β^* -relaxation at lower and an α -relaxation (dynamic glass transition) at higher temperatures was observed. In this high temperature range, a strong increase for the loss part of the compliance was observed, proving the onset of flow. Dynamic-mechanic and dielectric measurements evidenced that the β^* -relaxation consists of two processes which merge together for higher frequencies (loss modulus) or temperature (dielectric loss). This was further manifested by WAXS pattern displaying two different spacings for stacks. It was concluded that the observed two modes of the β^* -relaxation are due to different aggregates.

Up to a PhE-POSS concentration of 4 wt%, POSS was dissolved on a molecular level in Matrimid. For higher PhE-POSS concentrations, BDS results evidenced a Maxwell-Wagner-Sillars polarization, indicating a phase separated structure. This

assumed structure was further evidenced by SEM images, where, after prior breaking with liquid nitrogen, cavities on the surface of the fracture edge were observed.

5.3 Gas Transport Properties

Compared to polystyrene and polycarbonate used in previous studies^{115,118,119} Matrimid has a more rigid structure, which leads to a higher free volume and thus, improved gas transport properties. A main disadvantage of Matrimid is a strong tendency to plasticization.^{15,137}

Bos et al. observed reduced plasticization (CO₂) for heat-treated Matrimid/Thermid FA-700 blends compared to a pure Matrimid film.¹³⁷

Recently, several groups analyzed the influence of different nanofillers such as carbons,²⁵ metal-organic frameworks (MOFs),²⁵ zeolites^{27–29} and silicas³⁰ in Matrimid on its gas transport properties. Kanehashi et al. observed improved gas permeabilities as well as selectivities for mixed matrix membranes of Matrimid and different carbon nanoparticles.²⁵

In this study PhenethylPOSS was mixed in Matrimid because an interaction of the phenyl substituents of POSS with the π -system of Matrimid is expected and thus, probably stabilizes the Matrimid matrix to reduce e.g. plasticization, as discussed above.

5.3.1 Gas Permeability

N₂, O₂, CH₄ and CO₂-permeability was measured for MI-00, MI-01, MI-02, MI-04, MI-07, MI-10 and MI-15 (table 5.1) with the time-lag method (1 to 20 bar at 308 K (35 °C)). In the following discussion, permeability, diffusion coefficients and selectivity for Matrimid and Matrimid/PhE-POSS are discussed.

5.3.1.1 Permeability

Figure 5.23 presents a 3D representation of the CO_2 -permeability versus upstream pressure p_1 and $c(\text{PhE-POSS})$ at 308 K for Matrimid and selected Matrimid/PhE-POSS composites.

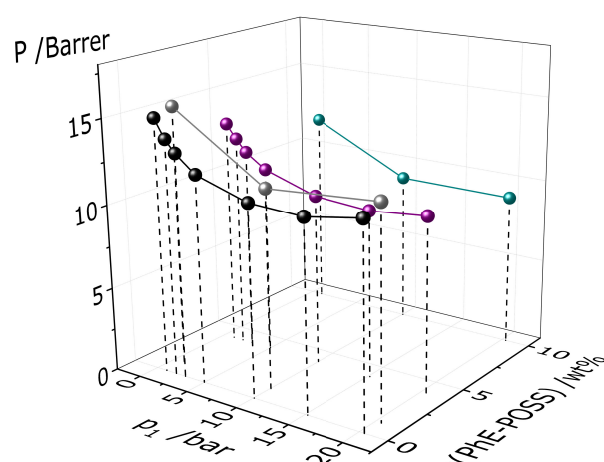


Figure 5.23 – CO_2 permeability vs. upstream pressure p_1 and $c(\text{PhE-POSS})$ at 308 K for the investigated MI/PhE-POSS composites.

The CO_2 -permeability of MI-00 and low concentrations of POSS up to 4 wt% show a “minimum” at 10 bar and increases with further increase of pressure. On a first sight, this behavior is different for 10 wt% of POSS. The permeability of MI-10 remains constant after the first decrease of the permeability. So it seems that for POSS concentrations above 10 wt% the CO_2 -induced plasticization at higher pressures (>10 bar) is suppressed.

In Figure 5.24 the permeability for all analyzed samples are shown in its pressure dependence and were moreover compared to data from Bos et al.¹⁵

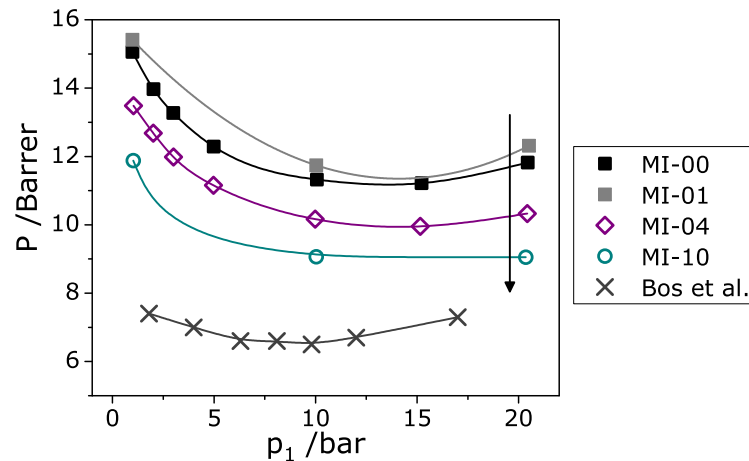


Figure 5.24 – CO₂ permeability vs. upstream pressure p_1 at 308 K for MI-00, MI-01, MI-02, MI-04, MI-07, MI-10 and MI-15. Furthermore, data for Matrimid from Bos et al. is included.¹⁵

The permeability of MI-00 first decreases with increasing CO₂ pressure to a “minimum” at about 10 bar and then increases with further increase of the pressure due to CO₂-induced plasticization. For concentrations up to 4 wt% a slight “minimum” is visible as well, however, for higher POSS concentrations the permeability remains constant after 10 bar. MI-01 shows a slight increased permeability compared to pure Matrimid (MI-00). In contrast, higher POSS concentration leads to overall decreased permeabilities compared to MI-00.

The decrease of the permeability below 10 bar can be explained by the Dual-Mode behavior, where an increase of pressure leads to a decrease of the solubility. In case of highly soluble gases, like CO₂, plasticization occurs, leading to an increase of the permeability at higher pressures. Bos et al.¹⁵ have shown such a plasticization effect for Matrimid as well (see Figure 5.24). In contrast to the used sample preparation procedure used in this study, Bos et al. removed the film after drying from the used glass plate with a small amount of water dried their Matrimid film at 150 °C for 4 days. These differences in film preparation can be the reason for the differences of the absolute values of their permeabilities.

The Dual-Mode behavior is present for all composites shown in Figure 5.24 up to 10 bar. In contrast to 1 wt% of POSS, the permeability for the other composites is lower compared to pure Matrimid (MI-00). This effect supports the assumption made in the previous section for the density and determined T_g s, that POSS is dissolved in the free volume sides of Matrimid. This leads to a hindered gas transport through the

polymer matrix and thus, decreased permeabilities with increasing POSS content. The internal structure of MI-01 is assumed to be more open compared to MI-00 and thus, the permeability is slightly enhanced.

In section 5.2 a phase separated structure was assumed for POSS concentrations higher than 8 wt%, which was evidenced by DSC (Fig. 5.15) and density measurements (Fig. 5.16). In contrast, the BDS results, shown in the previous section, show a phase separation already at about 4 wt%, which was also evidenced by the second heating cycle of DSC measurements. The analyzed BDS data was taken from the second cooling cycle. Here, in contrast to the gas transport measurements the samples were heated up once to 473 K and to 573 K, leading to a more dense structure and thus, to phase separation at about 4 wt%.

For low POSS concentrations, POSS is dissolved on a molecular level in the free volume sites of Matrimid. At about 8 wt%, the free volume is filled up and phase separation occurs, POSS agglomerates are formed. It is assumed that the POSS molecules join somehow the postulated $\pi - \pi$ -stacking and thus, with increasing POSS concentration the polymer matrix is more and more stabilized. Thus, plasticization is reduced with increasing POSS concentration (see Figure 5.24) but at the same time the permeability is decreased because the POSS domains are assumed to be impermeable.¹¹⁵

In Figure 5.25 the permeability of N₂, O₂, CH₄ and CO₂ versus the PhE-POSS concentration is shown for 10 bar and 308 K.

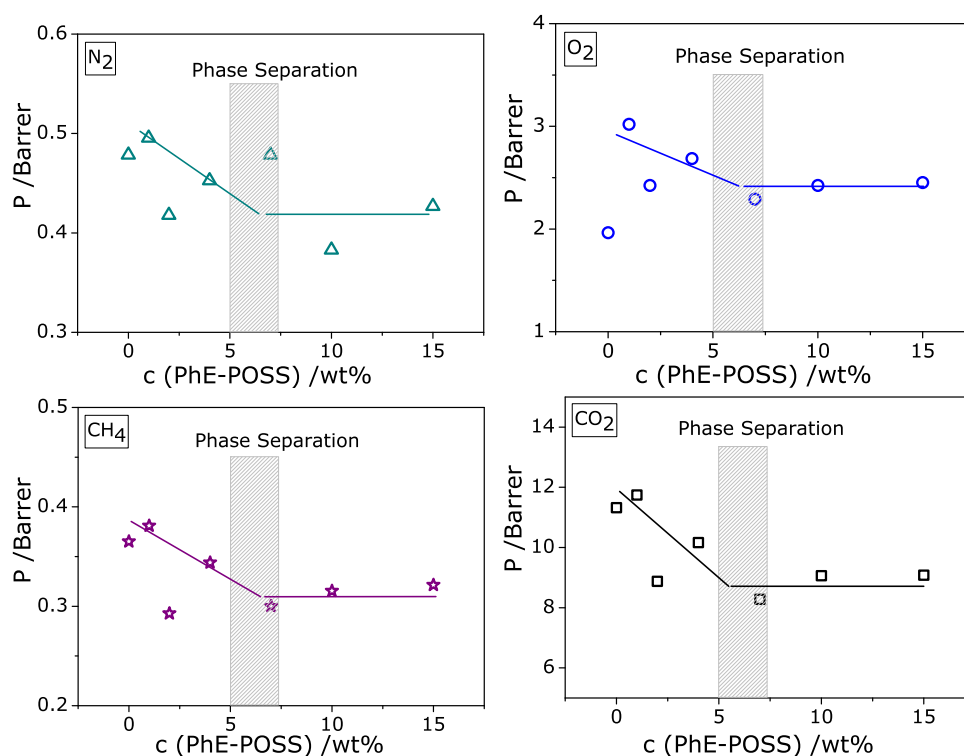


Figure 5.25 – Permeability of N₂, O₂, CH₄ and CO₂ vs. c(PhE-POSS) at 308 K and 10 bar. Lines are guides to the eyes. The gray background indicates the phase separation range observed for BDS/density in section 5.2.

The permeability decreases with increasing POSS concentration for all analyzed gases. After the assumed phase separation at about 8 wt%, the permeability remains almost constant. Furthermore, the permeability of MI-01 is higher compared to MI-00 for all analyzed gases.

With increasing POSS concentration up to the assumed phase separation at about 8 wt% the free volume of Matrimid is filled up. This assumption was already supported by the increase of the density with increasing POSS concentration, shown in Figure 5.16. The permeability of a penetrating gas is related to the free volume as it jumps from "hole" to "hole". Thus, the permeability decreases with increasing POSS concentration. When the phase separation sets in, POSS agglomerates are formed and the free volume sites are filled up. Thus, the composition of the Matrimid/PhE-POSS matrix remains constant, means the interaction between polymer and filler does not change with further increasing POSS concentration. For these reasons, the permeability is constant for higher POSS concentrations.

It is known that high concentrations of silicon atoms incorporated in a polymer matrix

can lead to an increase of the O_2 solubility.^{138–141} Thus, here with increasing POSS content within Matrimid the O_2 -permeability is enhanced as well. However, this effect becomes less for the phase separated samples, the O_2 permeability is almost constant with a further increase of the POSS concentration.

The increased permeability (for all gases) of MI-01 may be ascribed to a looser chain packing in the cast film compared to pure Matrimid MI-00. Thus, small amounts of POSS lead to enhanced gas transport properties, which was also observed for other polymer matrices like PIM-1 (see section 6.3 and ref.²²).

5.3.1.2 Diffusion Coefficients

The diffusion coefficients D were obtained by eq. 2.26 and are shown for N_2 , O_2 , CH_4 and CO_2 vs. the PhE-POSS concentration for 10 bar and 308 K in Figure 5.26.

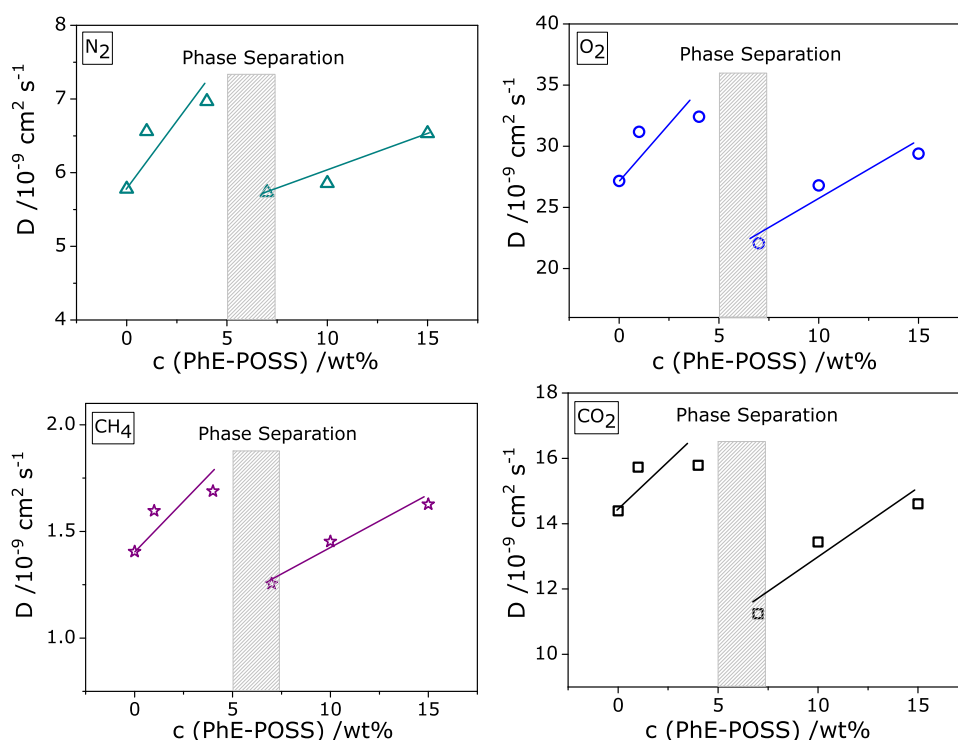


Figure 5.26 – Diffusion coefficients of N_2 , O_2 , CH_4 and CO_2 vs. $c(\text{PhE-POSS})$ at 308 K and 10 bar. Lines are guides to the eyes. The gray background indicates the phase separation range observed for BDS/density in section 5.2.

For all analyzed gases the diffusion coefficient shows the same dependence on the PhE-POSS concentration. For the phase separated as well as the non-phase sepa-

rated samples D increases with increasing POSS content. When the phase separation sets in, the diffusion coefficient changes significantly.

The incorporation of POSS leads a facilitated diffusion even though it is assumed that the free volume sites are filled up. The significant change of the diffusion coefficients at the assumed critical concentration for phase separation, indicates a considerable change of the internal structure. Interestingly, with further increase of the POSS concentration, the diffusion coefficients increases again for the already phase separated structure. This indicates a decrease of the solubility as the permeability is almost constant for the phase separated samples.

5.3.1.3 Selectivity

In addition, the selectivities of O_2/N_2 and CO_2/CH_4 versus the concentration of POSS within the composites are presented in Figure 5.27.

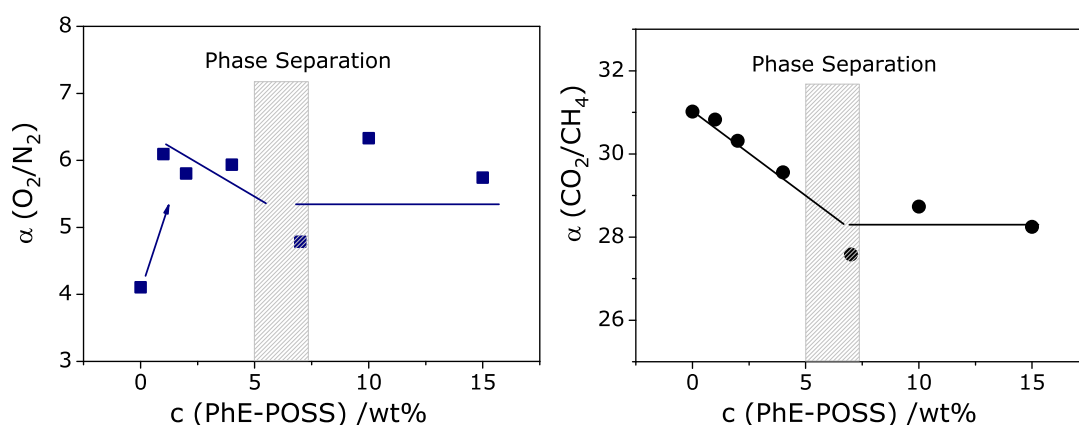


Figure 5.27 – Selectivity of O_2/N_2 and CO_2/CH_4 vs. $c(\text{PhE-POSS})$ at 308 K and 10 bar. Lines are guides to the eyes. The gray background indicates the phase separation range observed for BDS/density in section 5.2.

By incorporation of POSS within the Matrimid matrix the O_2/N_2 selectivity is improved for all composites compared to pure Matrimid. In contrast, the CO_2/CH_4 selectivity is debased significantly with the incorporation of POSS until the phase separation occurs. For the phase separated composites, both selectivities changes dramatically and then, with further increasing POSS concentration α is almost constant.

As it was already discussed the POSS molecules are dissolved in the free volume sites of Matrimid, leading to a densified structure and thus, to a hindered gas transport through the Matrimid matrix especially for the bulky gases CO₂ and CH₄. However, $\alpha(\text{O}_2/\text{N}_2)$ is improved by the incorporation of POSS within the Matrimid matrix, which can be explained by the already mentioned special interaction of the O₂ molecules with the silicon atoms of POSS.

5.3.2 Conclusions

Gas transport properties of Matrimid and Matrimid/PhE-POSS composites were investigated by the time-lag method for N₂, O₂, CH₄ and CO₂ at 308 K (35 °C).

The assumed phase separation at about 8 wt% was in evidence for permeability, diffusion coefficients as well as the selectivities of the Matrimid/PhE-POSS composites. Furthermore, an enhanced permeability for all analyzed gases was observed for 1 wt% of POSS (MI-01), indicating a more open structure compared to pure Matrimid. In addition, the plasticization effect of CO₂ was reduced for the phase separated composites.

6 PIM-1 and PIM-1/POSS Nanocomposites^{*†}

Abstract

Molecular dynamics and conductivity of PIM-1 and PIM-1/PhE-POSS were investigated by BDS. For pure PIM-1 one relaxation process denoted as β^* -relaxation and a conductivity contribution was found. Due to a high activation energy of 86 kJ/mol the β^* -relaxation was assigned to agglomerates formed by $\pi - \pi$ -stacking of the phenyl rings of PIM-1. The PIM-1/PhE-POSS showed a miscibility up to 15 wt%. For higher POSS concentrations a phase separated structure was observed. The conductivity phenomena was explained by $\pi - \pi$ -stacking as well.

Furthermore, gas permeability was determined with the time lag method (0 – 20 bar upstream pressure) at 35 °C for N₂, O₂, CH₄ and CO₂ for PIM-1 and depicted PIM-1/PhE-POSS composites. For 1 wt% of POSS, an enhanced permeability was found for all gases compared to pure PIM-1.

6.1 Introduction

While previously studied polymers with very high fractional free volume and extremely high gas permeabilities, e.g., polyacetylenes such as PTMSP, show only poor selectivities, most PIMs exhibit an attractive combination of almost as high permeabilities with reasonable permselectivities. Therefore, PIMs today represent

^{*}Similar content (section 6.1 and 6.2) was published in Konnertz, N.; Ding, Y.; Harrison, W. J.; Budd, P. M.; Schönhals, A.; Böhning, M., *ACS Macro Letters*, 2016, 5, 528-532.

[†]Similar content (section 6.3) submitted to Konnertz, N.; Ding, Y.; Harrison, W. J.; Budd, P. M.; Schönhals, A.; Böhning, M. *Journal of Membrane Science*

the current state-of-the-art in air separation and hydrogen recovery.^{18,19} All these superglassy polymers share a distinct tendency to physical aging, which is the major drawback with regard to practical membrane applications. After formation of the dense film (or thin selective layer) sometimes followed by a nonsolvent treatment in order to exchange residual casting solvent the initial permeability decreases significantly with time.^{20,21} Therefore, one of the current research topics in the field aims at the suppression of physical aging either by optimizing the chemical architecture of the polymers or by adding suitable (nano)fillers which stabilize their structural arrangement in the glassy state.^{20,22–24}

For conventional glassy polymers, a correlation between certain molecular motions of the solid polymeric matrix and the diffusion of small molecules within can be observed. This follows from fundamental transport models^{44,45} and molecular dynamics simulations^{46,47} and is also discussed based on experimental data.^{48,49} For the superglassy high free volume polymers such a correlation no longer holds as the transport mechanism is obviously different. Distinct differences are found in terms of the corresponding activation energies.^{142,143} This is also in agreement with a continuous free volume phase, found, e.g., in detailed atomistic molecular dynamics simulations of such polymers.^{144,145}

An investigation addressing the molecular mobility of PIMs is of great importance, as two major phenomena which determine the practical performance in membrane application, i.e., the physical aging and the plasticization induced by highly sorbing penetrants, are directly related. Furthermore, the film formation during casting, i.e., the solidification of the polymer by solvent evaporation, is predominantly governed by the molecular mobility of the polymer matrix. Thus, systematic studies of various PIMs as well as corresponding nanocomposites will substantially contribute to further developments toward practical applications of PIMs in membrane separations especially as BDS is complementary to investigations using X-ray scattering^{146,147} or addressing electronic properties of PIMs.¹⁴⁸

6.2 Dielectric Investigations: PIM-1

In this chapter the first synthesized and most representative PIM-1 (Figure 4.3) is investigated by Broadband Dielectric Spectroscopy (BDS).

It has to be noted that for PIMs in general no thermal glass transition is observed below the decomposition.¹⁶ A DSC measurement of PIM-1 is shown in Fig. 4.2. The decomposition starts at about 640 K (370 °C), so we do not expect to find a related dynamic glass transition (segmental dynamics, α -relaxation) in the applied temperature range.

In Figure 6.1 the temperature-dependent dielectric loss $\log \varepsilon''$ at a fixed frequency of 1000 Hz is plotted for the two heating runs and the cooling run between them.

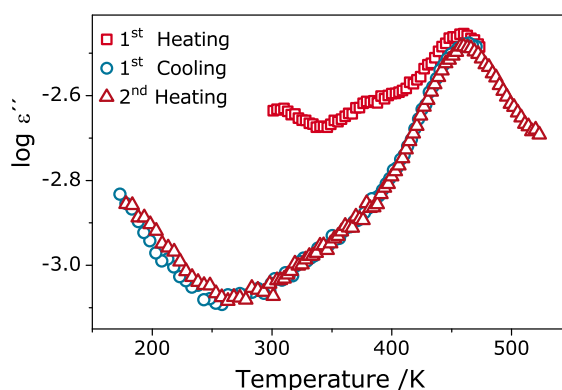


Figure 6.1 – Comparison of dielectric spectra ($\log \varepsilon''$ vs. temperature) at a fixed frequency of 1 kHz for the different heating and cooling runs.

A significant difference between first heating and the two subsequent runs is revealed. The dielectric loss curve of the first heating shows one distinct peak and a shoulder. The peak at higher temperatures, around 460 K (187 °C), can be assigned to a molecular relaxation process which is found similarly during the first cooling and second heating. It has to be noted that the dielectric loss in the first heating run, up to about 400 K (127 °C), is in general significantly higher than in the subsequent measurements. This is probably caused by the remaining solvent molecules. Together with the adumbrated shoulder around 313 K (40 °C) this indicates rather the evaporation process than a higher molecular mobility due to plasticization by traces of solvent. Also the influence of water, sorbed from the atmosphere, might be taken into account, for which a strong effect on the gas transport properties due to partial blocking of the accessible free volume is well-known.^{142,149}

The curves of the dielectric loss measured during first in this temperature range — and also show the distinct relaxation peak around 460 K (187 °C). The observed onset at lower temperature points at a second relaxation peak below 200 K (−73 °C),

but this can unfortunately not be fully characterized within the temperature range accessible for the BDS measurements.

Figure 6.2 shows a three-dimensional representation of the BDS measurement, i.e., the dielectric loss $\log \epsilon''$ versus frequency $\log f$ and temperature T .

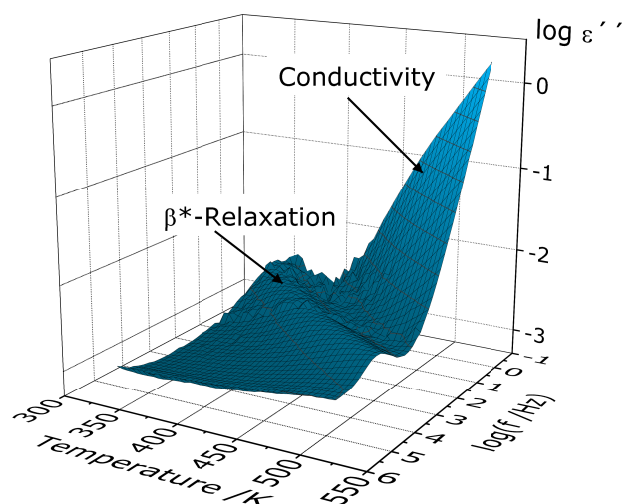


Figure 6.2 – 3D representation of the dielectric loss $\log \epsilon''$ of PIM-1 vs. frequency and temperature for the second heating run.

The peak of the molecular relaxation of PIM-1 is clearly seen, and as expected it shifts to higher frequencies with increase of temperature. The increase of dielectric loss with decreasing frequency (and increasing temperature) is due to conductivity, which is related to the drift motion of charge carriers in the film. For further analysis of the relaxation process, the Havriliak–Negami function (eq. 3.12) was fitted to the data, according to Figure 5.4.

In Figure 6.3 the determined frequencies of maximal dielectric loss are plotted in Arrhenius coordinates.

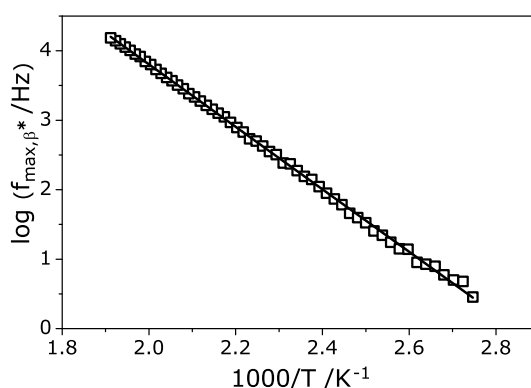


Figure 6.3 – Plot of the frequency of maximal dielectric loss f_{max,β^*} in Arrhenius coordinates.

At first glance, the linear behavior seems to indicate a localized molecular relaxation process, usually denoted as β -relaxation, which is typically found for most polymers. In contrast to that, cooperative segmental relaxation processes usually follow a Vogel–Fulcher–Tammann (VFT) law, distinctly deviating from the linear Arrhenius behavior. An activation energy of $E_A = 86.1$ kJ/mol is obtained for the PIM-1 under investigation. This value is relatively high for commonly observed local β -processes in polymers. For that, usually activation energies between 40 and 60 kJ/mol are expected. A similar phenomenon was also found for example in poly(ethylene naphthalate) (PEN). The activation energy of the β^* -relaxation (E_{A,β^*}) for PEN is in the similar range as the value obtained for PIM-1. For PEN this is ascribed to the formation of intermolecular sandwich-like agglomerates of aromatic moieties of the polymer chain with strong interaction of the respective π -systems.^{129–131}

This leads to higher activation energies and a more cooperative character of the molecular relaxation process. Moreover, a similar behavior was found for Matrimid, discussed in section 5.2.2.

Although for PIMs generally a limited molecular mobility is assumed due to their rigid structure, which leads to the low packing density and the exceptional gas transport properties, a somewhat similar reason for the higher activation energy should be considered. Preliminary wide-angle X-ray measurements of our film sample show several broad reflections which evidence such aggregates with a molecular spacing of about 3.4 and 10 Å¹³³ (see Figure A.4), which is in agreement with earlier investigations of PIM-1 reported in refs.,^{146,147} Due to the resulting partial cooperative character, the observed molecular relaxation process of PIM-1 is denoted as

β^* -relaxation.

For a further analysis of the dielectric behavior of PIM-1, also the conductivity is considered – especially because of the postulated $\pi - \pi$ stacking of the aromatic moieties of the polymer chain, which may have a distinct influence on the conductivity mechanism.

The frequency dependence of the real part of the complex conductivity σ' (Figure 6.4) shows the typical behavior expected for semiconducting polymeric materials.

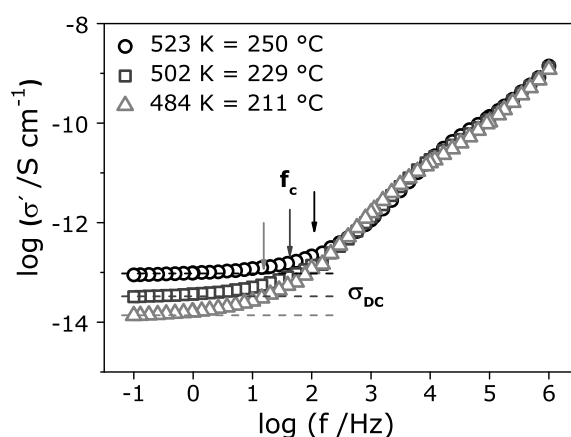


Figure 6.4 – Frequency dependence of the real part of the complex conductivity σ' at the indicated temperature.

For high frequencies the real part σ' decreases with decreasing frequency with a power law down to a characteristic frequency f_c , where a plateau value is reached. The plateau value corresponds to the DC conductivity σ_{DC} .¹⁵⁰ As can be seen from Figure 6.4, this DC conductivity increases with increasing temperature. Figure 6.5 shows a linear behavior for the plateau values σ_{DC} in dependence of the reciprocal temperature; i.e., the DC conductivity follows an Arrhenius relation. An apparent activation energy of $E_{A,\sigma_{DC}} = 101$ kJ/mol was estimated, which is significantly higher than the activation energy of the β^* -relaxation.

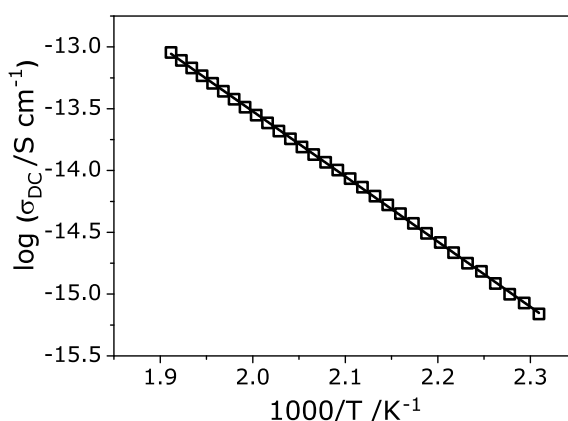


Figure 6.5 – DC conductivity σ_{DC} for PIM-1 in dependence of the inverse temperature. The lines are fits of the Arrhenius equation to the data.

It is necessary to note that the conductivity contribution was observed in the glassy state. For most conventional polymers the transport mechanism of charge carriers is due to mobility of charge carriers (impurities) connected with segmental dynamics of the polymer matrix above the glass transition, and therefore the DC conductivity follows VFT-behavior.

For PIM-1 no glass transition is observed before decomposition. Therefore, it is concluded that for PIM-1 the conductivity is not directly related to segmental dynamics. As discussed above wide-angle X-ray scattering measurements show evidence of agglomerates probably of stacked phenyl groups by $\pi - \pi$ interaction. Due to the overlapping π -systems charge transport in PIM-1 is enhanced.

It has to be noted that the PIM-1 sample shows a distinct change in color after the temperature cycle of the BDS measurement (Figure 3.6). As can be seen from the photographs in Figure 6.6, the color changes from yellow to brownish.

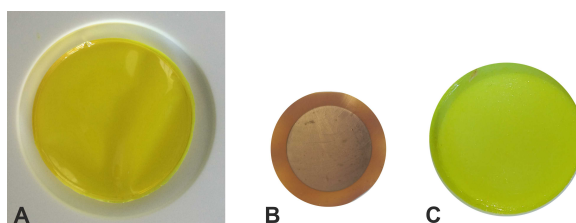


Figure 6.6 – Photographs of the freshly cast PIM-1 film (approx. 70 mm diameter) (A) and of the sample after the BDS measurements (B) — here the outer ring represents the real colour as the central part of about 20 mm diameter is covered with a thin gold layer. (C) shows the PIM-1 from (B) after re-dissolving in chloroform.

A comparison of FTIR spectra for the virgin and the BDS-measured sample (Figure 6.7) does not show any changes. Furthermore, the strongly annealed material regains its original yellow color after being redissolved in chloroform. So, no indications for changes in the chemical structure were found, and an only reversible change of the amorphous packing in the solid film may be concluded.

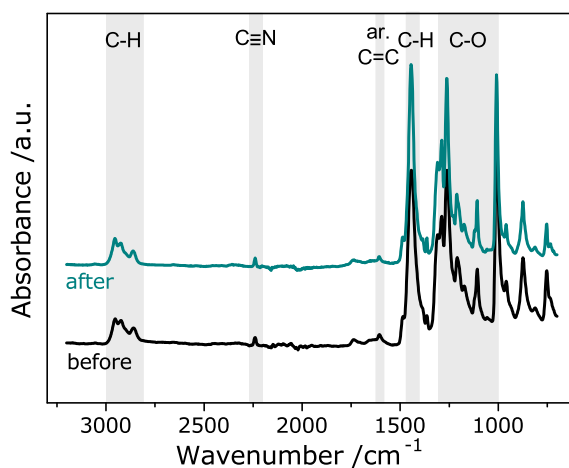


Figure 6.7 – FTIR spectra of PIM-1 before and after the temperature cycle up to 573 K (300 °C).

6.2.1 Conclusions

In conclusion, a molecular relaxation process with Arrhenius behavior and an unusually high activation energy, denoted β^* , has been observed in PIM-1, together with a significant conductivity in the glassy state. As expected, no α -relaxation (related to a glass transition) was found. Both the β^* -relaxation as well as the conductivity are explained with the formation of local intermolecular agglomerates due to interaction of π -electrons in aromatic moieties of the polymer backbone ($\pi-\pi$ -stacking). Up to now, this has not been taken into account when film formation, chain dynamics, free volume, and especially gas transport properties of PIMs were discussed. Although the reported findings have to be further investigated — also considering more PIMs in a systematic manner — they represent a new important aspect of this innovative class of polymers.

6.3 PIM-1/POSS Nanocomposites: Molecular Mobility and Gas Transport Properties

Yong et al. reported a study on the suppression of physical aging and plasticization of PIM-1 by incorporation of different POSS nanoparticles with various aliphatic substituents.²²

As it was already mentioned in section 5.1, PhE-POSS was already successfully embedded in novolac resin,¹²³ polystyrene¹¹⁸ and polycarbonate.^{49, 115, 119}

In this study, PhE-POSS was incorporated within PIM-1. Investigations on molecular mobility and gas transport properties of the PIM-1/PhE-POSS composites are discussed in this section and compared to the results found for the Matrimid composites (section 5.2.3).

6.3.1 Characterization

In Table 6.1, sample codes of the nanocomposites as well as pure PIM-1 are given including the PhE-POSS content, the thickness of the films and the measured density.

Table 6.1 – Sample codes with the corresponding PhE-POSS concentration, the film thickness of PIM-1, and the PIM-1/PhE-POSS nanocomposites and the density.

Sample	wt%	Thickness / μm	ρ / g cm^{-3}
PIM-1-00	0	217	1.150
PIM-1-01	1	215	1.149
PIM-1-05	5	119	1.151
PIM-1-075	7.5	238	1.153
PIM-1-10	10	170	1.155
PIM-1-15	15	207	1.157
PIM-1-20	20	193	1.160
PIM-1-30	30	187	1.164
PIM-1-40	40	155	–
PhE-POSS	1.22 ¹¹⁹	–	100

In order to verify the PhE-POSS content, in the nanocomposites TGA was applied under oxidative conditions. Example curves of the residual mass above 900 K for different PhE-POSS concentrations are shown in Figure 6.8a.

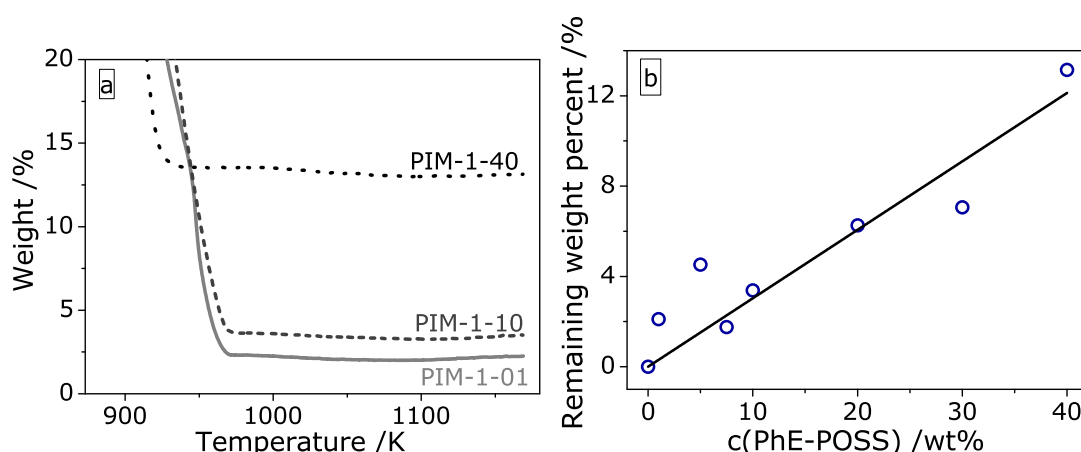


Figure 6.8 – a) TGA curves of PIM-1-01 (solid line), PIM-1-10 (dashed line) and PIM-1-40 (dotted line). b) Remaining weight percent vs. $c(\text{PhE-POSS})$. The solid line is a linear fit to the data.

During heating in the TGA, the polymer matrix and the POSS filler are completely oxidized. Thereby, only Si is assumed to remain in the residue as SiO_2 , as is identified by the plateaus of the TGA curves at high temperatures (Figure 6.8a). With increasing PhE-POSS content, the plateau value increases. Thus, the residual weight is regarded as a measure of the PhE-POSS content. Figure 6.8b shows the final remaining weight vs. the nominal PhE-POSS concentration used for the corresponding formulation. The resulting linear relation confirms this approach. In the following text the samples are identified by their nominal PhE-POSS content.

6.3.2 Relaxation Behavior

A detailed discussion of the dielectric behavior of pure PIM-1 (PIM-1-00) is already included in our previous section 6.2. For PIM-1-00, a significant difference between the first heating and the subsequent runs was observed. This was attributed to remaining solvent and/or absorbed water in the initial state of the sample. During the first heating, these volatile components are lost by evaporation. For this reason, here only the second heating runs of the composites, after heating the samples up to 473 K, are discussed.

In Figure 6.9a, the dielectric loss vs. temperature for the second heating run for PIM-1-00, pure PhE-POSS, and selected composites at 1 kHz are shown. Figure 6.9b presents a stacked overview of the dielectric loss vs. the temperature for all samples.

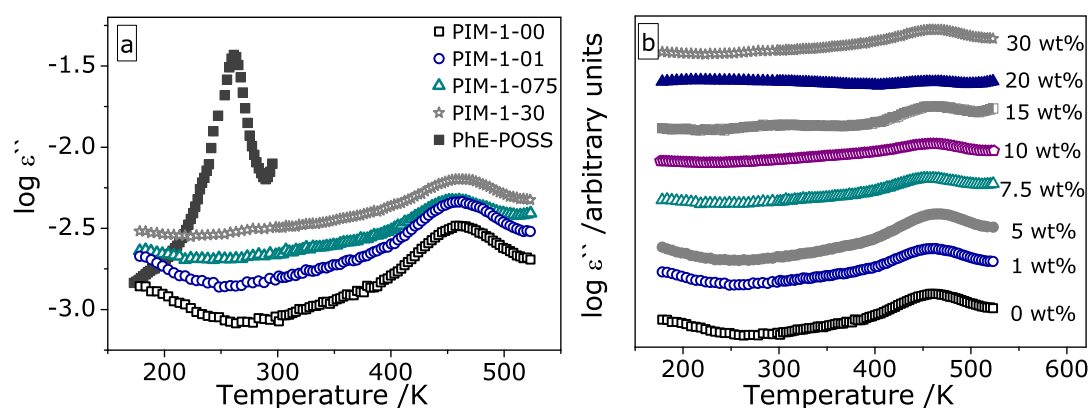


Figure 6.9 – a) Dielectric loss vs. temperature for the second heating of pure PIM-1 (PIM-1-00), of PIM-1 with 1 wt% PhE-POSS (PIM-1-01), 7.5 wt% PhE-POSS (PIM-1-075), 30 wt% PhE-POSS (PIM-1-30) and pure PhE-POSS at a frequency of 1 kHz. b) Stacked dielectric loss vs. temperature for the second heating of pure PIM-1 (PIM-1-00), pure PhE-POSS and of PIM-1/PhE-POSS composites at a frequency of 1 kHz.

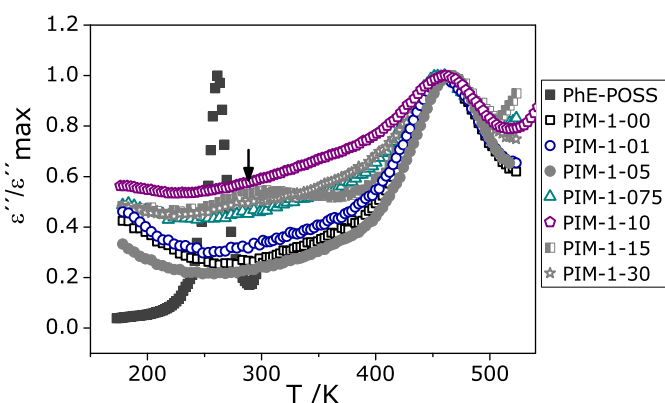


Figure 6.10 – Dielectric loss normalized by the maximum value of the peak vs. temperature for the second heating of PIM-1-00, PIM-1-01, PIM-1-05, PIM-1-075, PIM-1-15, PIM-1-30 and pure PhE-POSS at a frequency 1 kHz

For pure PIM-1, one distinct relaxation process is observed, which is called the β^* -relaxation. This process is assigned to coordinated fluctuations of aggregates caused by π - π -stacking (see section 6.2). For pure PhE-POSS, also one relaxation process is observed, which is due to the dynamic glass transition (α -relaxation) of PhE-POSS (for a more detailed discussion see ref.¹¹⁹). For concentrations of PhE-POSS up to 10 wt%, only the β^* -relaxation related to the PIM-1 matrix is observed as a peak, which indicates miscibility on a molecular level at first glance. However, for PIM-1-15 and PIM-1-30, a weak but distinct second relaxation process becomes apparent.

This second peak can be attributed to the α -relaxation of PhE-POSS located in PhE-POSS rich domains formed by phase separation, because this relaxation process is observed in a temperature range similar to the α -relaxation of pure PhE-POSS. This peak is shifted slightly to higher temperatures compared to the dynamic glass transition of pure PhE-POSS as indicated in Fig. 6.10. This is most probably due to the restricting and/or confining effects of the rigid glassy PIM-1 matrix on the soft PhE-POSS domains. Unfortunately, the nanocomposite with 40 wt% of PhE-POSS (PIM-1-40) was too brittle to perform BDS measurements.

A closer inspection of the normalized dielectric loss curves for PhE-POSS in Fig. 6.10 shows further a significantly rising level of ϵ'' between 220 and 400 K for the intermediate PhE-POSS concentrations up to about 10 wt%. This indicates, according to the fluctuation dissipation theorem, an enhanced molecular mobility in this temperature range. Also, a change in shape of the dielectric loss curves in this temperature range becomes obvious: For pure PIM-1 and the nanocomposites at low PhE-POSS concentrations, the curves exhibit a shape concave to the temperature-axis which disappears above 5 wt% (Fig. 6.9b).

Based on these observations, three concentration ranges may be distinguished for the nanocomposite materials: At low concentrations of PhE-POSS up to about 5 wt% (here denoted as range I), a single, clearly discernible relaxation peak (related to the β^* -relaxation of PIM-1) dominates the dielectric spectrum. In the intermediate concentration range II, i.e. between 5 and 10 wt%, the overall dielectric loss rises significantly with increasing PhE-POSS content. From the normalized dielectric loss curves in Fig. 6.10, it can be seen that the β^* -peak remains nearly unchanged while on both sides the ϵ'' -curve is on a higher level and exhibits slight changes in shape, as mentioned above.

At concentrations above 10 wt% (denoted as range III), the appearance of a second relaxation peak related to the α -relaxation of PhE-POSS is a clear indicator of a phase separation.

From this behavior and the fact that PIM-1 has an extremely high fractional free volume and most probably forms a continuous free volume phase,¹⁵¹ the following (simplified) picture of the investigated nanocomposites is suggested:

At low concentrations, i.e. in concentration range I (characterized by complete miscibility), the PhE-POSS incorporated into the nanocomposite is entirely accommo-

dated in the free volume of PIM-1 in a more or less isolated state. Within these free volume sites, the POSS molecules can fluctuate, causing an increased dielectric loss. As these fluctuations are restricted or constrained by the surrounding PIM-1 matrix, the molecular fluctuations are slowed down compared to the bulk and thus the dielectric loss is also increased at higher temperatures (e.g. compared to the glass transition of pure PhE-POSS). One possible molecular mechanism of the restriction of the molecular PhE-POSS can be the incorporation of one or more phenyl rings of PhE-POSS into the proposed stack-like structure of aromatic moieties of the PIM-1 matrix due to interactions of the π -systems.¹⁵² It seems obvious that for the restriction of the PhE-POSS molecules in the PIM-1 matrix, a broad variety of possibilities exists due to the amorphous structure of PIM-1 and different options to incorporate the phenyl groups of PhE-POSS into the structure of PIM-1. Therefore, the molecular fluctuations become heterogeneous, resulting in a broad relaxation time spectra, which thus lead to a broadly distributed loss ϵ'' (instead of a distinct peak) also in the temperature domain (see Figure 6.10).

As stated above, at low concentrations PhE-POSS exist individually and separately in the free volume sites. With increasing concentration of PhE-POSS, the free volume sites are increasingly filled-up, the PhE-POSS molecules start to recognize each other and the related molecular mobility may be regarded as a pre-stage of the co-operative α -relaxation. In this intermediate concentration range II, this behavior manifests itself as a change in shape of the dielectric loss curves.

At high concentrations (15 wt% and above), a phase separated morphology is observed in which domains of pure PhE-POSS are formed, which enable the fully co-operative motion giving rise to the observed α -relaxation and to the corresponding separate peak in ϵ'' . The small "holes" (< 300 nm), visible in the SEM images of PIM-1-30 and even more pronounced in PIM-1-40 (Figure 6.11), may be taken as an additional indicator of the phase separated structure. During breaking of the previously cooled nanocomposites, PhE-POSS domains are "broken out" of the PIM-1 matrix, leaving holes in the cross section. This effect was described in the previous section for Matrimid/PhE-POSS (5.2.3) and Polycarbonate/PhE-POSS¹²² composites and found by other investigators as well.¹²³

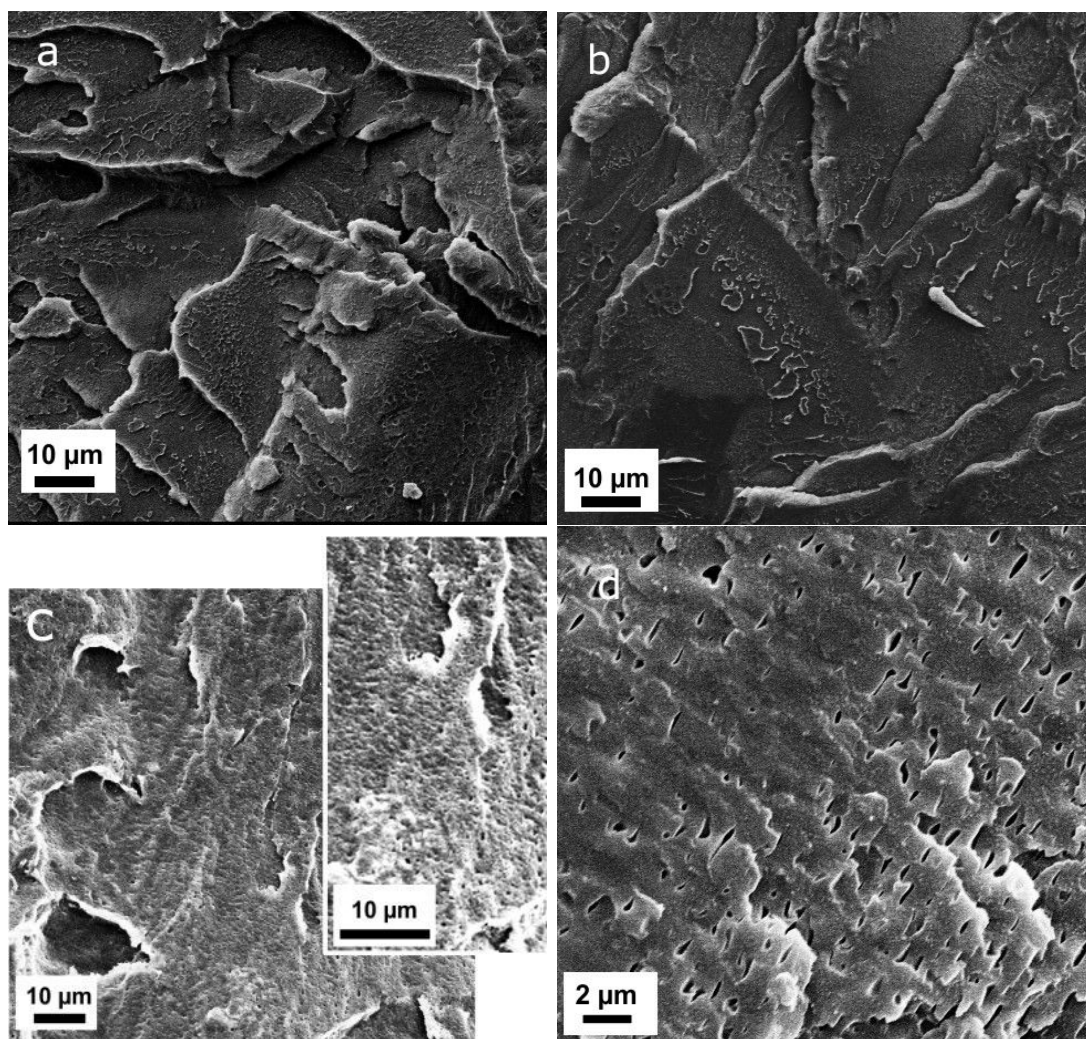


Figure 6.11 – SEM images of the cross sections of a) PIM-1-00, b) PIM-1-10, c) PIM-1-30 and d) PIM-1-40.

For the detailed analysis of the β^* -relaxation of the PIM-1 matrix in the nanocomposites, the model function of Havriliak-Negami (HN-function) (eq. 3.12) was fitted to the data.

Conductivity effects are treated in the usual manner by adding a power law (eq. 3.14) to the dielectric loss. By fitting the HN-function (for examples see Figure 5.4) to the data, the relaxation rate f_{max} (eq. 3.13) is obtained. The relaxation rate corresponds to the frequency of the maximum of the dielectric loss and is given in eq. 2.3. The temperature dependence of the relaxation rate of the β^* -relaxation $\log(f_{max,\beta^*})$ obeys the Arrhenius equation (see Figure 6.12b).

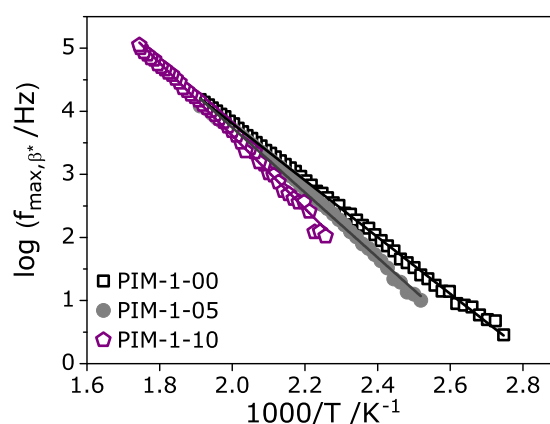


Figure 6.12 – Relaxation rate f_{max,β^*} for the second heating vs. inverse temperature of PIM-1-00, PIM-1-05, and PIM-1-10. The lines are fits of the Arrhenius equation to the corresponding data.

The determined activation energies of the β^* -relaxation E_{A,β^*} for all samples are given in Figure 6.13 as function of the PhE-POSS concentration.

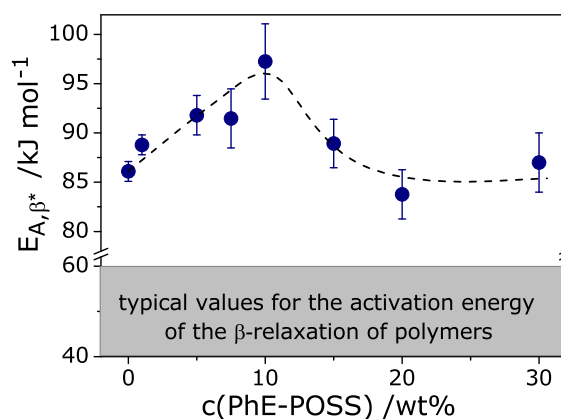


Figure 6.13 – Activation energy E_{A,β^*} for the second heating cycle determined by Arrhenius vs. the PhE-POSS concentration.

As already discussed for pure PIM-1 (section 6.2), the activation energy E_{A,β^*} for the β^* -relaxation is ca. 86 kJ/mol. This value is relatively high compared to β -processes typical for localized fluctuations in conventional polymers (40 to 60 kJ/mol). Therefore, it is assumed that sandwich-like agglomerates are formed due to the interaction between the π -systems of the polymer backbones. For a detailed discussion, see section 6.2 and ref.^{129–131} At first, E_{A,β^*} increases with increasing POSS concentration. Taking into account the simple picture for the nanocomposites derived from the phenomenological analysis of the ϵ'' -spectra, the changes of the activation energies

can be discussed as follows: At low concentrations, the aromatic phenyl moieties of the organic POSS-substituents interact with π -systems of PIM-1 as discussed above. Thus, some of the fluctuating aggregates are interconnected compared to pure PIM-1, resulting in an increased value of the activation energy of the β^* -relaxation. This coincides with concentration range I.

A further increase of the filler concentration leads to formation of small agglomerates of PhE-POSS (concentration range II). In contrast to the individual PhE-POSS molecules, these agglomerates can no longer be completely accommodated within the undisturbed free volume elements of PIM-1. Therefore, they cause a subtle distortion of the surrounding PIM-1 matrix.

This effect still leads to a further increase of the activation energy of the β^* -relaxation for which a maximum value is observed around 10 wt% of PhE-POSS. For concentrations higher than that, phase separation occurs (range III). Here, a part of the constraints and distortions superimposed to the aggregates are removed resulting in a decreasing E_{A,β^*} . Moreover, the PhE-POSS-rich domains of the phase-separated structure will weaken the stack-like arrangement of the phenyl rings of PIM-1. This effect also explains the increasing brittleness of the prepared films above 10 wt% PhE-POSS: the thereby weakened cohesive energy leads to an immediate decline of the mechanical properties, as the formation of entanglements seems unlikely for the rigid PIM-1 and therefore has no stabilizing effect.

The weakened $\pi - \pi$ -interaction of PIM-1 by the disturbed arrangement of its aromatic moieties finally leads to a constant level for E_{A,β^*} which is – rather coincidentally – comparable to that of pure PIM-1.

For composites based on Matrimid and PhE-POSS a different concentration dependence of the activation energy of the β^* -relaxation in dependence was observed (section 5.2.3). E_{A,β^*} (Matrimid/PhE-POSS) was constant up to the phase separation at about 4 wt% PhE-POSS and then decreased compared to the pure polymer. This effect was ascribed to incorporation of small amounts of PhE-POSS molecules within the free volume sites of Matrimid only slightly affecting the internal structure of the polymer. In contrast, PIM-1 has a more rigid structure with a higher free volume. For that reason, even the small distortion due to agglomeration of PhE-POSS within the free volume of PIM-1 weakens the $\pi - \pi$ -interaction, resulting in a decrease of E_{A,β^*} . With further increasing PhE-POSS concentration, phase separation occurs

and the mobility of the PIM-1 chains is enhanced and thus E_{A,β^*} levels off at the value for pure PIM-1.

In order to verify the simplified phenomenological picture, the density of the PIM-1/PhE-POSS composites was investigated in dependence of the nanofiller concentration (see Figure 6.14).

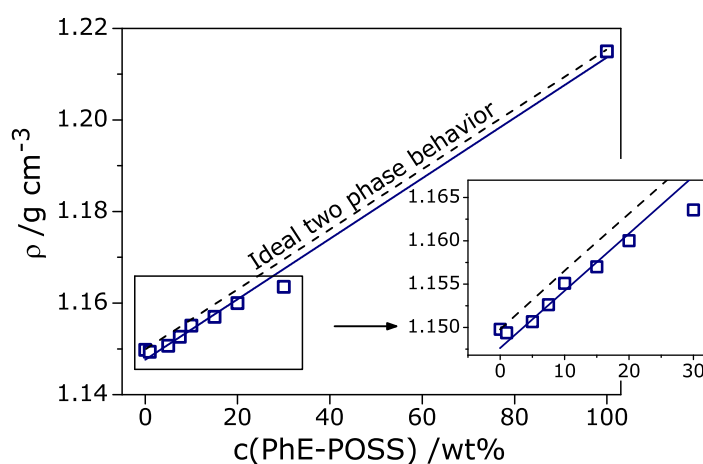


Figure 6.14 – Density of the PIM-1/PhE-POSS nanocomposites vs. $c(\text{PhE-POSS})$. The solid line is a linear fit of all data points and the dashed line sketches the behavior of an ideal two phase system. The inset gives a detailed view on the PhE-POSS concentrations up to 30 wt%. The error bars were estimated based on at least two values.

At first glance, density increases approximately linear with increasing PhE-POSS content. A detailed view on the density of the composites shows that, up to a concentration of 10 wt%, the densities almost follow the ideal behavior – only a slight trend to lower densities seems discernible. This behavior is in agreement with the assumption that PhE-POSS is dissolved in the free volume of PIM-1. When approaching the critical concentration for the occurrence of a phase separated morphology, around 15 wt%, the dependency of the density on the POSS concentration is changed and deviates more clearly from the ideal two-phase behavior. As discussed above, it is assumed that in some regions within the PIM-1 matrix the formation of PhE-POSS aggregates starts to distort the internal structure and meanwhile the free volume is further filled with individual PhE-POSS molecules. At very low concentrations, the second process dominates and thus the density increases further with increasing POSS content. When phase separation sets in, the negative deviation in the density change becomes more pronounced.

It should be noted that the prepared composites of PIM-1 and PhE-POSS are transparent up to the highest concentration of the nanofiller. This means that the domain-size of the phase-separated structure must be smaller than half of the wavelength of visible light. Taking blue light as the visible light with the shortest wavelength, the phase-separated domains should have a maximum size of ca. 200 nm. This is supported by the SEM pictures shown in Fig. 6.11.

This is different to the discussed Matrimid/PhE-POSS composites, where the samples become increasingly turbid for POSS concentration above 4 wt% (see Fig. 4.5). This line of argumentation is also in agreement with the observation that in the dielectric spectra of PIM-1/PhE-POSS nanocomposites no pronounced Maxwell/Wagner/Sillars (MWS) polarization effects have been observed, indicating also that the phase-separated domains should be small and the corresponding MWS polarizations will be observed at higher frequencies than considered here. In contrast to that, the Matrimid/PhE-POSS composites showed pronounced MWS phenomena (see section 5.2.3).

Conductivity

Besides the discussed relaxation processes, conductivity effects are observed surprisingly for the PIM-1/PhE-POSS composites although no glass transition could be measured before decomposition. For most conventional polymers, the mobility of charge carriers is related to segmental dynamics of the polymer and thus conductivity effects in general are observed above T_g .⁶³ As already discussed in section 6.2, it is assumed that conductivity effects of PIM-1 are related to the postulated $\pi - \pi$ -stacking of the polymer segments which supports the charge transport.

In order to analyze this effect in detail, the complex conductivity is used (eq. 3.5). In Figure 6.15a, the real part of the complex conductivity σ' is depicted for PIM-1-075 as function of frequency for different temperatures. In Figure 6.15b, the real part of the complex conductivity σ' versus frequency is shown for different PhE-POSS concentrations at the same temperature.

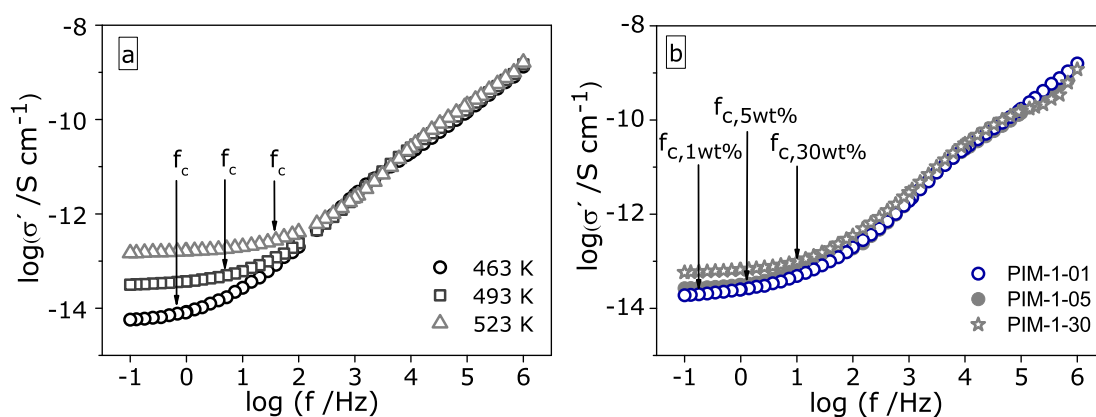


Figure 6.15 – Real part of the complex conductivity σ' vs. frequency for the second heating run of a) PIM-1-075 at different temperatures ($T = 463$ K, $T = 493$ K, $T = 523$ K) and b) for PIM-1-01, PIM-1-05 and PIM-1-30 at 499 K.

The real part of the complex conductivity σ' shows the typical frequency dependence expected for a semi-conducting polymer: σ' decreases with decreasing frequency until a critical frequency f_c is reached where this dependence changes to a plateau (see section 3.1.3). This plateau corresponds to the DC conductivity. The value for the DC conductivity increases with increasing temperature (Figure 6.15a) as well as increasing PhE-POSS content (Figure 6.15b).

The data is approximated by the Jonscher power law (eq. 3.15) and σ_{DC} is obtained by fitting the Jonscher equation to the data.

The DC conductivity σ_{DC} vs. inverse temperature is shown in Figure 6.16a for different PhE-POSS concentrations. The data follow an Arrhenius behavior similar to pure PIM-1 (discussed in section 6.2). The concentration dependence of the activation energy of the conductivity $E_{A,\sigma_{DC}}$ is given in Figure 6.16b.

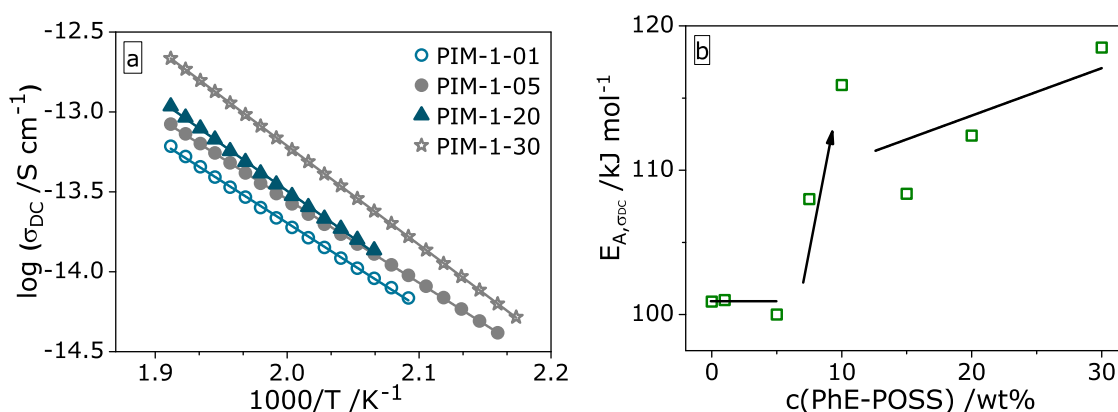


Figure 6.16 – a) Direct current conductivity σ_{DC} for the second heating vs. the inverse temperature of PIM-1-01, PIM-1-05, PIM-1-20 and PIM-1-30. The lines are an Arrhenius fit to the data. b) Activation energy of the conductivity $E_{A,\sigma_{DC}}$ vs. PhE-POSS concentration.

The observed activation energies for the conductivity are larger than those for the β^* -relaxation, as already discussed for pure PIM-1 in section 6.2. This indicates that the conductivity is not directly related to the β^* -relaxation. Up to a PhE-POSS concentration of about 5 wt%, $E_{A,\sigma_{DC}}$ is independent of $c(\text{PhE-POSS})$. This corresponds to region I, as identified for the β^* -relaxation. As already discussed, here small amounts of PhE-POSS can participate in motional processes of the surrounding PIM-1 matrix. For the conductivity, it is assumed that the phenyl rings of PhE-POSS join the $\pi - \pi$ -stacking of the PIM-1 matrix and thus almost not affect the conductivity. With increasing PhE-POSS concentration, the activation energy increases step-like up to about 10 wt% (see Figure 6.16b). This corresponds to concentration range II, where small PhE-POSS agglomerates are formed and the PIM-1 matrix is slightly distorted. This results in a distinct increase of $E_{A,\sigma_{DC}}$ because the stack-like arrangement of the phenyl rings, which supports the charge transport, is disturbed. Above the critical concentration for the phase-separation, i.e. concentration range III, $E_{A,\sigma_{DC}}$ shows a further, but less pronounced, linear increase with increasing POSS concentration due to the further weakening of the $\pi - \pi$ -stacking, as discussed above.

6.3.3 Gas Transport Properties

The gas transport properties of PIM-1 and selected composites were analyzed for N_2 , O_2 , CH_4 , and CO_2 at 35 °C. For a first orientation of the influence of PhE-POSS

on the gas transport properties of PIM-1, small POSS concentration was chosen, where individual filler molecules are completely accommodated in the fractional free volume of the polymer matrix: PIM-1-01 with 1 wt% PhE-POSS. For comparison, a somewhat higher POSS loading, still below the critical concentration of phase separation, was included, where significant changes of the matrix can be expected: PIM-1-075 with 7.5 wt% PhE-POSS.

6.3.3.1 Permeability and Diffusion Coefficients

The effect of PhE-POSS loadings on the permeability (a) and diffusion coefficients (b) of N_2 versus the upstream pressure p_1 is shown in Figure 6.17.

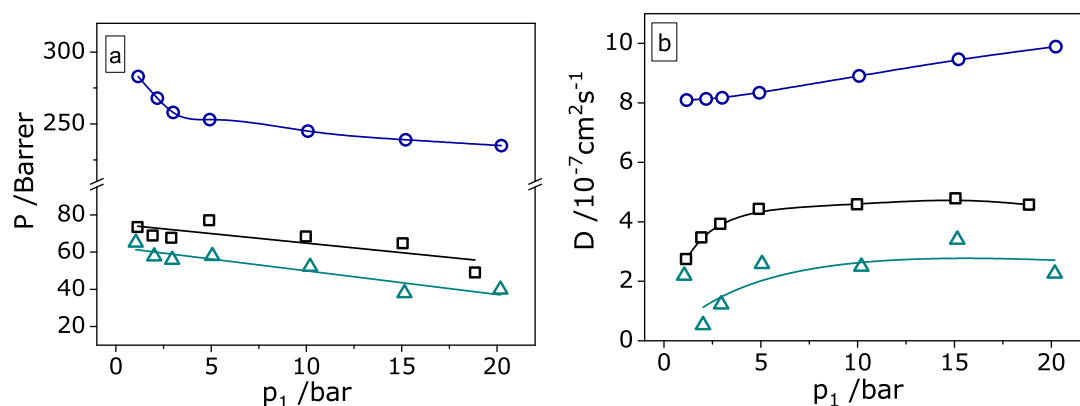


Figure 6.17 – a) N_2 –permeability and b) diffusion coefficients vs. upstream pressure p_1 for PIM-1-00, PIM-1-01 and PIM-1-075 at 35 °C.

In all cases, a decrease of permeability with increasing upstream pressure is observed, while the diffusion coefficients increase slightly. This behavior is in agreement with the dual-mode behavior expected for glassy polymers and was reported earlier by Li et al. for pure PIM-1.¹⁵³ A similar pressure dependence was also found for oxygen and methane, while for carbon dioxide its plasticizing effect seems to dominate – see more detailed discussion below.

Overall, for nitrogen the permeability is increased by a factor of three and the diffusion coefficients by two for PIM-1-01 compared to pure PIM-1, whereas loadings of 7.5 wt% lead to a reduction of the permeability as well as the diffusion coefficients compared to PIM-1-00. In Figure 6.18, the effect of PhE-POSS loadings on the

permeability (a) and diffusion coefficients (b) of O₂ versus the upstream pressure p_1 is shown.

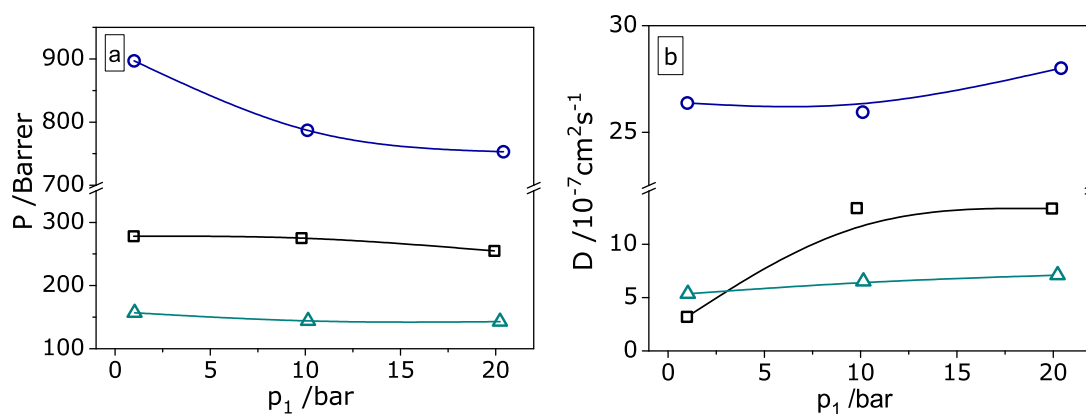


Figure 6.18 – a) O₂ –permeability and b) diffusion coefficients vs. upstream pressure p_1 for PIM-1-00, PIM-1-01 and PIM-1-075 at 35 °C.

As was observed for N₂ (Figure 6.17), the O₂–permeability and the diffusion coefficients are significantly increased as well by loadings of 1 wt% of PhE-POSS (PIM-1-01), whereas higher loadings of 7.5 wt% (PIM-1-075) lead to decreased permeability and diffusion coefficients. The same trend was found also for methane as shown in Figure 6.19.

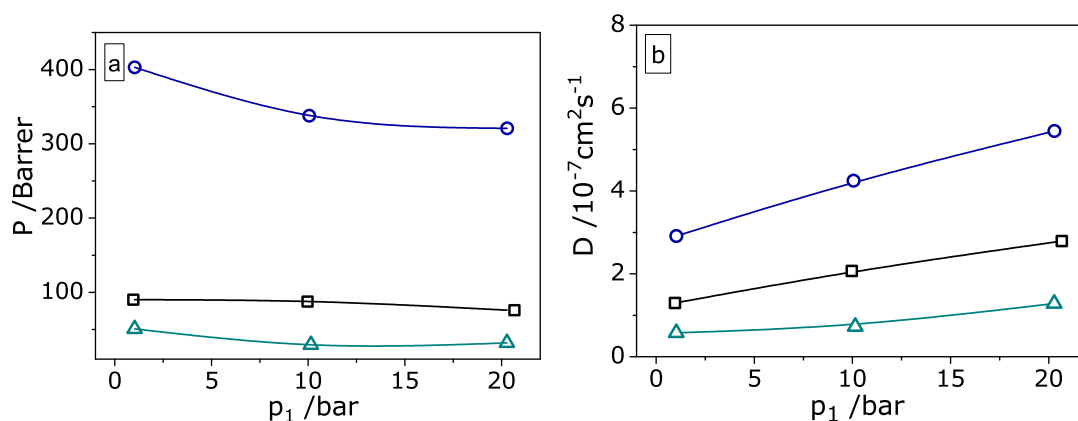


Figure 6.19 – a) CH₄ –permeability and b) diffusion coefficients vs. upstream pressure p_1 for PIM-1-00, PIM-1-01 and PIM-1-075 at 35 °C.

The CO₂–permeability (a) and the diffusion coefficients (b) versus the upstream pressure p_1 are shown in Figure 6.20.

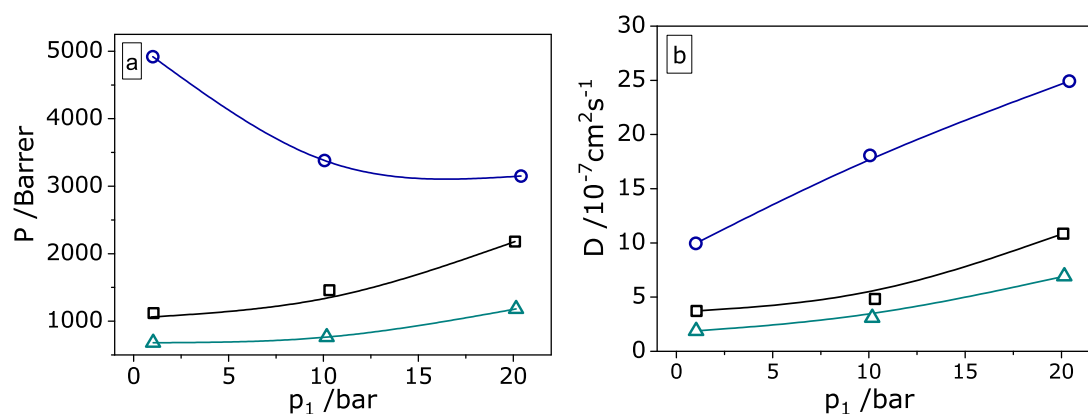


Figure 6.20 – a) CO₂ –permeability and b) diffusion coefficients vs. upstream pressure p_1 for PIM-1-00, PIM-1-01 and PIM-1-075 at 35 °C.

As for N₂, O₂, and CH₄, permeability and diffusion coefficients of CO₂ in PIM-1-01 are significantly higher compared to PIM-1-00 and PIM-1-075. Moreover, for pure PIM-1 (PIM-1-00) and 7.5 wt% (PIM-1-075) a distinct plasticization effect of CO₂ is observed, i.e. not only the diffusivity but also the permeability increases with increasing upstream pressure. In contrast, the CO₂-permeability of PIM-1-01 (1 wt% PhE-POSS) decreases drastically with increasing pressure. The initially much higher permeability of CO₂ in PIM-1-01 may be ascribed to a looser chain packing in the cast film compared to pure PIM-1. It should be noted that the permeation experiments were performed in the order of increasing gas solubility, i.e. N₂, O₂, CH₄, CO₂. So the distinctly increased permeability of PIM-1-01 compared to PIM-1-00 observed for the low solubility gases N₂, O₂ and CH₄ and also for CO₂ at 1 bar is related to this initial state of the film. The plasticizing effect of carbon dioxide is well known and mainly due to its much higher solubility compared to the other gases used in this study. This plasticization effect leads obviously to a collapse of the loosened structure of PIM-1-01 at higher carbon dioxide pressures corresponding to higher concentrations in the polymer. This enhanced physical ageing dominates the permeability in this case. In contrast, PIM-1-00 and PIM-1-075 show a significant increase of CO₂-permeability with upstream pressure due to the plasticizing effect of CO₂, as their more stable structure in the polymer film is less prone to physical ageing. Interestingly, this behavior of the gas transport properties is not directly reflected by the density or BDS data discussed in the first part of this work, indicating that already subtle changes in the structure of a solid film may have a strong impact on the gas transport properties, especially for PIMs.

Nevertheless, for all analyzed gases the permeability and the diffusion coefficients of PIM-1-01 are found to be much higher than for PIM-1-00 and PIM-1-075. Therefore, it may be assumed that PIM-1-01 has a loose, more open structure – also after the partial collapse induced by CO₂ at higher pressures – compared to pure PIM-1, which was also reported by Yong et al. for a PIM-1/POSS composite.²² Thus, small amounts of PhE-POSS generally lead to enhanced gas transport properties of the PIM-1 matrix.

For PIM-1-075, it is assumed that PhE-POSS agglomerates are formed, which occupy the free volume to an extent that they start to distort the surrounding polymer matrix. Consequently, it seems reasonable that this is connected with a reduction in diffusivity and permeability as parts of the free volume may be blocked thereby. Furthermore, these agglomerates may also lead to a rigidification of the adjacent matrix polymer as previously observed for other mixed matrix materials.^{124,154}

Although the findings concerning the gas transport in PIM-1/PhE-POSS nanocomposites are in agreement with the simplified picture developed based on the BDS measurements, the distinct effects of small loadings on diffusivity and permeability are not reflected to the same extent by the BDS data. In view of this complex behavior, a straightforward connection between the two is not expected.

The pronounced tendency to physical ageing of PIM-1-01 and its irreversibility were proven by repeated measurements at the end of our measurement series, including also some experiments at elevated temperatures up to 338 K not shown in this work. Here, the permeability decreased for CO₂ at 1 bar from initially 4920 Barrer (see Fig. 6.20) to 1430 Barrer. Although more detailed investigations concerning the ageing behavior might be necessary, it becomes clear that the potential improvement of the membrane performance cannot be directly utilized in practical applications. A possible approach to stabilize the loosened structure of the PIM-1 matrix could be a covalent crosslinking within the formed solid film, e.g. by partially functionalized POSS fillers.

6.3.3.2 Selectivity

The selectivity of the three materials is examined, taking the technically relevant gas pair CO₂/CH₄ as an example for natural gas upgrading to assess the potential improvement of the nanocomposite system under investigation.

In Figure 6.21 the CO_2/CH_4 selectivity versus CO_2 permeability of PIM-1-00, PIM-1-01 and PIM-1-075 at 35 °C and 1 bar are shown in comparison to the 2008 upper bound.¹²

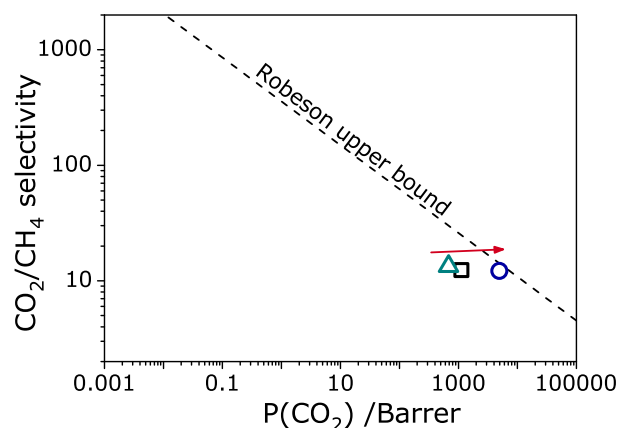


Figure 6.21 – CO_2/CH_4 selectivity vs. CO_2 permeability of PIM-1-00, PIM-1-01 and PIM-1-075 at 35 °C and 1 bar. The line is the Robeson upper bound published in 2008.¹²

By blending 1 wt% PhE-POSS into PIM-1 the gas separation performance is improved – as the permeability is distinctly increased without losing selectivity, the Robeson upper bound is touched by PIM-1-01. In contrast, the loss in CO_2 -permeability observed for PIM-1-075 is not accompanied by an equivalent gain in selectivity. So the potential membrane performance drops significantly for the higher PhE-POSS concentration.

It should be noted at this point that the PIM-1 film investigated here might be somewhat different from that of other investigators with respect to pre-treatment, thickness, casting solvent, and thermal history.¹⁴² Specifically, no solvent treatment of the film with methanol or ethanol was performed in this study, which is known to result in significantly higher permeability values. In contrast, a treatment at elevated temperatures and a thorough degassing was applied before permeability measurements for all materials under investigation.

Thus, the permeability of PIM-1 may be lower than reported elsewhere and therefore not situated directly on the 2008 upper bound, as one might expect. Nevertheless, Figure 6.21 demonstrates the distinct relative effect of PhE-POSS on the permeability of the nanocomposites.

6.3.4 Conclusions

As reported in the previous section, Broadband Dielectric Spectroscopy (BDS) reveals some important features of PIM-1, such as the unusually high activation energy of the localized relaxation process (β^*) due to $\pi - \pi$ -stacking as well as significant conductivity in the glassy state below T_g , which may be relevant for a deeper understanding of the film formation process and resulting membrane performance as well as for other applications of polymers of intrinsic microporosity. Furthermore, BDS results help to characterize the effects of the nanoscaled fillers with respect to miscibility, phase behavior and free volume of PIM-1/PhE-POSS nanocomposites. Investigations of the gas transport properties show drastic increases of diffusivity and permeability for very low filler concentrations, demonstrating that particularly subtle changes lead to effects on the membrane performance of PIM-1 based materials. Changes observed for 1 wt% PhE-POSS in PIM-1 point towards the Robeson upper bound indicating a substantial improvement in membrane performance. But the pronounced trend to physical aging prevents a direct utilization of these improvements. So the stabilization of such a modified structure of the polymer in the solid state remains the key challenge for further developments in this field.

7 Conclusions and Outlook

7.1 Conclusions

Polymeric membranes are increasingly used in industrial gas separation applications. However, novel polymers demonstrate much better gas transport properties than current state of the art membrane materials. One negative effect of today's polymeric membranes is the tendency to plasticization for certain gas separation processes. In this thesis a detailed structure/property study is performed on the commercially available and commonly used Matrimid, compared to the high performance polymer PIM-1. Both polymers exhibit good gas transport properties but show strong tendencies to physical aging and plasticization. Furthermore, this work comprises the impact of a nanofiller embedded into both polymers on the structure/property relationship.

Films of Matrimid and PIM-1 as well as their variations with PhenethylPOSS (PhE-POSS) as nanofiller, respectively, were prepared by solution casting. The PhE-POSS concentration varied from 0 - 20 wt% for Matrimid and from 0 - 40 wt% for PIM-1.

The molecular mobility of Matrimid, PIM-1 and of both nanocomposite systems were investigated by Broadband Dielectric Spectroscopy (BDS). Pure Matrimid and PIM-1 displayed one broad relaxation process, denoted as β^* -relaxation, and a conductivity contribution. For both polymers the relaxation process occurred at higher temperatures as it is expected for solely β -processes. Furthermore, the activation energies for this β^* -relaxation ($E_{A,\beta^*,Matrimid} = 99$ kJ/mol, $E_{A,\beta^*,PIM-1} = 86$ kJ/mol) are relatively high compared to β -processes of comparable glassy polymers (40 - 60 kJ/mol). Concluding the specific β^* -relaxation and high activation energies observed for Matrimid and PIM-1, the β^* -relaxation has to be of cooperative nature.

It was assumed that the cooperative relaxation is caused by agglomerates which are formed by $\pi - \pi$ -stacking of the phenyl rings of Matrimid (or PIM-1).

The assumption of such agglomerates were evidenced by preliminary wide-angle X-ray (WAXS) measurements of Matrimid and PIM-1 (Fig. 7.1). The measurements showed several broad reflections with spacings of 3.2 and 5.3 Å for Matrimid and 3.4 and 10 Å for PIM-1 while 10 Å can be attributed to the micropores.

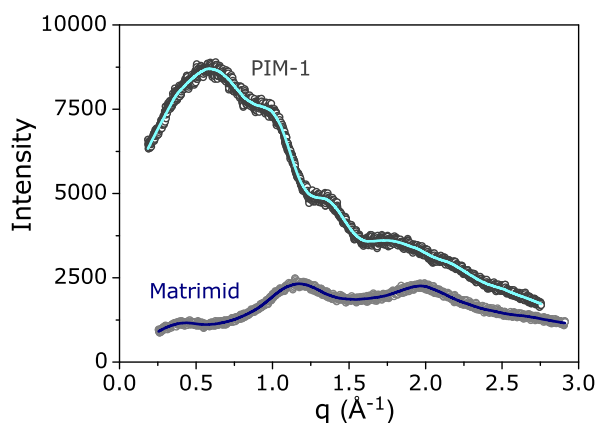


Figure 7.1 – X-ray curve of the freshly cast Matrimid and PIM-1 films.

Furthermore, dynamic mechanical properties of Matrimid were determined using Dynamic Mechanical Analysis (DMA). Performing DMA on PIM-1 film was not possible because of the brittleness of the film which broke during measurement. For Matrimid, basically, the same processes as for BDS were observed with DMA. At higher temperatures an α -relaxation, the dynamic glass transition, and at lower temperatures a β^* -relaxation was found for the loss modulus. In addition, the dynamic-mechanic and the dielectric properties showed that the β^* -relaxation consists of two processes, merging together either with increasing frequency (DMA) or temperature (BDS). Combined with the results of two spacings measured by WAXS, the separation of the β^* -relaxation into two processes was explained by the existence of different agglomerates.

A conductivity contribution well below the glass transition temperature was observed for Matrimid and PIM-1. The temperature dependence was Arrhenius like, which is untypical for conventional amorphous polymers, where the Vogel-Fulcher-Tammann equation describes the temperature dependence well. The estimated activation energies are $E_{A,\sigma_{DC},\text{Matrimid}} = 115$ kJ/mol and $E_{A,\sigma_{DC},\text{PIM-1}} = 101$ kJ/mol. Therefore,

and with the results of the WAXS measurements and the β^* -relaxation, the observed conductivity was ascribed to the $\pi - \pi$ -stacking, which enhances charge transport.

For Matrimid/PhE-POSS and PIM-1/PhE-POSS composites a β^* -relaxation as well as a conductivity contribution were found with BDS. For Matrimid/PhE-POSS at a POSS concentration of about 4 wt% and for PIM-1/PhE-POSS of about 10 wt% an additional peak at lower temperature appeared. It was concluded that this observed peak belongs to the α -relaxation of pure PhE-POSS, which takes place in the same temperature range and thus, a phase separated structure above the respective POSS concentration was assumed for both composites.

Additionally, this assumed phase separated structure was further supported by a Maxwell-Wagner-Sillars polarization, which was clearly visible for the Matrimid composites and only slightly present for the PIM-1 composites.

An overview of the main results for Matrimid and PIM-1 as well as their PhE-POSS composites are listed in Table 7.1.

Table 7.1 – Pure Matrimid and pure PIM-1 measurement results overview.

Polymer	T_g	ρ	Thickness	E_{A,β^*}	$E_{A,\sigma_{DC}}$	Spacings	c_{crit}
	$^{\circ}\text{C}$	g cm^{-3}	μm	kJ/mol	kJ/mol	\AA	wt%
Matrimid	320	1.24	91	99	115	3.2/5.3	4
PIM-1	-	1.15	217	86	101	3.4	10

In general, Matrimid and PIM-1 have shown similar results regarding their internal molecular mobility. Due to their π -systems, both polymers form sandwich like structures by $\pi - \pi$ -stacking. However, the activation energies for the motion of the formed agglomerates are slightly different, 99 kJ/mol for Matrimid and 86 kJ/mol for PIM-1. This is attributed to a higher free volume in PIM-1, which is formed due to the rigid structure (see Figure 7.2), leading to a slightly enhanced mobility of the agglomerates compared to Matrimid. One interesting aspect is that the difference of E_{A,β^*} and $E_{A,\sigma_{DC}}$ for Matrimid and PIM-1 is about 15 kJ/mol, which might be accidentally but should be further investigated.

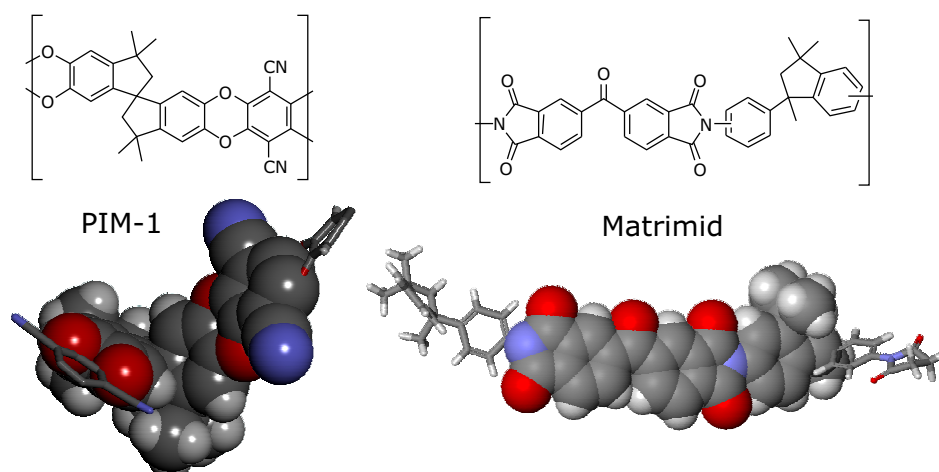


Figure 7.2 – Structures of Matrimid and PIM-1.

After the incorporation of PhenethylPOSS into Matrimid and PIM-1, the difference of the amount of free volume is still present. The composites of Matrimid and PIM-1 differ strongly with respect to their optical transparency for high POSS concentrations (see Fig. 7.3).

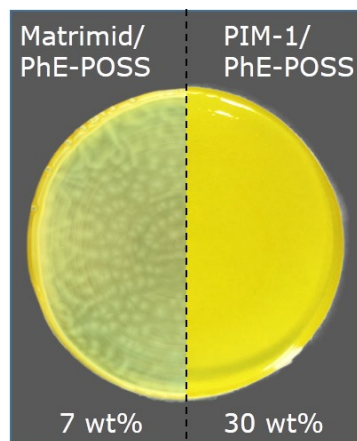


Figure 7.3 – Images of cast Matrimid/PhE-POSS (7 wt%) and PIM-1/PhE-POSS (30 wt%).

With increasing POSS concentration, the Matrimid composites became less transparent and for high POSS concentrations small areas of high cloudiness were formed. In contrast, the PIM-1 composites were transparent even at high POSS concentrations. It was concluded that the maximum size of the POSS domains in the phase-separated structure, has to be about 200 nm because the domains must be smaller than half

of the wave length of visible light. This assumption was further supported by SEM images of the fracture edge of the Matrimid and PIM-1 composites. Cavities on the surface of the fracture edge were observed for both composites at high POSS concentrations which were attributed to broken out POSS agglomerates. For Matrimid composites cavities appear with concentrations higher than 4 wt%, whereas for PIM-1 the concentration must be higher than 30 wt%.

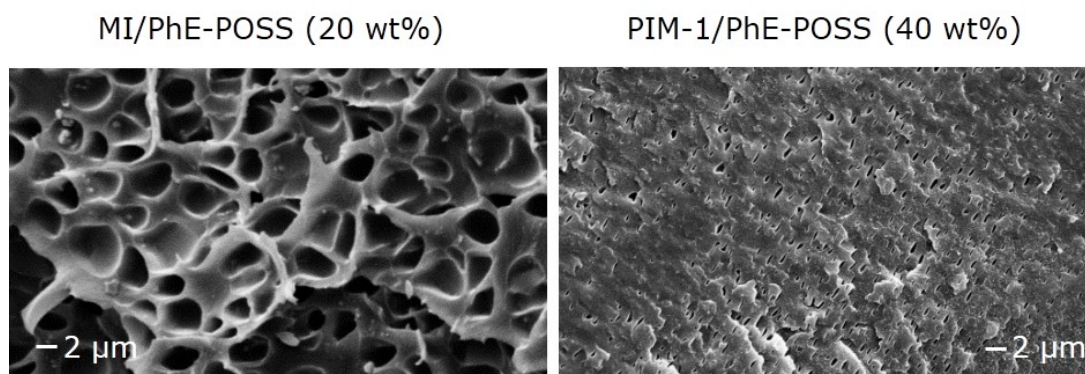


Figure 7.4 – SEM images of fracture edge of Matrimid and PIM-1 composites with POSS concentrations of 20 wt% and 40 wt%.

In Figure 7.4 the fracture edges of Matrimid and PIM-1 composites are shown, each with the maximum investigated concentration of POSS. The size of the observed cavities in Matrimid strongly differs from the cavities in PIM-1 composites. The POSS agglomerates formed in PIM-1 are much smaller than the POSS agglomerates formed in the Matrimid composites. This result is in line with the BDS results for the PIM-1/PhE-POSS composites where no pronounced Maxwell/Wagner/Sillars (MWS) polarization effects was observed, however, Matrimid/PhE-POSS composites showed pronounced MWS phenomena.

Besides the smaller size of the POSS domains in PIM-1 compared to Matrimid, the rigidity is strongly different, indicated by the difference in brittleness of fresh cast films. Furthermore, the concentration dependence of the normalized density is an additional indication for a more rigid structure of PIM-1 compared to Matrimid (Figure 7.5).

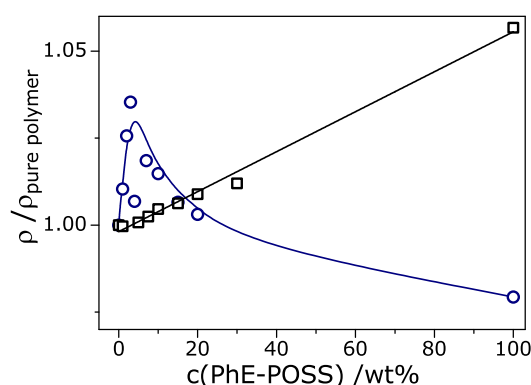


Figure 7.5 – Normalized density of Matrimid (circles) and PIM-1 (squares) composites vs. PhE-POSS concentration.

For both polymers it was assumed that small amounts of POSS are dissolved in the free volume sites of the polymer matrix. For small POSS concentrations, the density of Matrimid and PIM-1 composites increases, supporting the assumption of the filling of the free volume sites. When the phase separation occurs and POSS agglomerates are formed, ρ of the Matrimid composites decreases towards the ideal two phase behavior. In contrast, ρ of the PIM-1 composites starts to deviate from the ideal two phase behavior. This was assigned to two competitive processes. Besides the filling of the free volume sites, the formation of POSS agglomerates starts to distort the internal structure while the free volume is further filled up.

Furthermore, gas transport experiments showed strong interactions of the POSS molecules with the surrounding polymer matrix. The permeability of PIM-1 and Matrimid was enhanced by only 1 wt% of POSS embedded in polymers. In case of PIM-1 this enhancement indicated a substantial improvement of the membrane performance as the selectivity/permeability was improved towards the Robeson upper bound. Unfortunately, pronounced trend to physical aging prevents a direct utilization of these improvements.

In addition, the interaction of the POSS agglomerates with the Matrimid matrix, in the phase separated structure, led to a reduced plasticization effect for CO_2 .

In conclusion, this work proves the existence of agglomerates formed by $\pi - \pi$ -stacking in Matrimid and in PIM-1. Up to the present this fact was not taken into account when film formation, free volume, chain dynamics and especially gas transport properties were discussed. The expected interaction of the phenyl ring of the substituents of POSS with the π -system of the polymers was proved. However,

this strong interaction either leads to significant improvements for small POSS concentrations (especially for PIM-1) or reduces plasticization (for Matrimid) for high POSS contents.

7.2 Outlook

In general, the observed $\pi - \pi$ interactions provide a high potential on the one hand for the stabilization of the polymer itself and on the other hand for a better interaction between polymer and filler in a mixed matrix membrane and thus, improve gas transport properties and/or reduce plasticization effects. Due to the indicated physical aging effect observed for 1 wt% of POSS in PIM-1, another additional stabilization has to be found, e.g. additional crosslinking. Nevertheless, the discussed findings in this study have to be further investigated and extended to more PIMs as well as nanofillers.

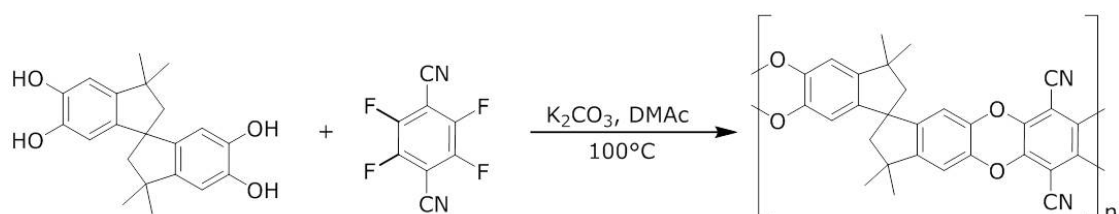
A Further Experimental Details

A.1 Materials and Sample Preparation: PIM-1*

Material

Synthesis

The synthesis of PIM-1 was carried out according to the procedure below, based on that reported by Du et al.¹¹⁷



To a dry 500 ml three-necked round bottom flask equipped with a Dean-Stark trap, 5,5',6,6'-tetrahydroxy-3,3,3',3'-tetramethyl-1,1'-spirobisindane (TTSBI) (17.021 g, 0.05 mol), tetrafluoroterephthalonitrile (TFTP) (10.005 g, 0.05 mol), anhydrous potassium carbonate (20.730 g, 0.15 mol), dimethylacetamide DMAc (100 ml), and toluene (50 ml) were added under an atmosphere of nitrogen gas. The monomers were allowed to dissolve before the reaction mixture was refluxed during rapid stirring at 200 rpm at 160 °C for 40 min. Heating was carried out using a IKA hot-plate together with a DrySyn aluminium heating block. After 40 min, the viscous solution was poured into methanol. To purify the polymer, the sample was dissolved in 500 ml of chloroform and re-precipitated in methanol while stirring. After washing with

*Similar content was published in Konnertz, N.; Ding, Y.; Harrison, W. J.; Budd, P. M.; Schönhals, A.; Böhning, M., *ACS Macro Letters*, 2016, 5, 528-532; Supporting Information.

acetone, the product was stirred in 1,4-dioxane for 30 min to remove low molecular weight oligomers and cyclic products, before washing again with acetone. The sample was then refluxed overnight in deionized water, stirred in methanol for 20 min and then dried at 100 °C for two days. The final yield of PIM-1 obtained was 22.06 g (95.9 %).

It has to be noted that for PIM-1 very different casting/ drying protocols can be found in the literature, which lead to different states of the solid film (as revealed, e.g., by different gas permeabilities). Drying temperatures in the range from 40 °C up to 100 °C have been reported^{20,153,155} the strong tendency to physical aging of PIMs suggests as low as possible temperatures as long as complete solvent removal is ensured. Furthermore, it is known that a methanol treatment for solvent exchange results in lower packing density (and high gas permeabilities), while contact with water (e.g., for removing the film from the casting plate) has an opposite effect.

Characterization

Gel Permeation Chromatography (GPC)

Gel Permeation Chromatography (GPC) measurements were carried out using a Viscotek GPC max VE 2001 instrument with two PL mixed B columns and a Viscotek TDA 302 Triple Detector Array which employs a viscometer, refractive index and light scattering detectors. Chloroform was used as solvent at a flow rate of 1 cm³ min⁻¹ and the injection volume was 100 µl. A PIM-1 solution in filtered chloroform was used at a concentration of 1.00 mg/ml. A calibration curve constructed from polystyrene standards of known molar mass was used to calculate a comparative value of molar mass from the refractive index detector. For light scattering, a refractive index increment value for PIM-1 in chloroform of 0.196 g/ml was used in the calculation of molar mass. An absolute value of molar mass and polydispersity of the PIM-1 was then calculated using data from all three detectors. The results are listed in table A.1.

Table A.1 – Results from Gel Permeation Chromatography of PIM-1.

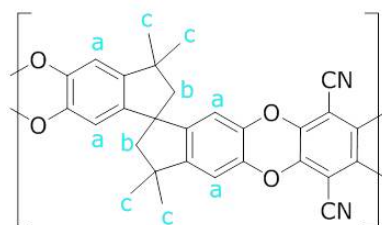
Polymer	M_W	M_n	M_W/M_n	M_p
PIM-1	82800	29300	2.8	55900

SEC in chloroform against polystyrene standards gave $M_W = 82800$ g/mol and a polydispersity index of $PDI = 2.8$.

^1H Nuclear Magnetic Resonance (NMR)

^1H Nuclear Magnetic Resonance (NMR) spectroscopy was carried out using a Bruker 400 MHz spectrometer. For sample preparation, PIM-1 was dissolved in deuterated chloroform (CDCl_3 , Aldrich 99.8% atom D) to make a concentrated solution which was then transferred into a 5 mm NMR tube. Results from ^1H -NMR can be found in Figure A.1.

The typical peaks attributed to PIM-1 can be seen in the ^1H -NMR spectra:



a – aromatic hydrogens, peaks 6.36 and 6.74 ppm

b – hydrogens on the five membered ring, peaks 2.1 and 2.26 ppm

c – hydrogens from methyl groups, peaks 1.24 and 1.29 ppm

Additional peak suggesting presence of residual solvent: Peak at 3.63 ppm– attributed to 1,4-dioxane. This was used to purify the polymer by removing oligomers/ cyclic PIM-1 species.

The ^1H -Nuclear Magnetic Resonance spectra are shown below in Figure A.1 and A.2.

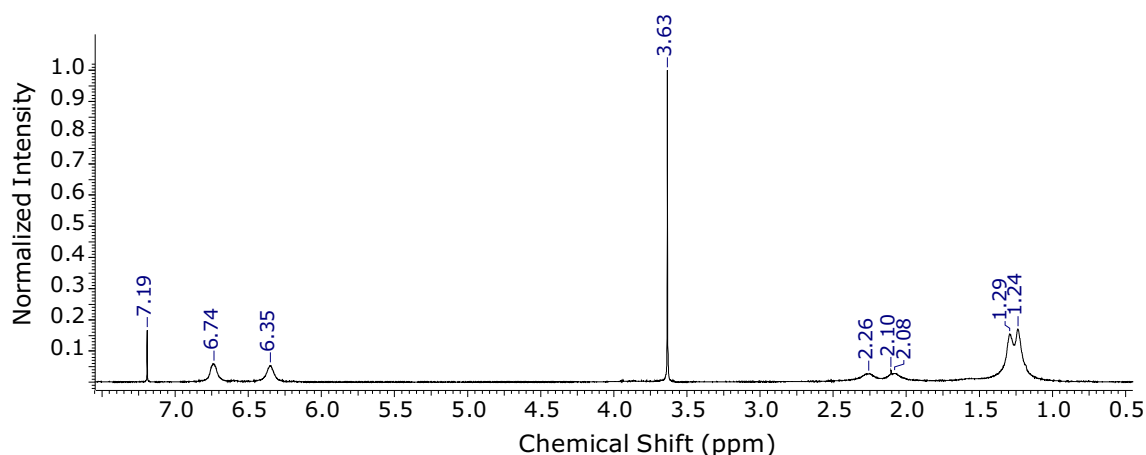


Figure A.1 – ^1H -NMR of PIM-1 before washing with methanol.

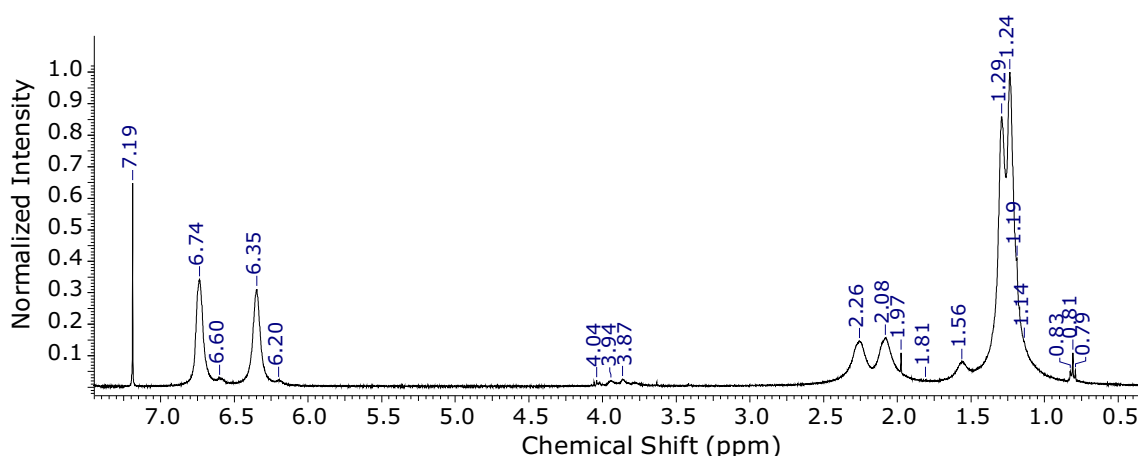


Figure A.2 – ^1H - NMR after washing with methanol – the 1,4-dioxane peak at 3.63 ppm is no longer visible.

Sample Preparation

Thermogravimetric Analysis

In order to obtain a representative PIM-1-film, a protocol without methanol treatment and without direct water contact was chosen. An optimal annealing temperature was determined by several casting/drying steps (temperature, time) with subsequent thermogravimetric analysis (TGA), respectively. After drying for 1 day in vacuum at 40 °C in the TGA, a remaining mass loss of about 2.6% at 200 °C was observed, which after 5 days at 40 °C was still 1.3%. For the second series of films, temperatures

above the boiling point of the solvent used (chloroform, bp = 61 °C) were chosen: 75 and 100 °C. After 3 days, at 75 °C there was a mass loss at 200 °C of 0.44% in the TGA, which was the same as for 1 day at 100 °C. After 3 days at 100 °C only a further reduction to 0.33% was achieved. Therefore, 3 days at 75 °C was chosen for the film used in this study. Selected TGA curves are given in Figure A.3.

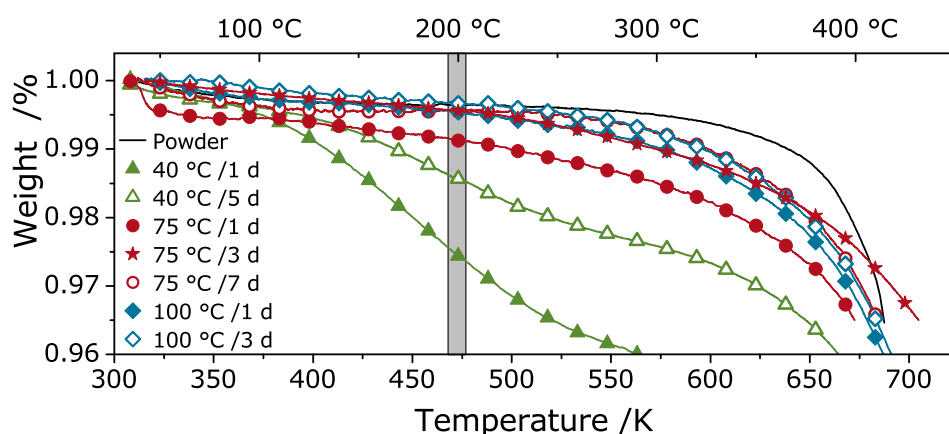


Figure A.3 – Selected TGA curves of PIM-1 films after the indicated drying/annealing protocols.

A.2 Dielectric Investigations: PIM-1 and Matrimid

X-Ray Measurements

A SAXSess mc2 small angle scattering system (Anton Paar, Graz, Austria) operated in wide angle modus was applied for X-ray measurements. Line-collimation operational mode and Cu-K α -radiation ($\lambda = 0.154$ nm) were used. The polymer samples were placed between two small copper plates and mounted to a solid sample holder in an evacuated sample chamber (1 mbar). The illuminated area was 20 mm x 1 mm. Data were recorded with an imaging plate and an exposition time of 15 min at constant temperature of 20 °C. The OptiQuant Image Analysis Software (Perkin Elmer) was utilized to read out the imaging plate and subsequent, treated with the SAXS Quant Software (Anton Paar).

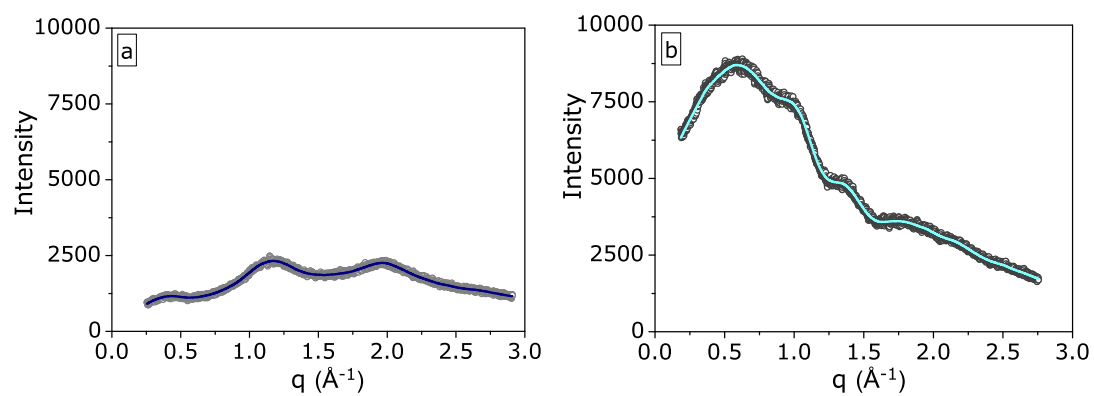


Figure A.4 – X-ray curves of the freshly cast Matrimid (a) and PIM-1 (b) film.

B Abbreviations

A	a	factor with unit $(rad \cdot s^{-1})^{s-1}$
	A	fragility parameter
	α	thermal expansion coefficient
	α_s	thermal expansion coefficient of a solid
	α_l	thermal expansion coefficient of a liquid
	$\alpha_{i,j}^{id}$	ideal selectivity
B	b	affinity constant
	BDS	Broadband Dielectric Spectroscopy
C	c	concentration
	C*	complex capacitance
	C ₀	vacuum capacitance
	c ₁	concentration upstream
	c ₂	concentration downstream
	c _D	concentration of the penetrant in the polymer
	c _H	Langmuir sorption
	c' _H	saturation capacity
	c _p	specific heat
	CRR	Cooperatively Rearranging Regions
D	D	diffusion coefficient
	D _{diel}	dielectric displacement
	D _{diel.,0}	dielectric displacement of the free space
	D _{eff}	effective diffusion coefficient
	D*	complex strain compliance
	D'	real part of the complex strain compliance
	D''	imaginary part of the complex strain compliance
	DC	direct current
	DMA	Dynamic Mechanical Analysis
	DSC	Differential Scanning Calorimetry

B ABBREVIATIONS

E	E	electric field
	E^*	complex elastic modulus
	E'	storage modulus
	E''	loss modulus
	ΔE	free energy barrier for one molecule or segments
	$\Delta \epsilon$	dielectric strength
	$E_{A,D}$	activation energy of the diffusion
	E_{A,β^*}	activation energy of the β^* -relaxation
	$E_{A,cond}$	activation energy of the conductivity
	E_0	alternating electric field amplitude
	$E(t)$	outer electrical field
	ϵ	permittivity
	ϵ^*	complex dielectric function
	ϵ'	real part of ϵ^*
	ϵ''	imaginary part of ϵ^*
	ϵ_0	dielectric permittivity of vacuum ($8.854 \times 10^{-12} \text{ As V}^{-1} \text{ m}^{-1}$)
	ϵ_s	static permittivity
	ϵ_∞	unrelaxed permittivity
	$\epsilon(t)$	time dependent dielectric function
F	f	frequency
	f_c	characteristic frequency
	f_g	fractional free volume at T_g
	f_{max}	relaxation rate
	f_∞	frequency in the high temperature limit
	F	effective sample area
G	G	shear modulus
J	J	molar flux
	J_{st}	molar flux in the steady state
H	ΔH_S	partial molar enthalpy of the sorption
	HN	Havriliak Negami
K	k_B	Boltzmann constant ($1.38 \cdot 10^{-23} \text{ J/K}$)
	k_D	Henry-constant
L	l	membrane thickness
	λ	mean free path
M	M_W	molecular weight
	M_c	critical molecular weight

B ABBREVIATIONS

	MWS	Maxwell-Wagner-Sillars
N	N	total number of particles
P	p	pressure
	p_1	pressure upstream
	p_2	pressure downstream
	P	permeability coefficient
	\hat{P}	polarization
	\hat{P}_∞	contributions arising from induced polarization
	p_i	microscopic dipole moments
	Φ_{FV}	fractional free volume
Q	Q_t	total amount of permeated gas
R	R	universal gas constant ($8.314 \text{ J mol}^{-1} \text{ K}^{-1}$)
	ρ	density
S	s	parameter describing ohmic and non-ohmic effects
	S	solubility coefficient
	S_c	total configurational entropy
	σ^*	complex conductivity
	σ'	real part of σ^*
	σ''	imaginary part of σ^*
	σ_0	DC (direct current) conductivity
	σ_{DC}	DC (direct current) conductivity
	σ_{kin}	kinetic diameter
	ST	steady state
	STP	standard conditions $T_{STP} = 273.15 \text{ K}$ and $p_{STP} = 1.013 \text{ bar}$
	SEM	Scanning Electron Microscopy
T	t	time
	τ	relaxation time
	τ_∞	relaxation time in the high temperature limit
	τ_{TL}	time-lag
	T	temperature
	T_0	Vogel or ideal glass transition temperature
	T_c	critical temperature
	T_g	glass transition temperature
	T_K	Kautzmann temperature
	T_m	melting temperature
	TGA	Thermogravimetric Analysis

B ABBREVIATIONS

	TL	time lag
V	V	volume
	V^*	minimal free volume required for a jump of a segment (or molecule) between two sites
	V_c	critical volume
	V_{gas}^0	volume of a gas at standard conditions STP
	$V_{m,gas}^0$	molar volume for an ideal gas ($22.4 \text{ cm}^3 \text{ mol}^{-1}$)
	V_{free}	total free volume
	\overline{V}_{free}	average free volume
	V_l	volume of an undercooled liquid
	V_M	volume of molecule ($V_M \approx V_{vdW}$)
	V_{Matrix}	matrix volume
	V_{spec}	specific volume
	V_{vdW}	van der Waals volume
	V_{CRR}	volume of "Cooperatively Rearranging Regions (CRR)"
	VFT	Vogel-Fulcher-Tammann
W	ω	angular frequency
X	x	space coordinate measured normal to the section
	χ^*	dielectric susceptibility
	ξ	length
Z	Z^*	complex impedance
	$z(T)$	number of segments per CRR

C Publications

C.1 Paper

Related Work

1. N. Konnertz, M. Böhning and A. Schönhals, Dielectric investigations of nanocomposites based on matrimid and polyhedral oligomeric phenethyl-silsesquioxanes (POSS), *Polymer*, 2016, **90**, 89-101.
2. N. Konnertz, Y. Ding, W. J. Harrison, P.M. Budd, A. Schönhals, M. Böhning, Molecular mobility of the high performance membrane polymer PIM-1 as investigated by dielectric spectroscopy, *ACS Macro Letters*, 2016, **5**, 528-532.
3. N. Konnertz, Y. Ding, W. J. Harrison, P.M. Budd, A. Schönhals, M. Böhning, Molecular Mobility and Gas Transport Properties of Nanocomposites based on PIM-1 and Polyhedral Oligomeric Phenethyl-Silsesquioxanes (POSS), *Journal of Membrane Science*, 2017, **529**, 274-285.

Other Publications

4. D. Becker, N. Konnertz, M. Böhning, J. Schmidt, A. Thomas, Light-Switchable Polymers of Intrinsic Microporosity, *Chemistry of Materials*, 2016, **28**, 8523-8529.

C.2 Contributions to Conferences

C.2.1 Oral Presentations

1. N. Konnertz, A. Schönhals and M. Böhning, Gas Transport Properties and Molecular Mobility of Matrimid/PhenethylPOSS Nanocomposites, 15th Network Young Membranes, Aachen, September 2015.
2. N. Konnertz, A. Schönhals and M. Böhning, Gas Transport Properties and Molecular Mobility of Matrimid/PhenethylPOSS Nanocomposites, EUROMEMBRANE, Aachen, September 2015.
3. N. Konnertz, M. Böhning and A. Schönhals, Dielectric Investigations of the high Performance Polymer PIM-1 and Nanocomposites containing PhenethylPOSS, 9th International Conference on Broadband Dielectric Spectroscopy and its Applications, Pisa, Italy, September 2016.

C.2.2 Poster Presentations

1. N. Konnertz, M. Böhning and A. Schönhals, Gas Transport Properties and Molecular Mobility of Matrimid/PhenethylPOSS Nanocomposites, DPG Frühjahrstagung, Berlin, March 2015.
2. N. Konnertz and M. Böhning, QCM System for the Characterization of Gas Sorption and Physical Aging on Membrane Polymers and Nanocomposites for Gas Separation Applications, DPG Frühjahrstagung, Berlin, March 2015.
3. N. Konnertz and M. Böhning, QCM System for the Characterization of Gas Sorption and Physical Aging on Membrane Polymers and Nanocomposites for Gas Separation Applications, EUROMEMBRANE, Aachen, September 2015.

D Bibliography

- [1] R. W. Baker, *Industrial & Engineering Chemistry Research*, 2002, **41**, 1393–1411.
- [2] R. W. Baker, *Membrane technology and applications*, John Wiley & Sons, Chichester, 2004.
- [3] D. J. Stookey, C. J. Patton, and G. L. Malcolm, *Chemical Engineering Progress*, 1986, **82**, 36–40.
- [4] http://www.mtrinc.com/pdf_print/refinery_and_syngas/MTR_Brochure_Hydrogen_Purification.pdf, 2016.
- [5] R. Prasad, R. L. Shaner, and K. J. Doshi in *Polymeric Gas Separation Membranes*, ed. D. R. Paul and Y. P. Yampolskii; CRC Press, Inc., Boca Raton, Florida, 1994.
- [6] D. F. Sanders, Z. P. Smith, R. Guo, L. Robeson, J. E. McGrath, D. R. Paul, and B. D. Freeman, *Polymer*, 2013, **54**, 4729–4761.
- [7] D. L. Gin and R. D. Noble, *Science*, 2011, **332**, 674–676.
- [8] W. J. Koros and G. K. Fleming, *Journal of Membrane Science*, 1993, **83**, 1–80.
- [9] H. K. Lonsdale, *Journal of Membrane Science*, 1982, **10**, 81–181.
- [10] S. A. Stern, *Journal of Membrane Science*, 1994, **94**, 1–65.
- [11] L. M. Robeson, *Journal of Membrane Science*, 1991, **62**, 165–185.
- [12] L. M. Robeson, *Journal of Membrane Science*, 2008, **320**, 390–400.
- [13] O. M. Ekiner and R. A. Hayes, Phenylindane-containing polyimide gas separation membranes, 1991.

- [14] J. W. Simmons and O. M. Ekiner, Polyimide and polyamide-imide gas separation membranes , 1993.
- [15] A. Bos, I. G. M. Pünt, M. Wessling, and H. Strathmann, *Separation and Purification Technology*, 1998, **14**, 27–39.
- [16] P. M. Budd, B. S. Ghanem, S. Makhseed, N. B. McKeown, K. J. Msayib, and C. E. Tattershall, *Chemical Communications*, 2004, pp. 230–231.
- [17] P. M. Budd, K. J. Msayib, C. E. Tattershall, B. S. Ghanem, K. J. Reynolds, N. B. McKeown, and D. Fritsch, *Journal of Membrane Science*, 2005, **251**, 263–269.
- [18] R. Swaidan, B. Ghanem, and I. Pinnau, *ACS Macro Letters*, 2015, **4**, 947–951.
- [19] Y. Yampolskii, *Macromolecules*, 2012, **45**, 3298–3311.
- [20] C. H. Lau, P. T. Nguyen, M. R. Hill, A. W. Thornton, K. Konstas, C. M. Doherty, R. J. Mulder, L. Bourgeois, A. C. Y. Liu, D. J. Sprouster, J. P. Sullivan, T. J. Bastow, A. J. Hill, D. L. Gin, and R. D. Noble, *Angewandte Chemie*, 2014, **53**, 5322–5326.
- [21] S. Harms, K. Rätzke, F. Faupel, N. Chaukura, P. M. Budd, W. Egger, and L. Ravelli, *Journal of Adhesion*, 2012, **88**, 608–619.
- [22] W. F. Yong, K. H. A. Kwek, K. S. Liao, and T. S. Chung, *Polymer*, 2015, **77**, 377–386.
- [23] L. Olivieri, S. Ligi, M. G. De Angelis, G. Cucca, and A. Pettinau, *Industrial & Engineering Chemistry Research*, 2015, **54**, 11199–11211.
- [24] K. Althumayri, W. J. Harrison, Y. Y. Shin, J. M. Gardiner, C. Casiraghi, P. M. Budd, P. Bernardo, G. Clarizia, and J. C. Jansen, *Philosophical Transactions of the Royal Society A-Mathematical Physical and Engineering Sciences*, 2016, **374**.
- [25] S. Kanehashi, G. Q. Chen, C. A. Scholes, B. Ozcelik, C. Hua, L. Ciddor, P. D. Southon, D. M. D'Alessandro, and S. E. Kentish, *Journal of Membrane Science*, 2015, **482**, 49–55.
- [26] L. Ge, W. Zhou, V. Rudolph, and Z. H. Zhu, *Journal of Materials Chemistry A*, 2013, **1**, 6350–6358.

- [27] A. E. Amooghin, M. Omidkhah, and A. Kargari, *RSC Advances*, 2015, **5**, 8552–8565.
- [28] J. Ahmad and M. B. Hagg, *Separation and Purification Technology*, 2013, **115**, 190–197.
- [29] Q. L. Song, S. K. Nataraj, M. V. Roussanova, J. C. Tan, D. J. Hughes, W. Li, P. Bourgoïn, M. A. Alam, A. K. Cheetham, S. A. Al-Muhtaseb, and E. Sivaniah, *Energy & Environmental Science*, 2012, **5**, 8359–8369.
- [30] B. Zornoza, C. Tellez, and J. Coronas, *Journal of Membrane Science*, 2011, **368**, 100–109.
- [31] S. Kim, E. Marand, J. Ida, and V. V. Guliants, *Chemistry of Materials*, 2006, **18**, 1149–1155.
- [32] K. N. Raftopoulos, S. Koutsoumpis, M. Jancia, J. P. Lewicki, K. Kyriakos, H. E. Mason, S. J. Harley, E. Hebda, C. M. Papadakis, K. Pielichowski, and P. Pissis, *Macromolecules*, 2015, **48**, 1429–1441.
- [33] K. Tsuchiya, H. Arai, Y. Ishida, and A. Kameyama, *Macromolecules*, 2015, **48**, 1636–1643.
- [34] D. Gnanasekaran, A. Shanavas, W. W. Focke, and R. Sadiku, *RSC Advances*, 2015, **5**, 11272–11283.
- [35] M. M. Rahman, S. Shishatskiy, C. Abetz, P. Georgopoulos, S. Neumann, M. M. Khan, V. Filiz, and V. Abetz, *Journal of Membrane Science*, 2014, **469**, 344–354.
- [36] M. J. T. Raaijmakers, M. Wessling, A. Nijmeijer, and N. E. Benes, *Chemistry of Materials*, 2014, **26**, 3660–3664.
- [37] A. Strachota, K. Rodzen, F. Ribot, M. Trchova, M. Steinhart, L. Starovoytova, and E. Pavlova, *Macromolecules*, 2014, **47**, 4266–4287.
- [38] M. M. Rahman, V. Filiz, M. M. Khan, B. N. Gacal, and V. Abetz, *Reactive & Functional Polymers*, 2015, **86**, 125–133.
- [39] M. M. Rahman, V. Filiz, S. Shishatskiy, C. Abetz, P. Georgopoulos, M. M. Khan, S. Neumann, and V. Abetz, *ACS Applied Materials & Interfaces*, 2015, **7**, 12289–12298.

- [40] A. J. Guenther, K. R. Lamison, L. M. Lubin, T. S. Haddad, and J. M. Mabry, *Industrial & Engineering Chemistry Research*, 2012, **51**, 12282–12293.
- [41] E. Ayandele, B. Sarkar, and P. Alexandridis, *Nanomaterials*, 2012, **2**, 445–475.
- [42] K. N. Raftopoulos, B. Janowski, L. Apekis, P. Pissis, and K. Pielichowski, *Polymer*, 2013, **54**, 2745–2754.
- [43] K. N. Raftopoulos, M. Jancia, D. Aravopoulou, E. Hebda, K. Pielichowski, and P. Pissis, *Macromolecules*, 2013, **46**, 7378–7386.
- [44] A. T. Dibenedetto and D. R. Paul, *Journal of Polymer Science Part A-General Papers*, 1964, **2**, 1001–1015.
- [45] A. Y. Alentiev and Y. P. Yampolskii, *Journal of Membrane Science*, 2002, **206**, 291–306.
- [46] A. A. Gusev, S. Arizzi, U. W. Suter, and D. J. Moll, *Journal of Chemical Physics*, 1993, **99**, 2221–2227.
- [47] D. Hofmann, L. Fritz, J. Ulbrich, C. Schepers, and M. Böhning, *Macromolecular Theory and Simulations*, 2000, **9**, 293–327.
- [48] R. Inoue, T. Kanaya, Y. M. Hu, T. Masuda, K. Nishida, and O. Yamamuro, *Polymer*, 2014, **55**, 182–186.
- [49] M. Böhning, N. Hao, and A. Schönhals, *Journal of Polymer Science Part B-Polymer Physics*, 2013, **51**, 1593–1597.
- [50] T. Visser and M. Wessling, *Macromolecules*, 2007, **40**, 4992–5000.
- [51] L. H. Sperling, *Introduction to Physical Polymer Science*, Wiley-Interscience, New York, 2001.
- [52] M. Heuchel, M. Böhning, O. Hölck, M. R. Siegert, and D. Hofmann, *Journal of Polymer Science Part B-Polymer Physics*, 2006, **44**, 1874–1897.
- [53] P. G. Debenedetti and F. H. Stillinger, *Nature*, 2001, **410**, 259–267.
- [54] E. J. Donth, *The glass transition*, Springer, Berlin, Heidelberg, New York, 2001.

- [55] A. Schönhalz and F. Kremer in *Polymer Science: A Comprehensive Reference*, ed. K. Matyjaszewski and M. Möller; Elsevier BV, Amsterdam, The Netherlands, 2012; pp. 201–226.
- [56] X. R. Wang and W. S. Zhou, *Macromolecules*, 2002, **35**, 6747–6750.
- [57] Y. P. Koh and S. L. Simon, *Journal of Polymer Science Part B-Polymer Physics*, 2008, **46**, 2741–2753.
- [58] J. L. Keddie, R. A. L. Jones, and R. A. Cory, *Europhysics Letters*, 1994, **27**, 59–64.
- [59] Z. Fakhraai and J. A. Forrest, *Physical Review Letters*, 2005, **95**.
- [60] O. Hölck *Gas sorption and swelling in glassy polymers* PhD thesis, TU Berlin, 2008.
- [61] A. Bondi, *Physical Properties of Molecular Crystals, Liquids and Glasses*, Wiley, New York, 1968.
- [62] R. J. Roe, *Methods of X-ray and Neutron Scattering in Polymer Science*, Oxford University Press, New York, 2000.
- [63] F. Kremer and A. Schönhalz, *Broadband Dielectric Spectroscopy*, Springer, Berlin, Germany, 2003.
- [64] G. S. Fulcher, *Journal of the American Ceramic Society*, 1925, **8**, 339–355.
- [65] H. Vogel, *Physikalische Zeitschrift*, 1921, **22**, 645–646.
- [66] G. Tammann and W. Hesse, *Zeitschrift für Anorganische und Allgemeine Chemie*, 1926, **156**.
- [67] C. A. Angell, *Journal of Research of the National Institute of Standards and Technology*, 1997, **102**, 171–185.
- [68] C. A. Angell, *Journal of Non-Crystalline Solids*, 1991, **131**, 13–31.
- [69] G. Adam and J. H. Gibbs, *Journal of Chemical Physics*, 1965, **43**, 139.
- [70] A. K. Doolittle, *Journal of Applied Physics*, 1951, **22**, 1471–1475.
- [71] M. H. Cohen and D. Turnbull, *Journal of Chemical Physics*, 1959, **31**, 1164–1169.

- [72] M. H. Cohen and G. S. Grest, *Physical Review B*, 1979, **20**, 1077–1098.
- [73] E. J. Donth, *Glasübergang*, Akademie Verlag Berlin, Berlin, 1981.
- [74] E. J. Donth, *Relaxation and thermodynamics in polymers, glass transition*, Akademie Verlag Berlin, Berlin, 1992.
- [75] E. Donth, *Journal of Non-Crystalline Solids*, 1982, **53**, 325–330.
- [76] K. Schneider, A. Schönhals, and E. J. Donth, *Acta Polymerica*, 1981.
- [77] E. Donth, H. Huth, and M. Beiner, *Journal of Physics-Condensed Matter*, 2001, **13**, L451–L462.
- [78] E. Donth, *Journal of Physics-Condensed Matter*, 2000, **12**, 10371–10388.
- [79] E. Hempel, G. Hempel, A. Hensel, C. Schick, and E. Donth, *Journal of Physical Chemistry B*, 2000, **104**, 2460–2466.
- [80] M. Beiner, S. Kahle, E. Hempel, K. Schroter, and E. Donth, *Macromolecules*, 1998, **31**, 8973–8980.
- [81] S. Kahle, J. Korus, E. Hempel, R. Unger, S. Horing, K. Schroter, and E. Donth, *Macromolecules*, 1997, **30**, 7214–7223.
- [82] H. Fujita, *Fortschritte der Hochpolymeren Forschung*, 1961, **3**, 1–47.
- [83] M. D. Sefcik, J. Schaefer, F. L. May, D. Raucher, and S. M. Dub, *Journal of Polymer Science Part B-Polymer Physics*, 1983, **21**, 1041–1054.
- [84] W. W. Brandt, *Journal of Physical Chemistry*, 1959, **63**, 1080–1084.
- [85] D. R. Paul and Y. P. Yampolskii, *Polymeric gas separation membranes*, CRC Press, Inc., Boca Raton, Florida, 1994.
- [86] W. F. Yong *Polymers of Intrinsic Microporosity (PIM)- Based Membranes for Gas Separation* PhD thesis, National University of Singapore, 2014.
- [87] W. J. Koros in *Membrane separation systems: Recent developments and future directions*, ed. R. W. Baker, E. L. Cussler, W. Eykamp, W. J. Koros, R. L. Riley, and H. Strathmann; William Andrew Publishing/Noyes, United States of America, 1991; pp. 189–241.
- [88] A. Eisenberg and J.-S. Kim, *Introduction to Ionomers*, Wiley, New York, 1998.

- [89] J. Crank in *The Mathematics of Diffusion*, ed. J. Crank; Oxford University Press, Oxford, 1975.
- [90] D. R. Paul, *Berichte Der Bunsen-Gesellschaft-Physical Chemistry Chemical Physics*, 1979, **83**, 294–302.
- [91] G. K. Fleming and W. J. Koros, *Macromolecules*, 1986, **19**, 2285–2291.
- [92] J. H. Petropoulos in *Polymeric Gas Separation Membranes*, ed. D. R. Paul and Y. P. Yampolskii; CRC Press, Boca Raton, FL, 1994.
- [93] D. W. Breck, *Zeolite Molecular Sieves: Structure, Chemistry and Use*, Wiley, New York, 1974.
- [94] A. R. Berens and H. B. Hopfenberg, *Journal of Membrane Science*, 1982, **10**, 283–303.
- [95] L. M. Robeson, W. F. Burgoyne, M. Langsam, A. C. Savoca, and C. F. Tien, *Polymer*, 1994, **35**, 4970–4978.
- [96] <https://www.membrane-australasia.org/polymer-gas-separation-membranes/>, 2016.
- [97] R. E. Kesting and A. K. Fritzsche, *Polymeric gas separation membranes*, John Wiley & Sons, New York, NY, USA, 1993.
- [98] B. W. Rowe, B. D. Freeman, and D. R. Paul in *Membrane engineering for the treatment of gases. Gas-separation problems with membranes*, ed. E. Drioli and G. Barbieri; Royal Society of Chemistry, 2011.
- [99] L. C. E. Struik, *Physical aging in amorphous polymers and other materials*, Elsevier, Amsterdam, The Netherlands, 1978.
- [100] A. Schönhalz in *Dielectric Spectroscopy of Polymeric Materials*, ed. J. P. Runt and J. Fitzgerald; American Chemical Society Publication, 1999.
- [101] M. Üzümlü *Metal/Polymer Hybrids: Multiscale Adhesion Behaviour and Polymer Dynamics* PhD thesis, TU Berlin, 2015.
- [102] K. W. Wagner, *Arch. Elektrotech. (Berlin)*, 1914, **2**, 371–387.
- [103] R. Sillars, *J. Inst. Elect. Eng.*, 1937, **12**, 139–155.

- [104] C. Böttcher and P. Bordewijk in *Dielectrics in time-dependent fields*; Elsevier, Amsterdam, Oxford, New York, 1978.
- [105] L. Landau and E. Lifschitz in *Statistical physics*; Akademie Verlag Berlin, Berlin, 1979.
- [106] P. Debye, *Polar Molecules*, Chemical Catalog Co., Inc, New York, 1929.
- [107] K. S. Cole and R. H. Cole, *Journal of Chemical Physics*, 1941, **9**, 341–351.
- [108] S. Havriliak and S. Negami, *Journal of Polymer Science Part C-Polymer Symposium*, 1966, pp. 99–117.
- [109] S. Havriliak and S. Negami, *Polymer*, 1967, **8**, 161–210.
- [110] A. Boersma, J. van Turnhout, and M. Wübberhorst, *Macromolecules*, 1998, **31**, 7461–7466.
- [111] F. Kremer and A. Schönhals in *Broadband Dielectric Spectroscopy*, ed. F. Kremer and A. Schönhals; Springer, Berlin, Germany, 2003; p. 35.
- [112] E. Schlosser and A. Schönhals, *Colloid and Polymer Science*, 1989, **267**, 963–969.
- [113] J. C. Dyre, *Journal of Applied Physics*, 1988, **64**, 2456–2468.
- [114] A. K. Jonscher, *Nature*, 1977, **267**, 673–679.
- [115] N. Hao, M. Böhning, and A. Schönhals, *Macromolecules*, 2010, **43**, 9417–9425.
- [116] B. D. Freeman in *Springer Handbook of Materials Measurement Methods*, ed. H. Czichos, T. Saito, and L. M. Smith; Springer, Heidelberg, 2006.
- [117] N. Y. Du, G. P. Robertson, J. S. Song, I. Pinnau, S. Thomas, and M. D. Guiver, *Macromolecules*, 2008, **41**, 9656–9662.
- [118] N. Hao, M. Böhning, and A. Schönhals, *Macromolecules*, 2007, **40**, 9672–9679.
- [119] N. Hao, M. Böhning, H. Goering, and A. Schönhals, *Macromolecules*, 2007, **40**, 2955–2964.
- [120] E. Rikowski and H. C. Marsmann, *Polyhedron*, 1997, **16**, 3357–3361.

- [121] A. R. Bassindale, H. P. Chen, Z. H. Liu, L. A. MacKinnon, D. J. Parker, P. G. Taylor, Y. X. Yang, M. E. Light, P. N. Horton, and M. B. Hursthouse, *Journal of Organometallic Chemistry*, 2004, **689**, 3287–3300.
- [122] M. Sanchez-Soto, D. A. Schiraldi, and S. Illescas, *European Polymer Journal*, 2009, **45**, 341–352.
- [123] Y. Wu, L. G. Li, S. Y. Feng, and H. Z. Liu, *Polymer Bulletin*, 2013, **70**, 3261–3277.
- [124] Y. Li, T. S. Chung, C. Cao, and S. Kulprathipanja, *Journal of Membrane Science*, 2005, **260**, 45–55.
- [125] F. Y. Li, Y. Li, T. S. Chung, and S. Kawi, *Journal of Membrane Science*, 2010, **356**, 14–21.
- [126] A. C. Comer, D. S. Kalika, B. W. Rowe, B. D. Freeman, and D. R. Paul, *Polymer*, 2009, **50**, 891–897.
- [127] H. W. Starkweather, *Macromolecules*, 1981, **14**, 1277–1281.
- [128] J. P. Bellomo and T. Lebey, *Journal of Physics D-Applied Physics*, 1996, **29**, 2052–2056.
- [129] L. Hardy, I. Stevenson, G. Boiteux, G. Seytre, and A. Schönhals, *Polymer*, 2001, **42**, 5679–5687.
- [130] M. Wübbenhorst, A. L. de Rooij, J. van Turnhout, J. Tacx, and V. Mathot, *Colloid and Polymer Science*, 2001, **279**, 525–531.
- [131] C. Spies and R. Gehrke, *Macromolecules*, 1997, **30**, 1701–1710.
- [132] A. S. Jones, T. J. Dickson, B. E. Wilson, and J. Duhamel, *Macromolecules*, 1999, **32**, 2956–2961.
- [133] S. Wellert, *TU Berlin, Personal communication*.
- [134] N. G. McCrum, B. E. Read, and G. Williams, *Anelastic and Dielectric Effects in Polymeric Solids*, Wiley, New York, 1969.
- [135] W. Brostow, R. Chiu, I. M. Kalogeras, and A. Vassilikou-Dova, *Materials Letters*, 2008, **62**, 3152–3155.

- [136] A. Bos, I. G. M. Pünt, M. Wessling, and H. Strathmann, *Journal of Membrane Science*, 1999, **155**, 67–78.
- [137] A. Bos, I. G. M. Pünt, M. Wessling, and H. Strathmann, *Journal of Polymer Science Part B-Polymer Physics*, 1998, **36**, 1547–1556.
- [138] M. W. Hellums, W. J. Koros, G. R. Husk, and D. R. Paul, *Journal of Applied Polymer Science*, 1991, **43**, 1977–1986.
- [139] V. S. Khotimskii, V. G. Filippova, I. S. Bryantseva, V. I. Bondar, V. P. Shantarovich, and Y. P. Yampolskii, *Journal of Applied Polymer Science*, 2000, **78**, 1612–1620.
- [140] Y. Nagasaki, Y. Hashimoto, M. Kato, and T. Kimijima, *Journal of Membrane Science*, 1996, **110**, 91–97.
- [141] H. Rios-Dominguez, F. A. Ruiz-Trevino, R. Contreras-Reyes, and A. Gonzalez-Montiel, *Journal of Membrane Science*, 2006, **271**, 94–100.
- [142] P. M. Budd, N. B. McKeown, B. S. Ghanem, K. J. Msayib, D. Fritsch, L. Staranikova, N. Belov, O. Sanfirova, Y. Yampolskii, and V. Shantarovich, *Journal of Membrane Science*, 2008, **325**, 851–860.
- [143] S. Thomas, I. Pinnau, N. Y. Du, and M. D. Guiver, *Journal of Membrane Science*, 2009, **333**, 125–131.
- [144] M. Heuchel, D. Fritsch, P. M. Budd, N. B. McKeown, and D. Hofmann, *Journal of Membrane Science*, 2008, **318**, 84–99.
- [145] O. Hölck, M. Böhning, M. Heuchel, M. R. Siegert, and D. Hofmann, *Journal of Membrane Science*, 2013, **428**, 523–532.
- [146] A. G. McDermott, G. S. Larsen, P. M. Budd, C. M. Colina, and J. Runt, *Macromolecules*, 2011, **44**, 14–16.
- [147] A. G. McDermott, P. M. Budd, N. B. McKeown, C. M. Colina, and J. Runt, *Journal of Materials Chemistry A*, 2014, **2**, 11742–11752.
- [148] B. K. Gupta, G. Kedawat, P. Kumar, M. A. Rafiee, P. Tyagi, R. Srivastava, and P. M. Ajayan, *Journal of Materials Chemistry C*, 2015, **3**, 2568–2574.

- [149] L. L. Zhang, W. J. Fang, and J. W. Jiang, *Journal of Physical Chemistry C*, 2011, **115**, 11233–11239.
- [150] A. Schönhals and F. Kremer in *Broadband Dielectric Spectroscopy*, ed. F. Kremer and A. Schönhals; Springer, Berlin, Germany, 2003; p. 59.
- [151] R. Swaidan, B. Ghanem, E. Litwiller, and I. Pinnau, *Macromolecules*, 2015, **48**, 6553–6561.
- [152] N. Konnertz, Y. Ding, W. J. Harrison, P. M. Budd, A. Schönhals, and M. Böhning, *ACS Macro Letters*, 2016, **5**, 528–532.
- [153] P. Li, T. S. Chung, and D. R. Paul, *Journal of Membrane Science*, 2013, **432**, 50–57.
- [154] P. Iyer, G. Iyer, and M. Coleman, *Journal of Membrane Science*, 2010, **358**, 26–32.
- [155] J. Ahn, W. J. Chung, I. Pinnau, J. S. Song, N. Y. Du, G. P. Robertson, and M. D. Guiver, *Journal of Membrane Science*, 2010, **346**, 280–287.